A thesis presented for the degree of
Doctor of Philosophy

Interactions and cold collisions involving AlF molecules

Sangami Ganesan-Santhi

Supervisor:
Prof. Dr. hab. Michał Tomza
Co-supervisor:
Dr. Marcin Gronowski

Abstract

Aluminium monoflouride is a great candidate for ultracold studies owing to its diagonal Frank-Condon factors and its stability. Our study involves theoretical calculations that pertains to the cooling processes involving AlF. As molecules are more complex than atoms, new methods of cooling mechanisms need to be devised for cooling molecules. This research aims to provide the theoretical background for buffer gas cooling, evaporative cooling and sympathetic cooling methods. We have employed Coupled Cluster (CC) and Multi Reference Configuration Interaction (MRCI) *ab initio* quantum chemistry methods to calculate the interaction potentials to a high accuracy. The interaction of AlF molecules with each other (tetra atomic system), helium atom (triatomic system) and with Rubidium atoms (triatomic system) have been calculated for ground and excited states of the AlF molecule. High quality potential energy surfaces are reported for all these interactions and the basis set convergence of ab initio methods and effect of relativistic effects were also studied for each of the system. The accuracy and the limitations of *ab initio* quantum chemistry methodology is also demonstrated. Scattering calculations for the AlF-He collisions were made and provide insight into the experimental prospects of buffer gas cooling of AlF. Data for future scattering calculations are also made available for the AlF-AlF and AlF-Rb interactions which would provide an theoretical basis for the corresponding experiments. One other main result of this study is the full four dimensional interaction potential for AlF-AlF interaction is calculated with significant accuracy.

Acknowledgement

I am grateful for my supervisor Dr. hab. Michal Tomza for giving this great opportunity. I feel really fortunate to have been guided by such a great scientist and a really cool person, someone who stands with us not just through our scientific endeavours but also through the hellhole of Polish bureaucracy, especially for international students. I will always be indebted to my assistant supervisor Dr. Marcin Gronowski who is a fantastic teacher and a scientist and has truly guided me through my research. Our weekly scientific discussions were integral to my growth as a scientist and a person. I am also insanely grateful to PLgrid infrastructure which made all of my research possible. I want to thank Dr. Piotr Gniewek who guided me through my initial PhD days, a sincere teacher. I am grateful to Dr. Matthew Frye for being supportive in my research and for teaching me to do scattering calculations. I am really grateful for Dr. hab. Krzysztof Jachymski for being the cool, supportive and inclusive person that he is. I have felt I am a part of his research group even more than I did in mine.

I am really grateful for my parents Santhi S. P. and Ganesan M. P. and my brother Nigaran G. S. for supporting me through my journey and being great companions in life. I am grateful and lucky for the relationship I have with you all.

I spent 4.5 years in Warsaw, I have lived in five different apartments out of which I spent two apartments in covid pandemic. I thought I would have a long list of people who accompanied me through my PhD journey but I don't, it really has been a pretty lonely path. But I am truly grateful for all my friends who made this journey worthwhile. Sakthikumaran, my closest friend with whom I shared three homes in Warsaw. I am grateful for all the million times you have made biriyani, for all the warmth and kindess that shine out of you, I love you so much. Karthiga, who just took me in as her own from the very first day and has been a great friend and a care taker since. I am grateful for her friendship and love. How glad I am to have met my dearest friend Sharat, one of the kindest most considerate person I have met, someone who made everything better by just his presence. I met Elavenil the same day as Sharat in Karthiga's home. It has been four years and he has remained a close confidante ever since. If dynamite were a person, it would be Monica. She is such a strong supporter and a great friend and I really believe she is an agent of chaos and truly one of a kind. I am really grateful for my friend Debjitha who is such a warm supportive friend and a great companion. One of the loveliest things that happened to me in Warsaw is my friendship with Joao and Lucielly, our friendship is a melting pot of two cultures, I am grateful for their love and kindness. Lucielly is just a sister from another mother, I love her so much. Piotr, my only close Polish friend but a great one, I am grateful for all the weird wonderful times we had together and for his sweetheart of a dog Pela whom I think is the greatest dog ever. Hela, my only friend from work, I am really grateful for her strong support through my work and for simply being a wonderful person. We all shared our food, culture and love when we were all feeling alien in Poland. Warsaw became special, Warsaw became a home for me because of every single one of them.

I will always be indebted to the love and friendship I share with Ganeshwar, Ruthu, Kaladhar and Anjali which has kept me going through shitty times, including covid. The chosen family I will cherish for life.

A special shoutout to my dearest cousin and friend, Raajadharshini, who is the perfect companion and support anyone could ever ask for and an insanely talented artist, I am just so grateful to her for simply persisting through life with me, I love you so much.

Contents

1 Introduction **9**
- 1.1 Quantum behavior in ultracold regime . . . 9
- 1.2 Ultracold molecules and their production . . . 10
  - 1.2.1 Direct cooling methods . . . 10
  - 1.2.2 Indirect cooling methods . . . 14
- 1.3 Application of ultra cold molecules . . . 15
  - 1.3.1 Controlled chemistry . . . 15
  - 1.3.2 Precision measurements . . . 16
  - 1.3.3 Quantum many-body physics . . . 16
- 1.4 Importance of electronic structure theory . . . 16

2 Aim of this research **19**

3 Methods **23**
- 3.1 *Ab initio* electronic structure theory . . . 23
  - 3.1.1 Born-Oppenheimer approximation . . . 23
  - 3.1.2 Electronic wavefunctions . . . 24
  - 3.1.3 Hartree-Fock method . . . 25
  - 3.1.4 Basis sets and the CBS limit . . . 28
  - 3.1.5 Basis set superposition error (BSSE) . . . 30
  - 3.1.6 Electron correlation . . . 30
  - 3.1.7 Long range interaction . . . 38
- 3.2 Scattering theory . . . 42
  - 3.2.1 Coupled channel scattering theory . . . 44

4 AlF **47**
- 4.1 Methods . . . 47
  - 4.1.1 *Ab initio* methods . . . 47
  - 4.1.2 Dipole moment and polarizability . . . 48
- 4.2 Results . . . 49
  - 4.2.1 Potential energy curves . . . 49
- 4.3 Excited state . . . 53
  - 4.3.1 Dipole moment and polarizability . . . 54
  - 4.3.2 Conclusion . . . 56

5 AlF-He **57**
- 5.1 Methods . . . 57
  - 5.1.1 Ab initio electronic structure theory . . . 57

5.1.2 Collision theory 60
5.2 Results 61
5.2.1 Potential energy surfaces 61
5.2.1 Collision dynamics 70
5.2.2 Conclusion 74

6 AlF-AlF **75**
6.1 Methods 76
6.2 Results 78
6.2.1 Ground state X^1A' 78
6.2.2 Optimization 84
6.2.3 Potential energy curves for excited states 84
6.3 Conclusion 90

7 AlF-Rb **91**
7.0.1 Methods 91
7.0.2 Results 92
7.0.3 Conclusion 96

8 Summary and Outlook **97**

List of Figures

1 Introduction

1.1 Quantum behavior in ultracold regime

The temperatures we are familiar with in our lives on earth are between -100° to $50^\circ\mathrm{C}$, but how does matter exist outside this range? At room temperature, the air molecules whizzing by at the speed of sound at around $400\ \mathrm{m/s}$, their de Broglie wavelength is so small that their wave character becomes inconspicuous. To study them, it would be much more convenient if the effects of thermal motion were reduced, that is, if the atoms were colder. As we approach the ultracold regime, quantum behavior takes over and it becomes easier for us to observe, control and manipulate quantum systems. The collisions between atoms at low energies exhibit special behavior due to long collision time and distance [1]. The scattering is dominated by few partial waves and the cross sections can be decomposed into partial wave components from incoming partial waves with different angular momentum. The threshold behavior of elastic and inelastic collision cross section is limited by the Wigner threshold laws [2]. It predicts that the elastic cross section becomes constant as the temperatures approaches zero and the inelastic cross section increases as $1/\sqrt{T}$ where T is the temperature of the gas. We also begin to observe scattering resonances which are usually averaged out at room temperature.

At low temperatures, the de Broglie wavelength, $\lambda_{db} = h/mv$, of matter increases with decreasing velocity v that when the temperature is low enough, the de Broglie wavelength becomes comparable to the distance between atoms. Also, for heavier atoms the de Broglie wavelength is smaller than for lighter atoms. At this point, almost all bosonic atoms occupy a single quantum state. This was predicted by Satyendra Nath Bose and Albert Einstein in 1924 [3, 4, 5] and the first Bose-Einstein condensate was produced in 1995 in a vapor of rubidium-87 atoms [6, 7] at 170 nanokelvin. Another interesting quantum behavior in the cold regime is the quantization of kinetic energy of electrons which allows the formation of Cooper pairs or bosonic pairs (from electron-phonon interaction) which gives rise to superconductivity discovered by Heike Kamerlingh Onnes in 1911 [8].

The nature of cold and ultracold collisions bears critically on light-guided manipulation of reactive and inelastic processes [9, 10, 11], fundamental concepts of quantum chemistry [12, 13, 14], precision measurement [15, 16] and loss channels in formation pathways [17, 18]. More than the fundamental physics aspect of ultracold studies, the very production of ultracold systems and their exciting applications in quantum simulations and the rise of quantum technologies [19] also occupy a central part of ultracold research. The advent of laser spectroscopy and non-linear optics in the 1970s reached its height in 1981 with a Nobel prize awarded to A. L. Schawlow and N. Bloembergen "for their contribution to the development of laser spectroscopy" [20, 21] while in 1989 a Nobel prize was awarded "for the development of ion-trap technique" to H. G. Dehmelt and W. Paul. Cooling and trapping techniques for atoms have been available since 1980s [22, 23]. This led to an unprecedented growth in production, control and manip-

ulation of ultracold atoms or ions from trapping atoms using electromagnetic fields [24, 25] to quantum simulation using ultracold atoms [26]. The advancement of ultracold atom research paved way for the much more complex field of ultracold molecules. We will dive into a general introduction to production and application of ultracold molecules.

1.2 Ultracold molecules and their production

Molecules are more complex than atoms owing to their rotational and vibrational degrees of freedom. Laser cooling, in general, requires a simple electronic structure such that a transition cycle can be established without off-resonant flourescence. But as the vibrational transitions are governed by Franck-Condon factors (overlap of vibrational wavefunctions), consequently, after spontaneous emission molecules tend to disperse across a vast range of vibrational states. Heteronuclear molecules also have permanent dipole moment. The smaller energy scales of rotation and vibration makes them much more responsive to electric and magnetic fields than atoms. These properties makes molecules more interesting but also more difficult to cool. There are two ways to produce cold molecules, direct and indirect methods. The first method involves the direct cooling of molecules themselves. The later method involves photo- or magnetoassociation [27, 28] of pre-cooled atoms at ultralow temperatures.

1.2.1 Direct cooling methods

Ultracold molecules can be directly formed in a few ways such as collisional cooling (like buffer gas cooling), phase-space conserving deceleration of molecular beams using external electric or magnetic fields, laser cooling, sisyphus cooling and evaporative cooling.

One of the main challenges faced during direct cooling of molecules is the introduction of the species of interest into the cooling apparatus. Most common methods of species introduction are laser ablation, beam injection and capillary filling. The first technique involves laser ablation of a suitable solid precursor [29, 30]. Beam injection is when high intensity beam sources are coupled to the buffer cell [31]. In capillary filling a gas from high temperature is guided into the buffer call using a capillary [32].

Collisional cooling

Buffer gas cooling Buffer gas cooling Buffer gas cooling is a direct cooling method in which the translational and internal energies are dissipated through collisions with cold, inert gas atoms, usually helium. Typically serving as one of the initial cooling steps, buffer gas cooling aids in preparing a sample for ultracold temperatures and is generally effective at temperatures above a few hundred millikelvin [33]. It is important to understand the process that occurs inside a buffer gas cell as all experiments begin from this point. In principle, buffer-cell cooling allows for the thermalization of both translational and internal degrees of freedom; however, the balance between them is determined by the ratio of elastic to inelastic collisions. One of the main advantages of buffer gas cooling is that it is very versatile, it can be used to cool almost any atom or molecule. Helium is one of the most commonly used buffer gases because it has an appreciable vapor pressure even at few hundred millikelvin.

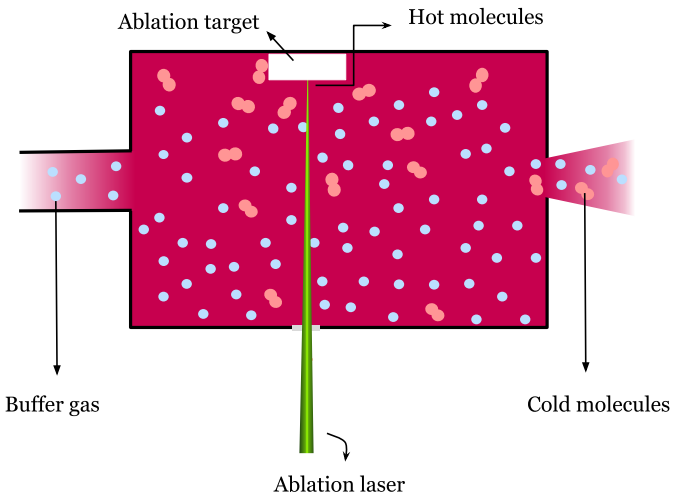

Figure 1.1: Buffer gas cooling scheme.

The Buffer gas cooling efficiency depends on the cell parameters and on the density and temperature of the buffer gas. If the density of the buffer gas is too low, the molecules may not thermalize and if the density is too high, molecules will thermalize near the cell entrance and scatter away, reducing the extraction efficiency. This puts a limit on the density and hence a limit on the temperature of the buffer gas. For ^{3}He, the temperature can be as low as 180mK and for ^{4}He, it can be 500 mK for a cell of order 1 cm in diameter [34]. One of the first buffer gas cooling and subsequent trapping of a molecule (CaH) was demonstrated by J. Doyle's group [30].

Sympathetic cooling The physics of sympathetic cooling is the same as buffer gas cooling but the difference is that the collision partners here are ultracold atoms. This method is usually used on trapped cold molecules to bring them into the ultracold regime. The efficiency of the cooling depends on the ratio of elastic to inelastic collisions. There has been recent demonstrations of sympathetic cooling of molecules to micro- and nano kelvin temperatures [35, 36]. In 2020, cooling of NaLi molecule to 220 nanokelvin was demonstrated using sympathetic cooling with ultracold Na atoms and by employing two stages of evaporation [35].

Evaporative cooling Evaporative cooling, like other collisional methods, is based on elastic collisions leading to energy exchange and re-equilibriation of the translational temperature of the molecule and on selective removal of the most energetic molecules. Similar to sympathetic cooling, evaporative cooling is used to bring cold molecules into the ultracold regime after trapping them in a magnetic or optical trap. For a trap with finite depth, the molecules with highest energy reaches the top and escapes, resulting in a lower average temperature. As the trap depth is continuously lowered allowing the new high energy molecules to escape, leading to colder and denser samples, eventually reaching the quantum-degenerate regime.

Inelastic collisions generate heat and lead to trap loss. An efficient evaporative cooling requires a high ratio of elastic to inelastic collisions. One other requirement is shorter thermalization time than the lifetime of the sample. In 1986, Hess proposes and discusses the evaporative cooling process [37] which was also used experimentally to create the first Bose-Einstein condensation [6, 7]. The first evaporative cooling of ultracold molecule was obtained in 2012, in experiment, where a hydroxy radical [38] from a Stark decelerated beam was trapped in a high-gradient magnetic quadrupole trap.

Deceleration of molecular beams

The motion of neutral (polar) molecules can be decelerated using electric or magnetic fields. In both Stark and Zeeman field decelerators, pulsed inhomogenous electric or magnetic field is used to slow down molecules with electric or magnetic dipole moments. The method uses the state specific force that a molecule (with electric or magnetic moment) experiences in an electric or a magnetic field. A similar method called optical deceleration is when lasers are used to form optical potentials which pulse. High phase space density molecule source is one of the important conditions for successful deceleration.

Electromagnetic fields have been used in accelerator physics for many years and Zeeman decelerators have been used to slow atoms [39]. The first Stark deceleration of neutral polar molecules was implemented by Meijer et al. where they have experimentally demonstrated efficient deceleration of neutral CO molecules to about 15 K [40, 41]. A number of polar molecules, like ND_3 [41], OH [42], YbF [43], NH [44], H_2CO [45], SO_2 [46], have been decelerated since and have been further used for experiments. Few of the recent contributions includes a proposal for ring-shaped Zeeman decelerator for heavy molecules that might overcome the limitations of traditional Zeeman decelerators [47] and capture of SrF at $20\mathrm{mK}$ in moving trap Stark decelerator [48].

Laser (Doppler) cooling

Doppler laser cooling is based on the scattering force produced by a photon resonant with an atomic transition. An atom illuminated with a laser which is slightly detuned below the atomic transition frequency (red detuned) gets cooled by continuous cycles of absorption and stimulated emission. Atoms moving towards the laser may absorb a counter-propagating photon which Doppler shifts closer to the atomic resonance and the momentum of the absorbed photon reduces the velocity of the atom by $\hbar k/m$ (where k is the wave vector of the laser beam, m is the atomic mass). Laser cooling gained traction about 40 years ago, mostly motivated to improve atomic clocks and atomic spectroscopy. Since then, there has been remarkable advancement in the field of atomic laser cooling with a Nobel prize awarded in 1997 for Doppler laser cooling [49, 50, 51, 52].

Because of their less complex energy structure than molecules and sharp atomic resonances, it is easy to assume a strictly two-level electronic structure for atoms but it is not the case for molecules. We cannot directly apply the atomic translational cooling methodology on molecules as they have many non-resonant rovibrational ground states and one would need multiple repumping lasers. Many schemes have been suggested to overcome this problem like using mul-

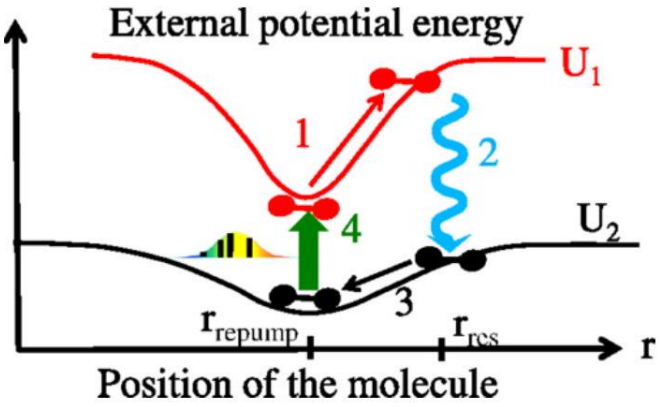

Figure 1.2: The working principle of sisyphus cooling is demonstrated in four steps. (1) The kinetic energy of the molecule is removed through motion in an external potential; (2) the "sisyphus transfer step" where a dissipative process prevents the reverse motion; (3) bringing the molecule back in position using the trapping potential; (4) absorbing repumping laser to bring the molecule to its original state. The above image was taken from [62].

tiple lasers, closed optical cycling schemes (SrF, the first molecule to be laser cooled), local optimization of the laser pulse shape in the excitation step, choosing molecules with a highly diagonal Franck-Condon matrix [53, 54, 55, 56]. Later, transverse laser cooling of a beam of polar yttrium oxide (YO) molecules was demonstrated, reaching about $15\mathrm{mK}$ [57]. Laser cooling of YbF molecules to temperatures below $100\mu K$ was also demonstrated in 2018 in an experiment designed to measure the electron's electric dipole moment [58].

Di Rosa was the first to notice the existence of molecules with almost diagonal (quasi diagonal) Franck-Condon matrix [59]. She proposed a class of molecules suitable for laser cooling with Franck-Condon factors for $0' - 0, 0' - 1, 0' - 2$ vibronic transitions close to the ratio 0.99:0.009:0.0009. The probability of population of the first three vibrational levels of the ground electronic state after spontaneous emission from the zero vibrational level of an excited electronic state is near 0.9999 [60]. She reported that the inclusion of two more vibrational levels of ground electronic state into the cooling cycle might make laser cooling much more efficient. This would require one to use lasers at the $1 - 0'$ and $2 - 0'$ transitions to pump the population back to the $0 - 0'$ transition. $\mathrm{AlF}, \mathrm{CaH}, \mathrm{MgH}, \mathrm{SrH}$ are among the molecules that she proposed. Many of these molecules have been laser cooled [53, 61].

Sisyphus cooling

First proposed in 1989 [63], sisyphus cooling (also called as polarization gradient cooling) is a type of laser cooling which combines a dissipative process and an absorption-spontaneous emission process to cool. Such a non-reversible process is repeated by optical pumping the molecule back to its original state (hence the usage of the term sisyphus). In atoms, the energy transfer is provided by counter propagating laser beams with orthogonal polarization. The molecules lose

their kinetic energy as they move up a potential at which point optical pumping is used to bring them back to a lower energy state. In the first demonstration of the sisyphus cooling of (polyatomic) molecules in 2012 [64, 62], microwave transitions between vibrational states provide the energy transfer. Zeeman-Sisyphus deceleration of a beam of ytterbium monohydroxide was reported recently which seems exciting [65].

1.2.2 Indirect cooling methods

Indirect cooling methods are based on associating atoms. The basic requirement for indirect ultracold molecule production is ultracold atoms. The foundation for these methods are laid by laser cooling and evaporative cooling of atoms. Indirect cooling methods have been one of the most successful methods in creating ultracold molecules. The limitation of indirect cooling is that only atoms which can be laser cooled and trapped can be used to create ultracold molecules. So, most indirect cooling experiments involve bialkali molecules. Key laser cooling techniques have been developed in the early 1980s [66, 67].

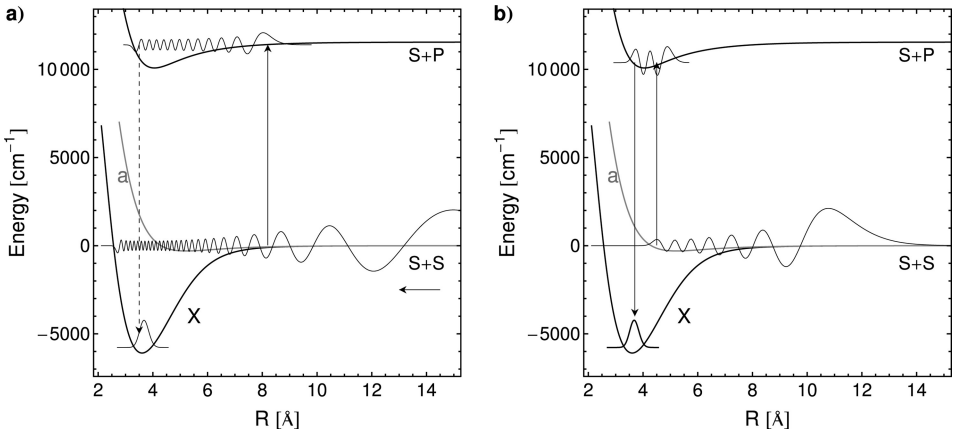

Figure 1.3: A scheme of a) photoassociation followed by spontaneous emission and b) magnetoassociation followed by Stimulated Raman Adiabativ Passage (STIRAP) is presented. The image is taken from Ref.[27]

Photoassociation

Photo-association is the process where colliding atoms absorb light and form a bound excited state. Laser-induced or spontaneous transitions are then used to bring the dimer to the electronic ground state. The photoassociation process usually starts at a hot atom source which needs to be cooled. One of the many methods such as Zeeman cooling or magneto-optical trap is used for this step. The first ultracold gas of molecules was created using photoassociation. Translationally cold Cs_2 ground-state molecules in the micro-Kelvin range were obtained through photoassociation of laser-cooled cesium atoms in a magneto-optical trap [68]. There is massive research and literature on photoassociation of homo-nuclear diatomic ultracold molecules including Na_2, Rb_2, Cs_2 and K_2 [69, 70, 71, 72, 73].

Despite the studies on photoassociation of unlike pair of atoms [74], the first ultracold polar molecule was formed using photoassociation only in 2004. Laser cooled mixture of Rb and Cs atoms were photo-associated to form ground state RbCs molecule [75, 76]. Other polar molecules such as KRb [77, 78], NaCs [79], LiCs [80] have since been produced using photoassociation.

magnetoassociation using Feshbach resonances

A Feshbach resonance occurs when the collision energy of two colliding atoms become degenerate with a bound excited state of the diatomic molecule. The energy difference between the scattering state and the bound state can be controlled through magnetic field. This is termed as *magnetically tunable Feshbach resonance* [81, 28]. While investigations of Feshbach resonances (coupling of bound state to the continuum) go back to 1930s, Herman Feshbach and Ugo Fano developed their work independently [82, 83, 84]. Feshbach resonances as useful tools to control interactions between ultracold atoms was first proposed in 1993 [85]. The interaction tuning using Feshbach resonances were first demonstrated in 1998 [86, 87] which became a fully established tool in few years and opened up many new applications [88, 89, 90].

The idea of magnetoassociation is to transfer the atoms from the scattering state to the bound state to form molecules. The molecules formed through magnetoassociation are also referred to as Feshbach molecules. Feshbach molecules are highly excited molecules with small binding energy compared to the vibrational ground state. As in photoassociation, the highly excited molecules are then transferred to deeply bound states through stimulated emission and STIRAP processes. Magneto-association of homo- and hetero-nuclear systems have been demonstrated [91, 92, 93, 94, 95].

1.3 Application of ultra cold molecules

1.3.1 Controlled chemistry

At ultracold temperature the collision energies of atoms and molecules are much smaller than the intermolecular forces and the chemical reactions and collision dynamics can be controlled by influencing the long range forces [96, 97]. One more advantage is the preparation of molecules in specific spin and hyper-fine levels which becomes impossible at ordinary temperatures with high thermal energy collisions. In an experiment conducted at JILA, optically trapped ultracold ^{40}K^{87}Rb molecules were prepared in different hyper-fine levels to study quantum state controlled chemical reactions. At few hundred nano kelvin temperature, when the molecules are in the same quantum state , p-wave collisions dominated and the reaction KRb + KRb $\rightarrow$ K_2 + Rb_2 required tunneling through the p-wave centrifugal barrier. But when the molecules are in two different internal states, the reaction rates are increased due to s-wave scattering [9]. The dipole-dipole interaction of OH molecules is shown to be influenced by electric and magnetic fields [98]. Stark decelerated OH radicals were scattered with hexapole-focused NO radicals to study the quantum-state resolved bimolecular collisions [99].

1.3.2 Precision measurements

The rich energy structure of molecular systems provide a set of precise frequency benchmarks in microwave, infrared and visible spectrum. Narrow transitions in molecules and low collisional broadening at low temperatures allows for a high spectral resolution which makes ultracold molecules great for precision measurements. The time variation of proton-electron mass ratio $\Delta\mu/\mu$ ($\mu = m_{proton}/m_{electron}$) is tested using Sr_2 dimers in a zero-differential-Stark-shift optical lattice [100]. Highly accurate vibrational spectroscopy of sympathetically cooled HD^+ ion which could also lead to an improved determination of electron-proton mass ratio [101]. The electric dipole moment has been measured using cold YbF molecules [102]. This molecular measurement of the electron EDM has exceeded that of the best atomic measurement. The metastable state $a(1)[^3\Sigma^+]$ of PbO molecule has also been proposed to search for electron EDM [103].Precise measurement of microwave transitions in cold hydroxy radical molecule has been reported in [45]. Diatomic molecules have been proposed for parity violation studies owing to the sensitivity of their rovibrational spectra to nuclear effects [104, 105].

1.3.3 Quantum many-body physics

An important application of ultracold molecules is quantum simulation where ultracold molecules are used to form a model of an unsolvable many-body Hamiltonian [106]. Hetero-nuclear diatomic molecules in optical lattices have been studied and a molecular Hubbard Hamiltonian for this system is presented [107]. The large electric dipole moment of the polar molecules allows for long-range dipole-dipole forces in DC electric field and transitions between rotational states in an AC microwave field [108]. Spin exchange interactions have been observed in lattice confined dipolar molecules [109]. Ultra cold molecules in lattices offer oppurtunities to study many-body phenomenon such as superfluidity, quantum magnetism [110, 111], etc. The emergence of a topological super fluid of identical microwave-dressed fermionic polar molecules in a 2D lattice has been demonstrated [112]. The many-body physics of molecular Bose-Einstein condensates was studied [113] and formation of self-bound droplets were observed [114, 115].

1.4 Importance of electronic structure theory

The aim of electronic structure theory is to develop methods that can be applicable to a wide range of chemical problems. Ab initio quantum chemistry has become an important tool to study atoms and molecules and to model complex systems. A theoretical framework is essential to understand the fundamental physics and also to construct efficient methods with predictive power. The development of efficient computers and development of the electronic structure methods have made them a significant part of the modern research. Paper [116] collects the historical development in ab initio electronic structure theory.

The central problem in *ab initio* electronic structure theory is to solve the electronic Hamiltonian for a many body wavefunction. The electronic structure provides information on molecular properties such as dipole moments, polarizabilities, transition moments, long range coefficients and equilibrium geometries. For larger, more difficult molecules, electronic structure calculations become an important starting point for experiments. Ab initio molecular orbital methods

are based only on the laws of quantum mechanics and on fundamental constants. Hence the term ab initio, meaning "from first principles". Ab initio calculations do not depend on any experimental data.

Experimental and theoretical studies complement and benchmark each other. One such classic case of theory vs experiment is the vibrational spectrum of the hydrogen bond. Hydrogen bond is an interaction that influences the properties of many chemicals and biochemical systems.

An important property associated with the presence of hydrogen bond is a shift in the infrared (IR) spectrum of the A-H stretching band after formation of the A-H ... B hydrogen bond. The A-H covalent bond can remain intact or a proton transfer can occur resulting in $\mathrm{A}^{-} \ldots {}^{+}\mathrm{H} - \mathrm{B}$ ion pair. The global minimum of a hydrogen-bonded complex is probed through IR spectroscopy and theoretically using ab initio calculations. The equilibrium structure of a hydrogen bonded complex also depends on the level of theory used to describe it [117]. So, there is a question of what level of theory is required to give reliable predictions [118]. If the hydrogen bond resides in a broad and a relatively flat potential well, a harmonic treatment of the proton stretching vibration cannot describe the anharmonicity of the potential energy surface which created discrepancy with the experimental results. The case was resolved by estimating the anharmonicity of the proton stretching motion and when the IR spectrum was recomputed using the anharmonic stretching force constant, a great agreement between theory and experiment was found [119, 120]. Another similar case is of CH ... O hydrogen bonds. The red and blue shift in the IR spectra due to the presence of this bond is investigated [121]. To give an idea of the applications of ab initio electronic structure methods, theoretical calculations have been used along side experiments to predict the geometric structure and other properties of many molecules including benzene, naphthalene, CO_2 [122, 123, 124], used to model photo-chemical applications [125], a comprehensive understanding of functioning of enzymes has been obtained by theory and experiment together [126, 127, 128]. Accurate ab initio calculations have been used to match high energy rovibrational levels of water molecule to prove its presence in the Sun and to study the green house effect in Earth [129, 130].

Ab initio electronic structure methods offer highly accurate calculation of ground state potential energy surfaces and molecular properties, especially for smaller systems. The peculiarity of ultracold regime is that the quantum behaviour atomic and molecular interactions are magnified. The electronic structure results have direct relevance to the interactions in this regime. Even weak van der Waal type interactions can be probed and controlled [131, 132, 133].

In the context of ultracold studies, ab initio quantum chemistry methods are an important tool. Theoretical predictions obtained from ab initio calculations can guide experimentalists in designing ultracold experiments which are challenging and resource-intensive. Let us go through a few examples that illustrate the importance of ab initio quantum chemistry for ultracold studies. The spectroscopic properties of Rb_2 molecule in the presence of a non-resonant laser field is studied using the double electron attachment intermediate Hamiltonian Fock space coupled cluster method. It is seen that the spectrum is significantly altered by the non-resonant field and this can be a new method to control photoassociation rates [134]. The internally contracted multiconfiguration reference configuration interaction method is used to identify new tetratomic molecules, CaCCH and SrCCH molecules, and demonstrate the feasibility of laser cooling schemes [135]. An ab initio polyatomic complex potential energy surface was used to interpret the auto-ionization process observed in the $\mathrm{He}\left(2^3\,\mathrm{S}\right)+\mathrm{H}_2$ collision [136]. For the same $\mathrm{He}+\mathrm{H}_2$

system, the effect of the anisotropy of the interaction potential on the quantum resonances is measured. Ab initio theory is used to show that switching between rotational states of the system also switches on or off the anisotropy of the interaction [137]. High level electronic structure calculations have been used to investigate reactions involving pairs of alkali-metal dimers. They show that trimer formation reactions are energetically forbidden for low-lying singlet states of the dimers [138]. An MP2 electronic structure calculations was performed to obtain the potential energy surface for the reaction $\mathrm{Li}^+ + n - \mathrm{C_3H_7Cl}$ which reflects the complex reaction pathway followed by the reaction from reactants to products [139]. The electronic structure of RbBa molecule is extensively investigated at the MRCI+Q level. From the calculated Franck-Condon factors and transition properties, direct laser cooling of RbBa is infeasible [140]. An *ab* initio investigation of Li-alkaline-earth dimers was performed to arrive at a comprehensive analysis of their interactions in an optical trap [141]. An ab initio complete active space self consistent field (CASSCF)/(MRCI+ Q) calculations were used to study the electronic structure of CaK molecules and a laser cooling scheme for CaK is proposed from these results [142]. Multilayer Multiconfiguration Time-Dependent Hartree Method for Bosons and Fermions (MLMCTDHB) method, an ab initio method used to study ultracold quantum gases, is employed to study the ultracold chemistry of bosonic and fermionic mixtures [143]. They also discuss the role of correlation in transmission and reflection properties of collisions.

2 Aim of this research

The aim of this research is to theoretically investigate the feasibility of cooling of aluminium monofluoride molecule. AlF is a great candidate to study ultracold phenomenon. In comparison to alkali and alkaline earth metal fluorides, AlF is much more stable as seen in the Tab.2.1.

The aluminium fluoride molecule is an ideal candidate to cool down [27, 144, 145]. This is primarily due to its highly diagonal Frank-Condon factors which is perfect for laser cooling [146, 147]. However, another advantage of AlF is its chemical stability due to relatively high binding energy (about 7 eV). As binding energy of simple monofluorides grows, the efficiency of the reaction of the fluorinating reagent with hot ablated metal also increases, as was demonstrated by theoretical computations for AlF and CaF [148]. A comparison of buffer gas-cooled beams of four monofluorides shows that the one containing AlF is an order of magnitude brighter than others, probably due to the low efficiency of the formation of MgF, CaF, and YbF [149]. Once cooled, its relatively large dipole moment of 1.5 D makes it a promising candidate for studying numerous types of dipolar physics.

Before AlF became the object of research in ultracold temperatures, the discovery of AlF in a protoplanetary circumstellar envelope sparked astronomers' interest in this molecule [150]. For this reason, Gotoum *et al.* reported the first potential energy surface of the AlF+He complex [151]. This potential exhibits only one minimum and depth about 24 cm^{-1}. Newer studies [145] suggest that the potential is shallower by about 2 cm^{-1}.

Let's go through the history of research on AlF relevant for this study. The research on AlF in early 1900s involved production of AlF and study of the thermodynamic and spectroscopic properties [152, 153, 154]. A boom in both theoretical and experimental study of the spectrum and electronic structure of AlF can be seen since the 1970s [155, 156, 157, 158, 159, 160]. In 2004, M. D. Di Rosa proposed a class of diatomic molecules optimal for laser cooling in which AlF was a prominent candidate. These molecules possess highly diagonal band system that allows for a closed cooling cycle [55]. The study, production and spectroscopic characterisation of ultracold aluminium monoflouride molecule has emerged in the past two decades and the experimental research on AlF is led by Dr. Stefan Truppe et. al. The production of AlF buffer gas beam at cryogenic temperatures and an exploration of optical cycling schemes and losses are recent progress in the field [146, 144, 145, 148, 149, 161].

My current research involves theoretical study of AlF and its interaction with He, with other AlF molecules and Rb. My aim is to gain a better understanding of the physical phenomenon behind buffer gas cooling and evaporative cooling of AlF. We also aim to report highly accurate potential energy surfaces for AlF-He, AlF-AlF and AlF-Rb interactions. The highly accurate ab initio studies reflect the anisotropic interaction landscape of these systems and can serve as a benchmark for future experimental studies. The usage of ab initio calculations also presented us an oppurtunity to study the convergence behavior and feasibility of different ab initio methods. The effect of including corrections such as relativistic corrections, usage of mid bonds,

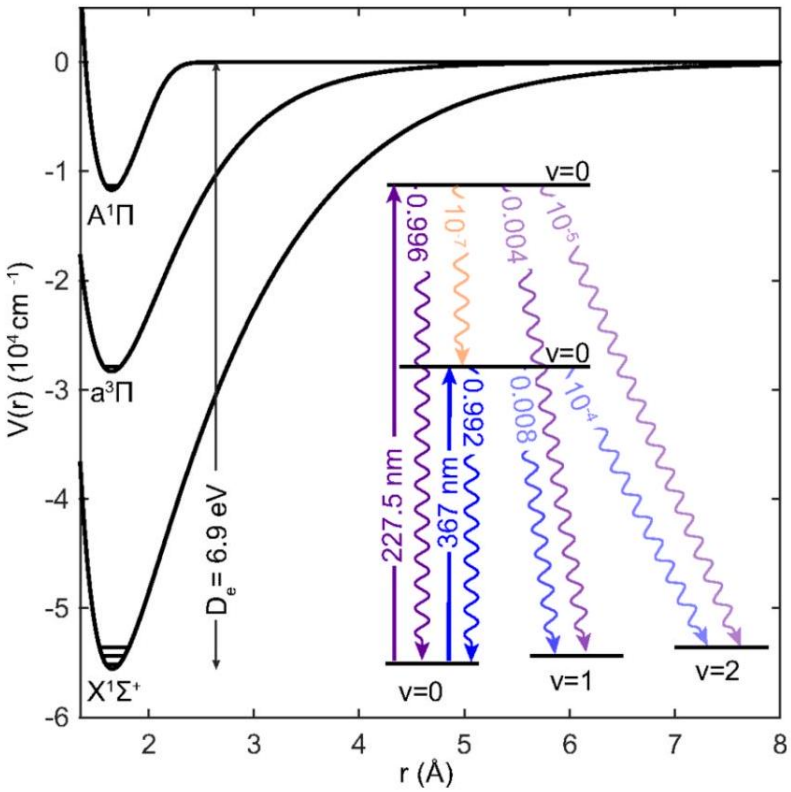

Figure 2.1: Potential energy curves of three electronic states of AlF proposed for laser cooling. The transition wavelengths and Franck-Condon factors are also presented. This image is take from this work [146].

core-valence basis sets, inclusion of higher excitations were also studies. We also report the optimized global minimum configuration of AlF-He, AlF-AlF and AlF-Rb systems. We also present accurate results on AlF-He collisions. Our collision results on AlF-He shows that buffer gas collision of AlF can be highly successful.

Table 2.1: Bond dissociation energy of XF. The energies are in cm^{-1}

AlF	57,152.2
LiF	48,233.161
NaF	40,208.233
KF	41,587.5175
RbF	41,294.942
CsF	42,966.802
BeF	48,233.161
MgF	38,619.966
CaF	44,053.511
SrF	45,307.406
BaF	40,709.791

In the third chapter, we discuss the theoretical methods used in the study. We provide the basic ideas of ab initio electronic structure calculations and scattering theory. The fourth chapter consists of our results on aluminium monofluoride and their potential energy curves. The fifth chapter encapsulates our results on AlF-He interaction to predict the buffer gas cooling prospect of AlF molecule. The sixth chapter contains results on AlF-AlF interaction which would help us theoretically predict the evaporative cooling prospect of AlF molecule. The AlF-Rb potential energy surfaces are reported in chapter seven which forms the basis for future scattering calculations. I summarise all the results in chapter eight.

3 Methods

In this chapter, we will briefly go through the introductory concepts of ab initio electronic structure theory and introduce the ab initio wave function based methods used in our calculations. A short introduction to long range forces and scattering theory is also included.

3.1 *Ab initio* electronic structure theory

The requirements for a theoretical model chemistry has been proposed by John Pople who was rewarded the Nobel prize in 1998 for developing computational methods for the theoretical study of molecules [162]. These requirements mainly constitute the following:

- Size consistency.
- Size extensivity.
- Accuracy (1 kcal/mol.)
- Agrees with experimental data.
- Should be applicable generally to any chemical species.

Size consistency is when a method gives the total energy as E_{tot} as the sum of monomer energies $E_A + E_B$ at infinite separation. Size consistency implies correct dissociation into fragments. Size extensivity is when a method scales linearly with the size of a system. All these properties are desirable in a model but until now no method has satisfied all these criteria. There is always a bargain between cost and accuracy. But availability of high performance computers has improved the accuracy tremendously [163, 164, 165, 166].

3.1.1 Born-Oppenheimer approximation

At the sub-atomic scale, the behavior of matter is governed by the Schrodinger equation. The time-independent non-relativistic Schrodinger equation is given as

$$\hat{H}\Psi = E\Psi \tag{3.1}$$

where H is the Hamiltonian of a system composed of K nuclei and N electrons, which can be written as follows,

$$\hat{H} = -\sum_{i=1}^{N} \frac{\hbar^2}{2m_e}\nabla_i^2 - \sum_{A=1}^{K} \frac{\hbar^2}{2m_A}\nabla_A^2 - \sum_{i=1}^{N}\sum_{A=1}^{K} \frac{Z_A e^2}{r_{iA}} + \sum_{i=1}^{N}\sum_{j>i}^{N} \frac{e^2}{r_{ij}} + \sum_{A=1}^{K}\sum_{B>A}^{K} \frac{Z_A Z_B}{r_{AB}}, \tag{3.2}$$

where $\vec{r}_A$ and $\vec{r}_i$ are position of nucleus A and electron i respectively and $r_{AB} = |\vec{r}_A - \vec{r}_B|$, $r_{ij} = |\vec{r}_i - \vec{r}_j|$, m_A and m_e are mass of the nucleus A and electron i respectively, ∇_i^2 and ∇_A^2 are Laplacian operators that involve differentiation with respect to the position of i th electron and Ath nucleus, Z_A is the atomic number of nucleus A. The first two terms are the kinetic energy operators for electrons and nuclei respectively, the third term describes the Coulomb attraction between electrons and nuclei, the last two terms describe the repulsion between electrons and nuclei respectively. The last three interaction terms depends only on the relative distance between the particles.

The Schrödinger equation is known to be used to obtain the analytical solution of simple systems like the hydrogen atom. The solution for many electron atoms and molecules require approximations since the wave function describing the correlated motion of $N + K$ interacting particles is difficult or impossible to solve analytically. In an attempt to simplify the problem at hand, the Born-Oppenheimer approximation is implemented. It is a type of adiabatic approximations within which the motion of nuclei and electrons can be separated. So, the approximation is that we consider the motion of electrons in the field of fixed nuclei. This is one of the adiabatic treatments of the problem. In equation 3.2, the second term describing the kinetic energy of the nuclei can be neglected and the last term describing the Coulombic repulsion between nuclei can be considered a constant. For the sake of convenience atomic unit will be used further in the text. In this convention the mass of electron, m_e and $\hbar$ are set to the value 1. The remaining terms form the electronic Hamiltonian

$$\hat{H}_{el} = -\sum_{i=1}^{N} \frac{1}{2}\nabla_i^2 - \sum_{i=1}^{N}\sum_{A=1}^{M} \frac{Z_A}{r_{iA}} + \sum_{i=1}^{N}\sum_{j>i}^{N} \frac{1}{r_{ij}}, \tag{3.3}$$

The electronic Schrodinger equation reads

$$\hat{H}_{el}\psi_{el} = E_{el}\psi_{el}, \tag{3.4}$$

where the electronic wave function, $\psi_{el}\left(\vec{r}_i; \vec{r}_A\right)$ depends explicitly on the electronic coordinates, $\vec{r}_i$ and parametrically on the nuclear coordinated, $\vec{r}_A$. This means that for different set of nuclear coordinates, there is a different electronic wavefunction. Then, the nuclear motion is directed by the electronic potential averaged over the motion of electrons. Using ab initio quantum chemistry, we attempt to solve the electronic Schrödinger equation on a grid of "clamped" nuclear positions.

3.1.2 Electronic wavefunctions

The simplest trial wave function employed in ab initio quantum chemistry is the Slater determinant. The Slater determinant is a representation of the wavefunction of a multi particle fermionic system and represents an anti-symmetric product of one electron functions (molecular orbitals). Molecular spinorbitals (one-electron functions) which are used as building blocks for the Slater determinants are functions of the coordinates of one electron only: three spatial coordinates and one spin coordinate ($\sigma = \frac{1}{2}$ or $-\frac{1}{2}$). A general normalized spin orbital looks like this,

$$\Phi_i\left(\overrightarrow{r_j}, \sigma_j\right) = \phi_{i1}\left(\overrightarrow{r_j}\right)\alpha\left(\sigma_j\right) + \phi_{i2}\left(\overrightarrow{r_j}\right)\beta\left(\sigma_j\right), \tag{3.5}$$

where ϕ_{i1}, ϕ_{i2} are the orbital components that depend on the position $\vec{r}$ of the electron j and spin functions α, β depend on the spin coordinate σ_j. The Slater determinant has this following form:

$$\Psi = \frac{1}{\sqrt{N!}} \begin{vmatrix} \Phi_1(1) & \Phi_1(2) & \cdots & \Phi_1(N) \\ \Phi_2(1) & \Phi_2(2) & \cdots & \Phi_2(N) \\ \vdots & \vdots & \ddots & \vdots \\ \Phi_N(1) & \Phi_N(2) & \cdots & \Phi_N(N) \end{vmatrix}, \tag{3.6}$$

where N electrons occupy N spinorbitals, Φ_i. The Slater determinant is a convenient starting point because of a few advantages. The anti-symmetric property of a determinant satisfies one of the postulates of the quantum mechanics by default. Interchanging the coordinates of two electrons correspond to interchanging two rows of the Slater determinant during which the determinant acquires a negative charge. One other important property of the determinantal form of the wave function is the inclusion of Fermi correlation or exchange correlation which means that the motion of two electrons with parallel spins is correlated. When two electrons occupy the same spin orbital, it means two columns of the determinant becomes equal which makes it zero, such a system becomes non-existent. A Fermi hole exists between the electrons. But we need to note that no correlation between the motion of electrons with opposite spins is included in this treatment.

3.1.3 Hartree-Fock method

In the Hartree-Fock approximation, the electronic wave function is described using a single determinant, that is, by a single configuration of spinorbitals. The Hartree-Fock method is a variational method where the single Slater determinant is used as the variational wave function. According to the variational principle, the best spinorbitals are those which minimizes the electronic energy, E_{el}. Rewriting the electronic Hamiltonian, $\hat{H}_{el}$ as follows,

$$\hat{H}_{el} = \sum_{i=1}^{N} h(i) + \sum_{i=1}^{N} \sum_{j>i}^{N} \frac{1}{r_{ij}} \tag{3.7}$$

where $h(i)$ is the one-electron Hamiltonian for the i^{th} electron is given by

$$\hat{h}(i) = -\frac{1}{2}\nabla_i^2 - \sum_{A=1}^{M} \frac{Z_A}{r_{iA}}, \tag{3.8}$$

Expanding the ψ_{el} and assuming that $\langle \psi_{el} \mid \psi_{el} \rangle = 1$, the electronic wavefunction over the spinorbitals, the expectation value of the electronic Hamiltonian is written as

$$E_{el} = \left\langle \psi_{el} \left| \hat{H}_{el} \right| \psi_{el} \right\rangle = \sum_{i=1}^{N} \left\langle \Phi_i | \hat{h} | \Phi_i \right\rangle + \frac{1}{2} \sum_{i,j=1}^{N} \left[\left\langle \Phi_i \Phi_j \left| \frac{1}{r_{ij}} \right| \Phi_i \Phi_j \right\rangle - \left\langle \Phi_i \Phi_j \left| \frac{1}{r_{ij}} \right| \Phi_j \Phi_i \right\rangle \right] \tag{3.9}$$

or written in a simple form as

$$E_{el} = \sum_i \langle i|\hat{h}|i\rangle + \frac{1}{2}\sum_{ij}[\langle ij \mid ij\rangle - \langle ij \mid ji\rangle], \tag{3.10}$$

The Coulomb term is

$$J_{ij}^{\text{coul}} = \left\langle \Phi_i(1)\Phi_j(2) \left| \frac{1}{r_{12}} \right| \Phi_i(1)\Phi_j(2) \right\rangle, \tag{3.11}$$

which represents the Coulomb potential experienced by electron 1 due to electron 2 in a given position. In the Hartree approximation, the two-electron potential r_{12}^{-1} is replaced by an average of the interaction r_{12}^{-1} over all space and spin coordinates of electron 2 weighted by the probability that electron 2 occupies the volume dx_2 at x_2. It can also be written in an integral form like this, When summed over all $b \neq a$, we obtain the total averaged potential experienced by electron in ϕ_a from the $N-1$ electrons in other spinorbitals.

The exchange term arises due to the antisymmetric nature of the Slater determinant. The integral form of the exchange operator looks like

$$K_{ij}^{exch} = \left\langle \Phi_i(1)\Phi_j(2) \left| \frac{1}{r_{12}} \right| \Phi_j(1)\Phi_i(2) \right\rangle, \tag{3.12}$$

Now, the idea here is to find the molecular spinorbitals that minimize the electronic energy

$$E = \frac{\langle \psi \mid \hat{H}\psi\rangle}{\langle \psi \mid \psi\rangle}, \tag{3.13}$$

where ψ is the variational wavefunction. The electronic energy needs to be constant for small variations in the molecular orbitals ($\delta\Phi$). The constraint here is that the spinorbitals remain orthonormal and hence the spinorbitals can only be varied without destroying their orthonormality. At the minimum, both the electronic energy E and the molecular orbital overlap integrals $S_{ij} \equiv \langle \Phi_i \mid \Phi_j\rangle$ must remain constant. We can write that at minimum of E,

$$E - 2\sum_i \sum_j \epsilon_{ij} S_{ij} = \text{ constant for } \delta\Phi \tag{3.14}$$

for the restricted variation in the spinorbitals. The particular set of coefficients, ϵ_{ij}, for which the equation 3.14 is satisfied for small variations $\delta\Phi$ around the minimum are called the Lagrangian multipliers. We need to determine these Lagrange multipliers [167]. Under variation of the spinorbitals,

$$\delta E - 2\delta \sum_i \sum_j \epsilon_{ij} S_{ij} = 0, \tag{3.15}$$

Expanding E,

$$2\sum_{i=1}^{N} \delta h_{ii} + \sum_{i=1}^{N}\sum_{j=1}^{N} (2\delta J_{ij} - \delta K_{ij}) - 2\sum_{i=1}^{N}\sum_{j=1}^{N} \epsilon_{ij}\delta S_{ij} = 0, \tag{3.16}$$

Expanding the terms,

$$\delta S_{ij} = \int \delta\Phi_i^*(1)\Phi_j(1)d\tau_1 + \int \Phi_i^*(1)\delta\Phi_j(1)d\tau_1, \tag{3.17}$$

$$\delta h_{ii} = \int \delta\Phi_i^*(1)h_1\Phi_i(1)d\tau_1 + \int \Phi_i^*(1)h_1\delta\Phi_i(1)d\tau_1, \tag{3.18}$$

$$\delta J_{ij} = \int \delta\Phi_i^*(1)\Phi_j^*(2)\,(1/r_{12})\,\Phi_i(1)\Phi_j(2)d\tau_1 d\tau_2 + \int \Phi_i^*(1)\delta\Phi_j^*(2)\,(1/r_{12})\,\Phi_i(1)\Phi_j(2)d\tau_1 d\tau_2, \tag{3.19}$$

$$+ \int \Phi_i^*(1)\Phi_j^*(2)\,(1/r_{12})\,\delta\Phi_i(1)\Phi_j(2)d\tau_1 d\tau_2 + \int \Phi_i^*(1)\Phi_j^*(2)\,(1/r_{12})\,\Phi_i(1)\delta\Phi_j(2)d\tau_1 d\tau_2, \tag{3.20}$$

and similarly, for δK_{ij},

$$\delta K_{ij} = \int \delta\Phi_i^*(1)\Phi_j^*(2)\,(1/r_{12})\,\Phi_j(1)\Phi_i(2)d\tau_1 d\tau_2 + \int \Phi_i^*(1)\delta\Phi_j^*(2)\,(1/r_{12})\,\Phi_j(1)\Phi_i(2)d\tau_1 d\tau_2, \tag{3.21}$$

$$+ \int \Phi_i^*(1)\Phi_j^*(2)\,(1/r_{12})\,\delta\Phi_j(1)\Phi_i(2)d\tau_1 d\tau_2 + \int \Phi_i^*(1)\Phi_j^*(2)\,(1/r_{12})\,\Phi_j(1)\delta\Phi_i(2)d\tau_1 d\tau_2. \tag{3.22}$$

As $\delta\Phi_i(1)$ and $\delta\Phi_i^*(1)$ are independent, the respective terms must go to zero independently. Thus,

$$\left[h(1) + \sum_{j=1}^{N} \hat{J}_j(1) - \hat{K}_j(1)\right]\Phi_i(1) = \sum_{j=1}^{N} \epsilon_{ij}\Phi_j(1) \tag{3.23}$$

for $i = 1, 2, 3, \ldots$ and for a particular set of ϵ_{ij}. We see that the Lagrange multipliers turned out to be the spin orbital energies. The equation for spinorbitals can be simply written as,

$$f\,|\Phi_i\rangle = \sum_{j=1}^{N} \epsilon_{ji}\,|\Phi_j\rangle \tag{3.24}$$

where f is the Fock operator. So, to obtain a single determinant many-electron wave function, one-electron wave functions which are eigenfunctions of the one-electron Fock operator must be used. The unique set of orbitals that are solutions to the above equation for which the matrix of Lagrange multipliers is diagonal is called the set of canonical spinorbitals. An infinite number of equivalent spinorbitals can be obtained from the canonical set by unitary transformations. The Fock equation for canonical orbitals with orbital energy ϵ_i is written as

$$f\,|\phi_i\rangle = \epsilon_i\,|\phi_i\rangle\,. \tag{3.25}$$

What would be the form of the molecular orbitals? We can expand each molecular orbital as a linear combination of linearly independent basis set

$$\Phi_i(1) = \sum_{k=1}^{n} c_{ki}\chi_k(1), \tag{3.26}$$

where χ_k is the basis function and c_{ki} are the expansion coefficients. If we were to use a complete basis set, then this expansion can be used without approximation. But it is not feasible to use an infinite basis set. Hence, we resort to finite (incomplete) basis sets. Substituting the above form of the molecular orbitals in equation 3.25 multiplying χ_l on the left and integrating over the electronic coordinates,

$$\sum_{k=1}^{n} \int \chi_l(1) f(1) \chi_k(1) c_{ki} d\tau_1 = \epsilon_i \sum_{k=1}^{n} \int \chi_l(1)\chi_k(1) d\tau_1 c_{ki}, \tag{3.27}$$

which can be written in the matrix form as,

$$\mathbf{Fc} = \text{ Sce }, \tag{3.28}$$

where the overlap matrix $\mathbf{S}$ is

$$S_{kl} = \iint \chi_k(1)\chi_l(1) d\tau_1. \tag{3.29}$$

We can see that, to construct the Fock matrix $\mathbf{F}$, we need to know the molecular orbitals before hand. So, we solve the Fock equation (equation 3.28) iteratively. One starts with an initial guess of the molecular orbitals and constructs a Fock matrix. Then the solution of the Fock equation produces a new set of orbitals which is used to construct a new Fock matrix. This cycle is repeated until the solutions from two consecutive iterations are the same within a given numerical precision. At this point, the self-consistency is reached. This is why Hartree-Fock method is a self consistent field method. We need to emphasize the description of Coulomb interaction in HF theory, it assumes that an electron interacts with an average charge distribution of all the other electrons. The single Slater determinant formed from the eigenfunctions χ_k is an eigenfunction of the Hartree-Fock Hamiltonian, H_0, which is $\sum_{k=1}^{1} f(k)$, the sum of one electron Fock operators.

Hartree-Fock method is always size extensive but not always size consistent [168]. But size extensivity property does not ensure correct dissociation. Due to its single reference nature, restricted HF does not correctly describe dissociation and hence is not always size consistent hence it was not introduced.

3.1.4 Basis sets and the CBS limit

We use the linear combination atomic orbitals (L C A O) method to describe the molecular orbitals

$$\phi_i(1) = \sum_{a}^{M} c_{ai}\chi_a(1), \tag{3.30}$$

where χ_a is an atomic orbital. Here, both the atomic and molecular orbitals depend on the spatial coordinates of only one electron. For this expansion to be complete, we need to use an infinite number of basis functions or a basis set of infinite size. Such an upper bound is called the *complete basis set limit*. But for practical computational reasons, we restrict the basis set to M basis functions.

Since the basis sets are atomic orbitals, the basis set for a molecule is made of basis sets of atoms in the molecules. An atomic orbital can written as a product of radial and angular part as follows

$$\psi_{n\,\mathrm{lmA}}\left(r_A, \theta_A, \phi_A\right) = f_n\left(r_A\right) Y_l^m\left(\theta_A, \phi_A\right), \tag{3.31}$$

where n, l, m are atomic quantum numbers for an atom A and r_A, θ_A, ϕ_A describe the spatial position of an electron within atom A. There are two forms of radial basis functions generally used in computational chemistry. One is the Slater-type orbitals (STOs) inspired from bound state hydrogen wave functions which has the form

$$f_n^{STO}\left(r_A\right) = r_A^{n-1} \exp(-\eta r_A), \tag{3.32}$$

where the screening constant η differs for different basis functions. These orbitals are mostly used for free atoms and are difficult to use for molecules due to increased complexity of the integrals. The other form of orbitals is Gaussian-type orbitals (GTOs) which have the form

$$f_l^{GTO}\left(r_A\right) = r_A^l \exp(-\alpha r_A^2), \tag{3.33}$$

where α varies for different basis functions. The Gaussian form of these orbitals made the evaluation of integrals much simpler.

Wave functions calculated at short intermonomer separation are required to satisfy a mathematical condition called the correlation cusp condition. When two singlet-coupled electrons have the same coordinates i and j, the wave function exhibits the cusp [169],

$$\lim_{r_{ij}\to 0}\left(\frac{\partial \psi}{\partial r_{ij}}\right) = \frac{1}{2}\psi\left(r_{ij} = 0\right), \tag{3.34}$$

Such non-differentiable points in the wave function converges slowly. For gaussian type orbitals, the basis set error converges towards the basis set limit as a function of the basis set cardinal number, X, as $\left(X + \frac{1}{2}\right)^{-3}$. The basis set limit, E_∞, for $\mathrm{CCSD(T)}$ method is given as

$$E_X = E_\infty + A\left(X + \frac{1}{2}\right)^{-3} \tag{3.35}$$

where A is a constant. Correlation consistent and polarization consistent basis set exhibited an exponential convergence of the form [170, 171, 172] for self consistent field methods as

$$E_X = E_\infty + Ae^{-BX} \tag{3.36}$$

where A and B are constants. The equation 3.33 and equation 3.34 can be used to extrapolate the basis set limit from two or more calculations [173].

3.1.5 Basis set superposition error (BSSE)

When we consider systems with interacting subsystems, we have two set of atomic coordinates, internal and external. Internal coordinates $(A, B, C, \ldots)$ describe the internal geometries of the subsystems while the external coordinates $\left(\vec{R}_{ex}\right)$ determine the inter monomer distance and their orientation in a global coordinate system. We can define the interaction energy for a given internal configuration of the monomers as,

$$E_{\text{int}}^{AB} = E^{AB} - (E_A + E_B) \tag{3.37}$$

where E_{AB} is the electronic energy of the total system, E_A and E_B are the electronic energies of the monomers A and B. This is called the supermolecular method. Any method of electronic energy calculation can be used to evaluate the interaction energy. The advantage of the supermolecular method is that it can be applied to systems of any size. But a problem arises when we are not able to solve the Schrödinger equation exactly. So the error of approximations will manifest in the interaction energy and its precision comes into question. So, the solution to this problem is to use the same method to calculate all the energies. We have two things to consider here, the method used and the atomic orbital basis set considered. Let us consider an atomic basis set centered on A as Ω_A and on B as Ω_B. The total basis set is $\Omega = \Omega_A \cup \Omega_B$. When we calculate the energy E_{AB} in the Ω basis, the subsystems have a larger number of basis function available than in Ω_A or Ω_B separately, this artificially lowers the energy. This is called the Basis Set Superposition Error (BSSE). To remove this error, we use the basis set Ω for all E_{AB}, E_A, E_B. This procedure is called the counter-poise correction method [174].

3.1.6 Electron correlation

An electronic motion is dependent on the motion of all other electrons in a system. This interaction between electrons is refereed to as electron correlation. In reality, electrons are not fixed dots on labelled orbitals. The wave function of any given state is realistically described only when the correlation between electrons are included. Electron correlation refers to the interaction between electrons of a quantum system. In general the Hartree Fock method produces about 99% of the non-relativistic electronic energy of a system. But in most physical and chemical processes we deal with energy differences in the same magnitude as the correlation energy. To give an insight, the HF values of excitation energies of atoms are in error by 40% [175, 176], poor results of polarizabilities and transition probabilities [177, 178], an accurate account of electronic correlation is required to predict the geometries of molecules and significantly improves their description [179, 180, 181]. In systems with degenerate energy levels, single determinant approximation becomes futile, like in the case of carbon atom in the ground state, a single choice of $2p$ orbitals will always be inadequate as this state is triple degenerate. This is also referred to as static correlation. The correlation effect beyond the degenerate or quasi-degenerate levels of a given electronic state is referred to as dynamic correlation.

The correlation energy is defined as the difference between the Hartree-Fock energy and the exact (non-relativistic) energy.

$$E_{corr} = \varepsilon_{\text{exact}} - E_{HF} \tag{3.38}$$

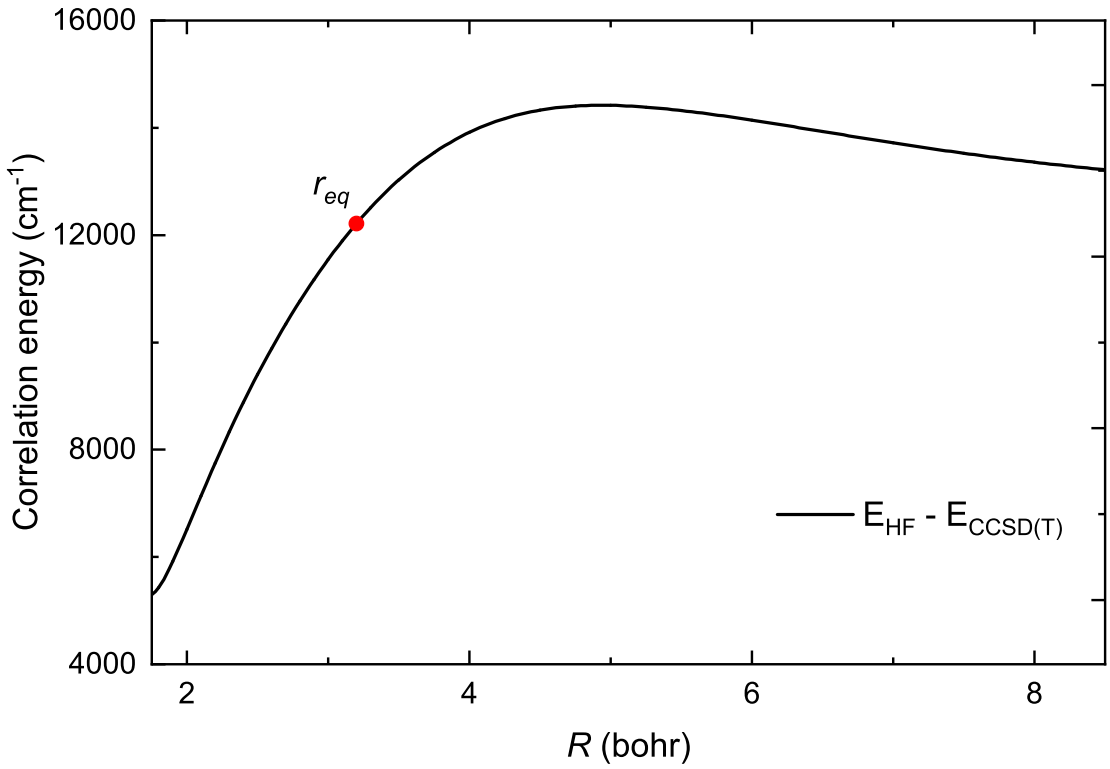

Figure 3.1: The above plot shows the contribution of correlation energy to the interaction energy between aluminium and flouride atoms. The level of theory used is CCSD(T)/aug-cc-pVTZ. The red dot indicates the position of minima of the AlF interaction.

According to the variational theorem, the Hartree-Fock energy is an upper bound to the exact energy. Hence, the correlation energy, E_{corr} , will always be negative. The Fig.3.1 shows the correlation energy calculated using CCSD(T)/aug-cc-pVTZ method. At the equilibrium bond length, r_{eq}, the correlation energy is $12214.2\ \text{cm}^{-1}$ which is 22% of the depth of the potential at CCSD(T)/aug-cc-pVTZ level of theory. It is to be noted that the correlation energy reported at $12214.2\ \text{cm}^{-1}$ is positive because it is not the total correlation energy but the contribution of correlation to the interaction energy between Al and F.

The mean-field approach ignores spatial correlation of electrons. We need to move beyond the single configuration approximation. Not only to achieve accuracy but also to arrive at a conceptually correct view of the electronic structure. There are two broad ways in which we can move forward from the Hartree-Fock method. One way is to improve on the energy or wave function generated by the HF approximation. The other way is to improve the approximation by enlarging the variational space. The most significant ab initio methods relevant to this study which are discussed in the upcoming sections are the Moller-Plesset perturbation methods (MP_n), configuration interaction methods (CI), coupled cluster methods (CC) and multi reference methods such as multiconfiguration self consistent field method (MCSCF) and Multi reference configuration interaction method (MRCI).

Before we discuss few of the relevant post-Hartree-Fock methods, let us discuss how orbital mixing (configuration mixing) actually improves the description of the electronic correlation. The most important step is to account for correlation between electron pairs. Pauli's principle allows the presence of at most 2 electrons in the same point in space and the Hamiltonian contains only up to two particle operators, hence two-electron correlation becomes most important [182]. One of the most common way to include correlation is by describing the wave function as a linear combination of the mean-field configurations.

Configuration Interaction method

In Configuration Interaction (CI) method, the many-electron wave function is expanded as

$$\Psi^{CI}(1,2,\ldots,n_e) = \sum_{a=1}^{n} c_a \Phi_a, \tag{3.39}$$

where Φ_a are the Slater determinants for n configurations included in the expansion. The Slater determinants Φ_a are constructed by replacing the occupied spinorbitals with virtual ones in the single Slater determinant (Ψ_{HF}). It is important to note that Ψ_{HF} is also included in the expansion. When only one spinorbital is replaced, the consequent determinant is called singly excited, when two spinorbitals are replaced, it is called doubly excited and so on. So, the wave function is a linear combination of Slater determinants with unknown coefficients. The CI wave functions for different states are made of the same Slater determinants but with different coefficients.

When all the possible excitations of all the electrons to all the virtual orbitals are included, the procedure is called "full CI" or full configuration interaction. The full CI approach solves the electronic Schrödinger equation exactly within the space spanned by the one-electron basis. But a full CI is computationally infeasible even for small systems due to long expansion. For practical reasons, we use the truncated version of the full CI wave function. Configuration Interaction with Single and Double excitations (CISD) is when we include just the single and doubly excited Slater determinants, CISDT is when we include single, double and triply excited Slater determinants and so on. It becomes important to analyse which excitations contributes the most to the wave function. Truncated CI methods are neither size extensive nor size consistent.

The more excitations we add to the wave function expansion, the lower the energy (variational principle). The convergence of CI expansion is slow and a large number of determinants is needed to achieve a good approximation.

Multireference CI In direct CI method, the Hartree-Fock determinant is used to construct the CI expansion by replacing the orbitals in this determinant. This is called a single reference method. But in multireference CI, a set of Slater determinants is used to form the model space. A rational analysis is required to choose these determinants. But after this, as in direct CI method, we replace the spinorbitals in the whole model space by virtual orbitals and move forward the same way as in CI method. MRCI is used to calculate the excited state interaction energies and parameter as it uses multiple reference configurations.

Let me add a bit more intuition to the difference between single reference vs multi reference methods. When one uses a single reference method like Hartree-Fock (HF), then only the HF

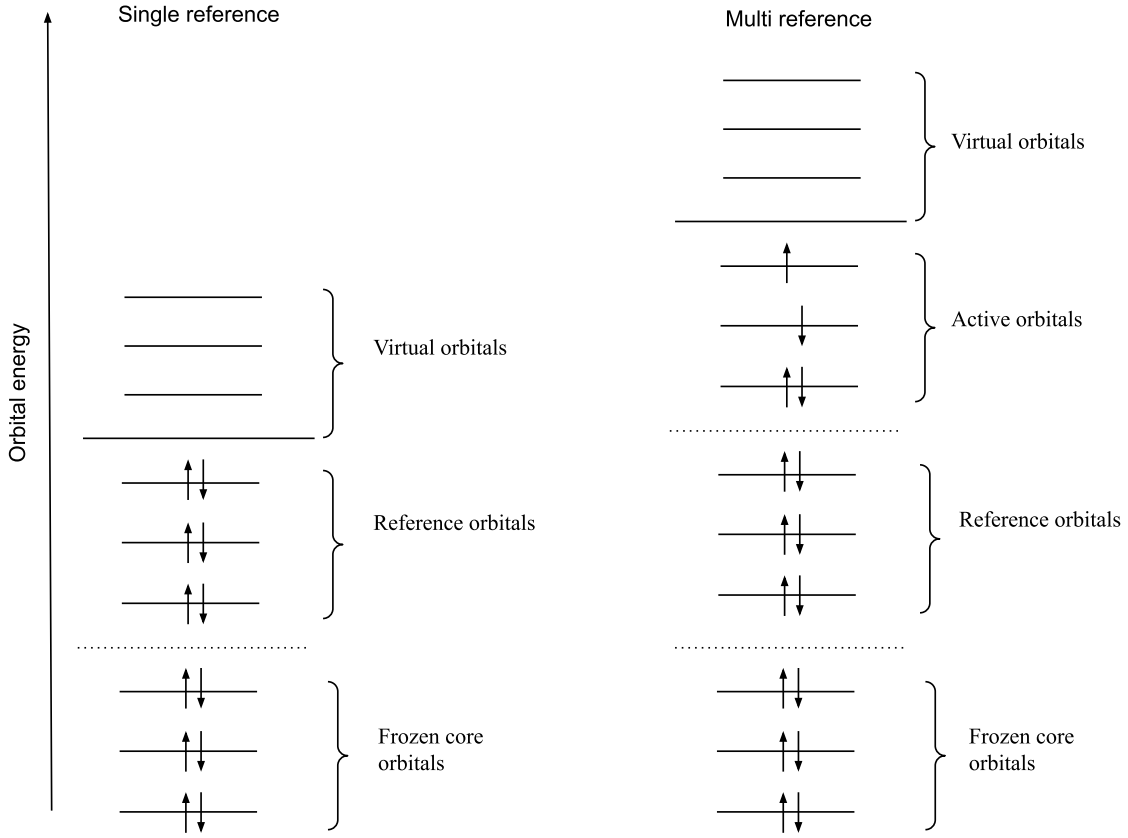

Figure 3.2: The difference between a single and a multi reference wave function is shown.

configuration will contribute the most to the CI wave function. And only the HF orbitals will be optimised. This only makes sense when the state in question is not degenerate and is energetically well separated from all the nearby states. The multi reference character of a given state can be accounted for by taking more than one configuration as a reference. Fig. 3.2 displays the basic difference between single and multi reference methods. In single reference wave function expansion, the higher excitation configurations are obtained by exciting electrons from the reference orbitals to the virtual orbitals. But in the multi reference case, for each combination of the electrons in the active orbitals, a set of excited configurations are obtained. If all the possible configurations in an active space are included, it is called complete active space (CAS) [183]. It is important to assess the multi reference nature of a system and determine the best ab initio method to implement [184].

Coupled cluster method

In coupled cluster method, the exact ground state wave function is written as [185, 186]

$$\Psi^{CC} = \exp(\hat{T})\phi_0, \tag{3.40}$$

where $\hat{T}$ is a cluster operator. It has the form

$$\hat{T} = \hat{T}_1 + \hat{T}_2 + \hat{T}_3 + \dots \tag{3.41}$$

where $\hat{T}_1$ is an operator for single excitations

$$\hat{T}_1 = \sum_{a,m} t_a^m \hat{m}^\dagger \hat{a} \tag{3.42}$$

and $\hat{T}_2$ is an operator for double excitations

$$\hat{T}_2 = \frac{1}{4} \sum_{ab,mn} t_{ab}^{mn} \hat{n}^\dagger \hat{m}^\dagger \hat{a} \hat{b}, \tag{3.43}$$

where t_a^m, t_{ab}^{mn} are excitation amplitudes, $\hat{n}^\dagger, \hat{m}^\dagger \dots$ are creation operators which refer to the virtual spinorbitals and $\hat{a}, \hat{b} \dots$ are annihilation operators referring to the occupied spinorbitals in ϕ_0. The wave operator, $\exp(\hat{T})$, ensures the size consistency of the coupled cluster method. The exponential form of the wave operator can be written as $\exp\left(\hat{T}_A + \hat{T}_B\right)\phi_0 = \exp\left(\hat{T}_A\right)\exp\left(\hat{T}_B\right)\phi_0$ unlike the truncated CI expansion $\left(\hat{T}_A + \hat{T}_B\right)\phi_0$ which gives the sum rather the product. So, a truncated CC wave function contains contributions from higher order excitations as compared to the CI expansion which contains contributions only from the same level of excitation. The coupled cluster (CC) is an iterative method. The goal of CC method is to determine the excitation amplitudes, t. Using the wave function form in equation 3.40, the Schrödinger equation is written as

$$\hat{H} e^{\hat{T}} \phi_0 = E e^{\hat{T}} \phi_0, \tag{3.44}$$

$$e^{-\hat{T}} \hat{H} e^{\hat{T}} \phi_0 = E \phi_0, \tag{3.45}$$

Multiplying from the left by the Slater determinants $|^{mn\dots}_{ab\dots.}\rangle$, which represent the excitations built from ϕ_0 into a particular cluster expansion $\hat{T} = \hat{T}_1 + \hat{T}_2 + \dots$,

$$\left\langle {}^{mn\dots}_{ab\dots..} \middle| e^{-\hat{T}} \hat{H} e^{\hat{T}} \middle| \phi_0 \right\rangle = 0. \tag{3.46}$$

There is zero on the right side due to orthogonality. CCSD method is when single and doubly excited determinants are included in the wave function expansion. The standardly used CC method is the Coupled Cluster with Single, Double and perturbative Triple excitation ($\mathrm{CCSD(T)}$). The size of the system and the basis set determines the feasibility and accuracy of the method. The standard CC method is a single reference method predominantly used for ground states and lowest energy states in a given spin mulltiplicity. In Chapter 5 we demonstrate basis set convergence and report on the computational time for increasing basis set cardinal number. The convergence of CC method towards CBS is great but its computational cost increases in the order of $\mathrm{CCSD}\left(N^6\right), \mathrm{CCSD(T)}\left(N^7\right), \mathrm{CCSDT}\left(N^8\right)$. So, they are feasible only for smaller systems.

For a given number of excited configurations, the number of CC equations is equal to the number of unknown amplitudes. As a compromise between accuracy and applicability, a non-iterative augmentation to CCSD was proposed [187]. The $\mathrm{CCSD(T)}$ method is where a non-iterative correction to the CCSD energy is added by accounting for the triple excitations in a perturbative manner. $\mathrm{CCSD(T)}$ is widely used for the improved accuracy it offers from CCSD for a relatively small computational cost [188, 189].

Explicitly correlated methods One of the main source of error in CC calculations is the basis set truncation error as discussed later in Sec.5.2. The configuration interaction type wave function with Gaussian basis sets has slow basis set convergence of energies due to the incorrect description of the correlation cusps of the wave functions [190]. Explicitly correlated methods improve the wave function description near the cusp and the correlation energy by directly introducing the inter-electronic coordinate in the wave function expansion.

In 1985 Werner Kutzelnigg proposed a method of dealing with the slow convergence by using resolution of identity (RI) to factorize the many electron integrals into one- and two-electron integrals [191]. This idea was then greatly developed into the R12 method. The R12 wave function is parameterized as

$$\psi^{CC-R12} = e^{\hat{T}}\phi_0, \tag{3.47}$$

$$\hat{T} = \hat{T}_1 + \hat{T}_2 + \hat{R}, \tag{3.48}$$

where $\hat{T}_1$ and $\hat{T}_2$ are the standard single and double excitation cluster operators. The difference here is the presence of the geminal operator, $\hat{R}$. A simple gaussian geminal operator is a product of two s-type gaussians and a correlation factor $e^{Ar_{12}^2}$.

Equation of Motion Coupled Cluster Method Equation of Motion CC (EOM-CC) method is used to compute the excitation energies with respect to the ground state. The CC wave function is taken as ground state wave function. Using a linear excitation operator, $\hat{U}_k$, ground state wave functions are transformed into k th excited state wave functions

$$\psi^{exc} = \hat{U}_k\psi^{CC} = \hat{U}_k \exp(\hat{T})\phi_0. \tag{3.49}$$

The $\hat{U}_k$ operator changes the coefficients of the CC wave function. The Schrödinger equation is written as,

$$\hat{H}\hat{U}_k \exp(\hat{T})\phi_0 = E_k\hat{U}_k \exp(\hat{T})\phi_0, \tag{3.50}$$

$\hat{U}_k$ and $\hat{T}$ commute with each other because they both contain only excitations. Multiplying with $\exp(-\hat{T})$,

$$e^{-\hat{T}}\hat{H}e^{\hat{T}}\hat{U}_k\phi_0 = E_k\hat{U}_k\phi_0, \tag{3.51}$$

The CC equation for the ground state is

$$e^{-\hat{T}}\hat{H}e^{\hat{T}}\phi_0 = E_0\phi_0, \tag{3.52}$$

Denoting the transformed Hamiltonian as $H = e^{-\hat{T}}\hat{H}e^{\hat{T}}$, multiplying equation 3.51 from left by $\hat{U}_k$ and subtracting equation 3.51 from equation 3.50 , we arrive at

$$\left[H, \hat{U}_k\right] \phi_0 = (E_k - E_0)\, \hat{U}_k \phi_0. \tag{3.53}$$

The $\hat{U}_k$ operator contains the excitation amplitudes we are solving for. We obtain the EOM-CC equation by making a scalar product of equation 3.52 with the excitations $|^{mn\ldots}_{ab\ldots..}\rangle$ included in $\hat{U}_k$,

$$| \left\langle a^{mn\ldots}_{ab\ldots} \right| \left[H, \hat{U}_k\right] \left| \phi_0 \right\rangle = (E_k - E_0) \left\langle {}^{mn\ldots}_{ab\ldots} \right| \hat{U}_k \left| \phi_0 \right\rangle . \tag{3.54}$$

We aim to solve equation 3.53 to obtain the amplitudes and excitation energies, $E_k - E_0$.

Douglas-Kroll-Hess (DKH) approach As a next step from the Schrödinger equation, relativistic effects are included using the Dirac equation. A complete description of a system must include the relativistic effects. However, keeping in mind the computational feasibility and significance, the relativistic effects are prominent for heavier atoms [192]. The one electron Dirac Hamiltonian in the presence of an external potential V is

$$H_D = c\boldsymbol{\alpha} \cdot \hat{p} + 4\boldsymbol{\beta}c^2 + V, \tag{3.55}$$

where c is the speed of light, $\hat{p}$ is the momentum operator, $\boldsymbol{\alpha}$ and $\boldsymbol{\beta}$ are the Dirac matrices

$$\boldsymbol{\alpha}_i = \begin{pmatrix} 0 & \sigma_i \\ \sigma_i & 0 \end{pmatrix}, i = (x, y, z), \boldsymbol{\beta} = \begin{pmatrix} \boldsymbol{I}_2 & 0 \\ 0 & \boldsymbol{I}_2 \end{pmatrix}, \tag{3.56}$$

the $\boldsymbol{\sigma}_i$ are the 2×2 Pauli spin matrices and $\boldsymbol{I}_2$ is a 2×2 identity matrix.

Approximations to the Dirac Hamiltonians are used to reduce the computational efforts that come with solving equations with four-component spinors. The Douglas-Kroll-Hess method is such a quasi-relativistic approximated method [193, 194]. In this method, the Dirac spinors in the presence of an external potential are decoupled by unitary transformations. This two-component approach is arrived at using block-diagonalization of the Dirac Hamiltonian,

$$\boldsymbol{U}\boldsymbol{H}_D\boldsymbol{U}^\dagger = \begin{pmatrix} H_+ & 0 \\ 0 & H_- \end{pmatrix}, \tag{3.57}$$

using a sequence of unitary transformations, $\mathbf{U} = \ldots \mathbf{U}_3\mathbf{U}_2\mathbf{U}_1\mathbf{U}_0$. The eigenvalues of $H_+$and H_-form the full Dirac spectrum. Solving the two-component equation

$$H_+\Psi = E\Psi \tag{3.58}$$

gives us the electronic solution of the Dirac equation. The block-diagonalization of the Hamiltonian occurs order by order which means this method assumes that the block-diagonal Hamiltonian can be expanded in terms of an expansion parameter (formally the external potential, V) and identify the block-diagonal terms of a given order. We have employed a DKH method of order 3 to estimate the contribution of relativistic effects in our systems. An important note is that the DKH and X2C methods modifies mostly orbitals hence the computational cost is also low for these methods.

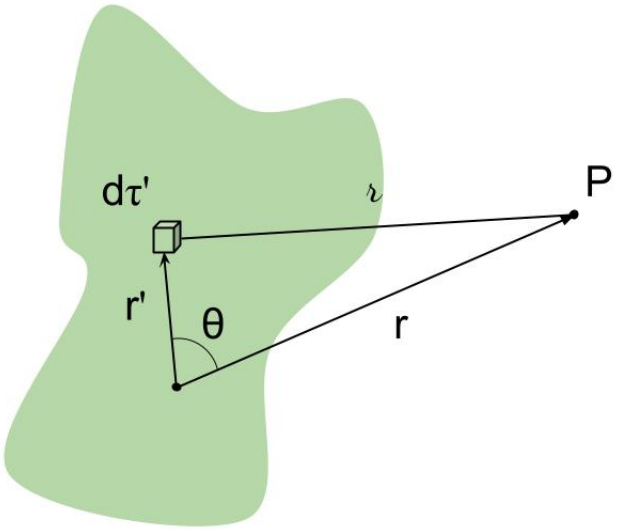

Figure 3.3: Coordinate system around an arbitrary charge distribution.

Exact two-component method (X2C) The exact two-component method (X2C) introduces scalar relativistic effects at a given level of theory [195]. In two-component methods, a unitary transformation $\boldsymbol{U}$ is used to decouple the four-component Dirac equation resulting in a block-diagonalized four component Hamiltonian, $\boldsymbol{H}$,

$$\boldsymbol{U}\boldsymbol{H}\boldsymbol{U}^{\dagger} = \begin{pmatrix} H_{+} & 0 \\ 0 & H_{-} \end{pmatrix}, \tag{3.59}$$

This block diagonalization is necessary to eliminate the negative energy part from the positive energy part (electronic part) of the Dirac Hamiltonian. In the exact two-component method $(\mathrm{X2C})$, a finite basis is used to construct just the one-electron part of the Dirac Hamiltonian and then diagonalized using a unitary transformation $\boldsymbol{U}$. The H^{+}block in equation 3.57 is the X2C Hamiltonian. The two-electron part of the Hamiltonian is approximated by just the first element, $\tilde{V}_{++}^{++}$, of the transformed V matrix since accounting for all the elements is more expensive than the four-component calculation.

3.1.7 Long range interaction

The dynamics of ultracold matter interactions is controlled by long-range interactions. Long range interactions can be describes as a power series in r, the position coordinate

$$V(r) = -\sum_n \frac{C_n}{r^n},$$

where C_n is the expansion coefficient. This definition originates from the multipole expansion. The first few dominant expansion coefficients can largely help us approximate an interaction in the long range. They are also called the long range coefficients.

Multipole expansion

The idea of multipole expansion is to substitute the Coulombic interaction by an infinite sum of interactions between multipoles. It describes the interaction between non-spherically symmetric charge distributions through the interaction of the deviations from the spherical symmetry. So it gives us formulae for multipole-multipole interaction. For an arbitrary charge distribution $\rho(r')$ Fig. 3.3, the potential at a point $\mathbf{P}$ far from the charge distribution ($r >> r'$) is

$$V(\mathbf{r}) = \int \frac{1}{\mathscr{r}} \rho(\mathbf{r}')\, d\tau', \tag{3.60}$$

Here,

$$\mathscr{r}^2 = r^2 + r'^2 - 2rr'\cos(\theta), \tag{3.61}$$

and

$$\frac{1}{\mathscr{r}} = \frac{1}{r} \frac{1}{\sqrt{1 + \left(\frac{r'}{r}\right)^2 - 2\frac{r'\cos(\theta)}{r}}} \tag{3.62}$$

Reminding ourselves of the infinite series $(1+x)^s = \sum_{n=0}^{\infty} \frac{s!}{n!(s-n)!} x^n$, expanding $\frac{1}{\mathscr{r}}$ as

$$\frac{1}{\mathscr{r}} = \frac{1}{r}\left[1 - \frac{1}{2}\frac{r'}{r}\left(\frac{r'}{r}2\cos\theta\right) + \frac{3}{8}\left(\frac{r'}{r}\right)^2\left(\frac{r'}{r} - 2\cos\theta\right)^2\right) + \ldots\Bigg]. \tag{3.63}$$

Collecting terms with same powers of $\frac{r'}{r}$,

$$\begin{aligned}\frac{1}{\mathscr{r}} &= \frac{1}{r}\left[P_0(\cos\theta) + \frac{r'}{r}P_1(\cos\theta) + \left(\frac{r'}{r}\right)^2\right) P_2(\cos\theta) + + \left(\frac{r'}{r}\right)^3\right) P_3(\cos\theta) + \ldots\Bigg] \\ &= \frac{1}{r}\sum_{n=0}^{\infty}\left(\frac{r'}{r}\right)^n P_n(\cos\theta),\end{aligned} \tag{3.64}$$

$$V(r) = \frac{1}{r}\sum_{n=0}^{\infty}\int_{\tau'}\rho\left(r'\right)\left(\frac{r'}{r}\right)^{n} P_n(\cos\theta)d\tau'$$
$$= \frac{1}{r}\int_{\tau'}\rho\left(r'\right)d\tau' + \frac{1}{r^2}\int_{\tau'}\rho\left(r'\right)r'\cos\theta + \frac{1}{r^3}\int_{\tau'}\rho\left(r'\right)r'^2\left(\frac{3}{2}\cos\theta^2 - \frac{1}{2}\right)d\tau' + \ldots. \tag{3.65}$$

The first term (for $n = 0$) is the monopole contribution, the second is the dipole term $(n = 1)$, third the quadrupole term and so on. For a coordinate system of two particles in Fig. 3.4 where the z axes are colinear and x and y axes are parallel, the Coulomb interaction can be expanded as following [196],

$$\frac{q_1 q_2}{r_{12}} = \sum_{k=0}^{n_k}\sum_{l=0}^{n_l}\sum_{m=-s}^{m=+s} A_{kl|m|}R^{-(k+l+1)}\hat{M}_a^{(k,m)}(1)\hat{M}_b^{(l,m)}(2), \tag{3.66}$$

where the $A_{kl|m|} = (-1)^{l+m}\frac{(k+l)!}{(k+|m|)!(l+|m|)!}$, n_k and n_l denote the quantum states of the individual particles and $s = \min(k,l)$. Here, the m th component of the 2^k pole of particle 1 in coordinate system a is $\hat{M}_a^{(k,m)}(1)$ given by

$$\hat{M}_a^{(k,m)}(1) = q_1 r_{a1}^k P_k^{|m|}\left(\cos\theta_{a1}\right)\exp\left(im\phi_{a1}\right), \tag{3.67}$$

where $P_k^{|m|}$ are the associated Legendre polynomials with $|m| \leq k$. The total multipole moment of a system would be the sum of the same moment operators of individual particles. To give an insight, the monopole of a particle is its charge, q, the z-component of the dipole moment operator is qz and so on. The operator of the 2^k pole moment will be a polynomial of k th degree in x, y and z. As a general rule, the multipole expansion converges as long as the two charge distributions do not overlap. The useful property of this method is that we can interpret the interaction energy in terms of the charges, dipoles, quadrupoles, ..., moments of the particles. In reality, only a truncated form of the multipole expansion becomes feasible and usually multipole moments higher than $k = 3$ is neglected.

Polarizability Polarizability of a neutral molecule is a basic property that characterises the lowest-order response of the molecule to an external electric field. It is important in collision phenomena where the polarizabilities determine the interaction of a molecule with other neutral or charged particles. So, the polarizability relates the induced dipole moment to the external electric field E.

$$p = \alpha \cdot E. \tag{3.68}$$

In matrix notation,

$$\begin{pmatrix} p_x \\ p_y \\ p_z \end{pmatrix} = \begin{pmatrix} \alpha_{xx} & \alpha_{xy} & \alpha_{xz} \\ \alpha_{yx} & \alpha_{yy} & \alpha_{yz} \\ \alpha_{zx} & \alpha_{zy} & \alpha_{zz} \end{pmatrix}\begin{pmatrix} E_x \\ E_y \\ E_z \end{pmatrix},$$

In the presence of a static electric field, the polarizability tensor is symmetric, $(\alpha_{ij} = \alpha_{ji})$.

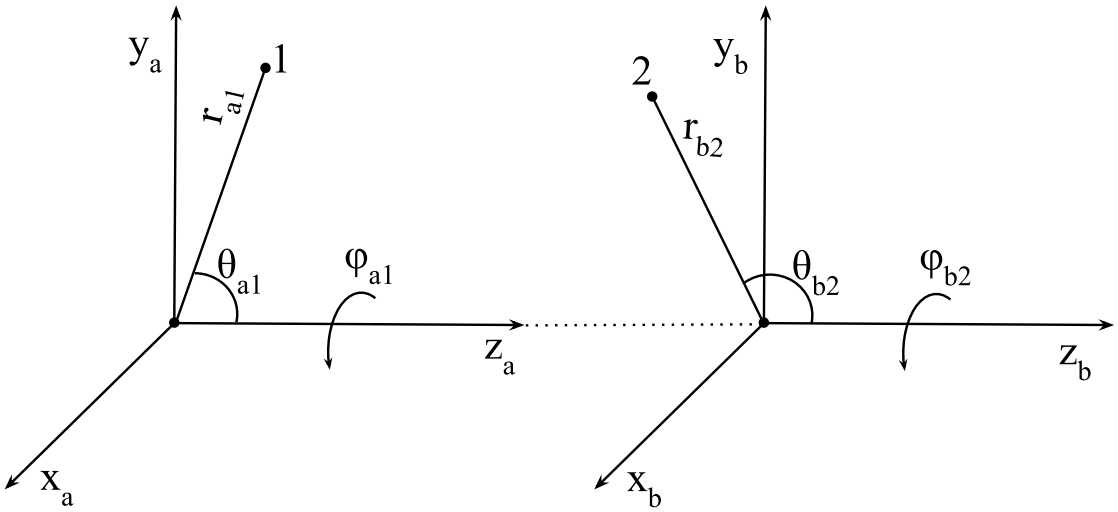

Figure 3.4: The coordinate system used for multipole expansion.

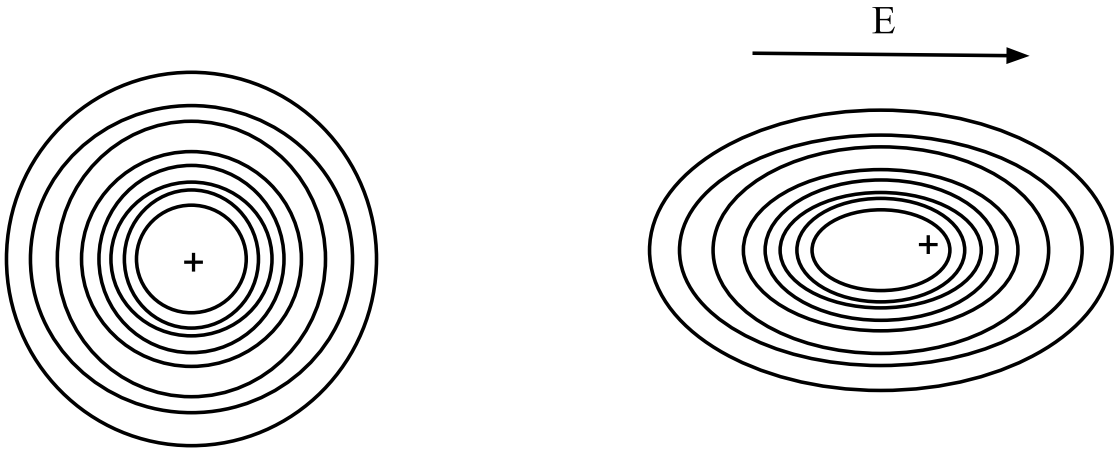

Figure 3.5: A representative figure of the spherical charge distribution of of hydrogen atom. In the presence of an external electric field, the atom acquires an induced dipole moment because the electron charge distribution is distorted and displaced from the nucleus.

Perturbation theory of intermolecular forces

Molecules interact through their electric moments and polarizabilities in long range. Intermolecular interaction energy becomes small at long distances, about 10^{-3} to 10^{-8} times total energy, it is suitable to use perturbation theory to describe it. For two interacting systems A and B, the individual Schrödinger equations are

$$H_A^0 \phi_A^0 = E_A^0 \phi_A^0, \tag{3.69}$$
$$H_B^0 \phi_B^0 = E_B^0 \phi_B^0. \tag{3.70}$$

Coulombic interactions between pairs of charged particles is considered as the perturbation. The general form of the interaction is $V = \sum_i \sum_j q_i q_j / r_{ij}$ where r_{ij} is the distance between the particles i and j. The zeroth order wave function is written as a product of the ground state wave functions of the molecules.

$$\psi_{gs}^0 = \phi_A^0 \phi_B^0. \tag{3.71}$$

This is referred to as the polarization approximation, a long range approximation to the interaction energy. When the interacting subsystems are far enough from each other, their electrons become distinguishable and the wave function equation **??**, which essentially describes a noninteracting system, can be used. The first order correction to energy is

$$E_0^{int} = \langle \psi_0 | V | \psi_0 \rangle \,. \tag{3.72}$$

The electrostatic interaction energy represents the classical Coulombic interaction between two molecular charge distributions. The second order energy represents the induction and dispersion energies. We split the summation as,

$$E_{ind}(A \to B) = \sum_{n_B}{}' \frac{|\langle \psi_{A,0}\psi_{B,n_B} \mid V \mid \psi_{A,0}\psi_{B,0} \rangle|^2}{(E_{B,0} - E_{B,n_B})}, \tag{3.73}$$

$$E_{\text{ind}}\,(B \to A) = \sum_{n_A}{}' \frac{|\langle \psi_{A,n_A}\psi_{B,0} \mid V \mid \psi_{A,0}\psi_{B,0} \rangle|^2}{(E_{A,0} - E_{A,n_A})}, \tag{3.74}$$

$$E_{disp} = \sum_{n_A}{}' \sum_{n_B}{}' \frac{|\langle \psi_{A,n_A}\psi_{B,n_B} \mid V \mid \psi_{A,0}\psi_{B,0} \rangle|^2}{(E_{A,0} - E_{A,n_A}) + (E_{B,0} - E_{B,n_B})}. \tag{3.75}$$

The prime in the above summation means that $n_A = n_B = 0$ is excluded. The induction energy has two parts, one is the polarization energy when unperturbed molecule A perturbs molecule B and vice versa. The dispersion term is when both the molecules are temporarily in an excited state. Dispersion interaction is a correlation effect.

The long range coefficients, C_n, in the equation $E_{int} = \sum_n C_n R^{-n}$ shape the long range behavior of the electrostatic, induction and dispersion interactions and they are related to the property of monomers. The expression of C_n coefficients for basic atom-molecule interaction is

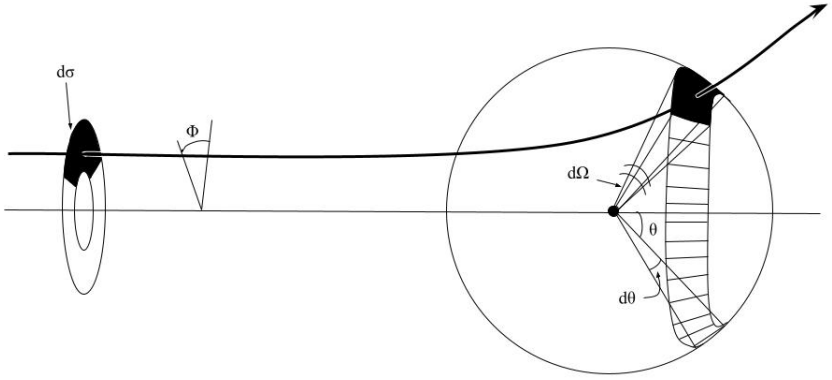

Figure 3.6: Particles incident through the area $d\sigma$ scattering into the solid angle $d\Omega$.

discussed here [197, 198]. The isotropic dispersion, $C_{6,0}^{dis}$ coefficient is estimated from the mean dipole polarizability, $\bar{\alpha}$, of the constituents using the formula [199]

$$C_{6,0}^{\text{dis}} = \frac{3}{\pi}\int_0^\infty \bar{\alpha}^{\text{mol}}(i\omega)\alpha^{\text{atom}}(i\omega)d\omega. \tag{3.76}$$

The anisotropic dispersion coefficient associated with $P_2(\cos\theta)$ term in the Legendre expansion is calculated using the anisotropy of the polarizability of the molecule, $\Delta\alpha^{\text{mol}}$, as

$$C_{6,2}^{\text{dis}} = \frac{1}{\pi}\int_0^\infty \Delta\alpha^{\text{mol}}(i\omega)\alpha^{\text{atom}}(i\omega)d\omega, \tag{3.77}$$

The induction contribution to the C_6 coefficient can be written as

$$C_{6,0}^{\text{ind}} = C_{6,2}^{\text{ind}} = \mu_{\text{mol}}^2\alpha^{\text{atom}}(0), \tag{3.78}$$

where μ_{mol} is the electric dipole moment of the molecule and $\alpha^{\text{atom}}(0)$ is the static dipole polarizability of the atom.

We should note that a product description of the wave function is not antisymmetric under electron exchange (between the sub systems). This would give us a poor description of the exchange forces between electrons, especially at shorter ranges.

3.2 Scattering theory

In this section, we will go through a basic overview of scattering theory and the quantities relevant to this study. Understanding of collisions between ultracold atoms and molecules is a essential for many aspects of ultracold experiments. In elastic collisions, the atoms and molecules remain in the same internal state and the energy of the relative motion remains constant. Inelastic collisions involve change in the internal state of atoms or molecules and energy is released.

Considering the quantum scattering of two particles, the interaction potential $V(r)$ goes to 0 as $r \to \infty$. The particles at $r \to \pm\infty$ are essentially free particles and these asymptotic states

can be matched to arrive at the scattering wave function. For $r \to \infty$, the total scattering wave functions takes the asymptotic form,

$$\psi(r,\theta) \sim \psi_0(r) + f(k,\theta).\frac{e^{ikr}}{r}.$$

Here, $\psi_0(r)$ is the unscattered wave function, assumed to be a plave wave (free particle). r is the distance between the particles, $\vec{k}$ is the wave vector, $f(\theta)$ is the scattering amplitude and θ is the scattering angle. The scattering amplitude encapsulates the angular distribution of the scattering. The scattering amplitude is related to the differential cross section as

$$\frac{d\sigma}{d\omega} = |f(k,\theta)|^2, \tag{3.79}$$

where ω is the solid angle. The elastic cross section is obtained by integrating over all solid angles. We need to solve the Schrödinger equation of the relative motion of particles,

$$\left[-\frac{\hbar^2}{2\mu}\nabla_r^2 + V(r)\right]\psi(r) = E\psi(r), \tag{3.80}$$

where μ is the reduced mass. For a collision of two spherically symmetric particles, wave function $\psi(r,\theta,\phi)$ can be expanded as a sum of spherical harmonics and radial functions,

$$\psi(r,\theta,\phi) = \sum_{l,m} \frac{R_l(r)}{r} Y_l^m(\theta,\phi), \tag{3.81}$$

where l is the relative angular momentum and m its projection onto a space-fixed z-axis. The spherical harmonics $Y_l^m(\theta,\phi)$ are the eigenstates of the angular momentum operator. We should note that for only two coordinates (r,θ) is required to describe an atom while molecules require three coordinates (r,θ,ϕ). For an isotropic potential, there is no coupling between different partial waves. The radial function $R_l(r)$ is an eigenfunction of the equation,

$$\left[-\frac{\hbar^2}{2\mu}\frac{d^2}{dr^2} + \frac{l(l+1)}{2\mu r^2} + V(r)\right]R_l(r) = ER_l(r), \tag{3.82}$$

where the second term is the centrifugal barrier which is non-existent for the s-wave and is increasingly repulsive for $l > 0$. For $E < 0$, a discrete set of bound states can be obtained. For $E > 0$, we arrive at a continuous spectrum of scattering states. At $r \to \infty, V(r) \to 0$, the asymptotic solutions to the equation 3.77 (for $V = 0$) is expressed using spherical Bessel and Neumann functions $j_l(kr)$ and $n_l(kr)$ as

$$R_l(r) = A_l r j_l(kr) + B_l r n_l(kr), \tag{3.83}$$

where A_l and B_l are normalization constants. In the asymptotic limit,

$$\lim_{r\to\infty} j_l(kr) \to \frac{\sin\left(kr - \frac{l\pi}{2}\right)}{kr} \tag{3.84}$$

and

$$\lim_{r\to\infty} n_l(kr) \to -\frac{\cos\left(kr - \frac{l\pi}{2}\right)}{kr}, \tag{3.85}$$

The radial wave function is be written as

$$R_l(r) \xrightarrow{r\to\infty} \sqrt{\frac{2\mu}{\pi k}}\left[\sin\left(kr-\frac{l\pi}{2}\right)-\tan\delta_l(k)\cos\left(kr-\frac{l\pi}{2}\right)\right], \tag{3.86}$$

where δ_l denotes the phase shift. The incoming and outgoing wave can only differ by a phase owing to conservation of probability. Calculating the phase shift for a particular potential gives all the information about the scattering problem. It is defined as,

$$\delta_l = \arctan\left(-\frac{B_l}{A_l}\right), \tag{3.87}$$

Comparing the equation 3.93 to equation 3.72 , the scattering amplitude can be expressed in terms of the phase shifts as

$$f(k,\theta) = \frac{1}{k}\sum_{l=0}^{\infty}(2l+1)\sin\delta_l P_l(\cos\theta) \tag{3.88}$$

and the scattering cross section $\sigma(k)$ is

$$\sigma(k) = \sum_{l=0}^{\infty}\sigma_l(k) = \frac{4\pi}{k^2}\sum_{l=0}^{\infty}(2l+1)\sin\left(\delta_l(k)\right)^2 \tag{3.89}$$

$$= \frac{4\pi}{k^2}\sum_{l=0}^{\infty}(2l+1)\left|1-S_l\right|^2, \tag{3.90}$$

where $P_l(\cos\theta)$ denotes the Legendre polynomials, S_l denotes the S-matrix elements. The S-matrix is an important quantity in scattering problems. It links the initial and final state of a collision. It is related to the phase shift as follows,

$$S_l = e^{2i\delta_l}. \tag{3.91}$$

3.2.1 Coupled channel scattering theory

In the Born-Oppenheimer approximation, introduced in Sec. 3.1.1, we solve the electronic and nuclear Schrödinger equations separately. The solution of the electronic Schrödinger equation provides the electronic wavefunction ψ_{el} and electronic emergies E_{el} for a particular nuclear configuration. Such a calculation will be repeated for a range of nuclear configurations. The resultant set of electronic energy, which parametrically depends on the nuclear coordinates, is now used as a potential in the Schrödinger equation of the nuclear motion. The total Schrödinger equation for a 2-body collision in the centre-of-mass frame is written as,

$$\hat{H}(R,\beta)\psi(R,\beta) = E\psi(R,\beta), \tag{3.92}$$

$$\left[-\frac{\hbar^2}{2\mu}\frac{1}{R}\frac{d^2}{dR^2}R + \frac{\hbar^2\hat{L}^2}{2\mu R^2} + \hat{H}_{\text{int}}(\beta) + V(R,\beta)\right]\psi(R,\beta) = E\psi(R,\beta), \tag{3.93}$$

where R is the inter-monomer separation and β represents all the other coordinates, μ is the reduced mass for the collision, E is the collision energy, $\hat{H}_{\text{int}}$ is the internal Hamiltonian of the colliding monomers at infinite seperation, $\hat{L}$ is the relative angular momentum operator of the monomers around each other and $V(R, \beta)$ is the interaction potential between the two monomers, the electronic energy in our case.

We solve equation 3.93 to obtain the total energy of the system. The wave function for the translational, vibrational and rotational motions will be obtained. Unlike a two-particle isotropic scattering where there is only one channel that connects the initial and final state of the scattering event, more complex scattering with more degrees of freedom has many channels, i.e, for one initial state there can be many possible final states that the particles can end up in. Each of these combinations will constitute a channel. Coupling between these channels can induce inelastic processes, so the interaction potential becomes a matrix that captures all these couplings.

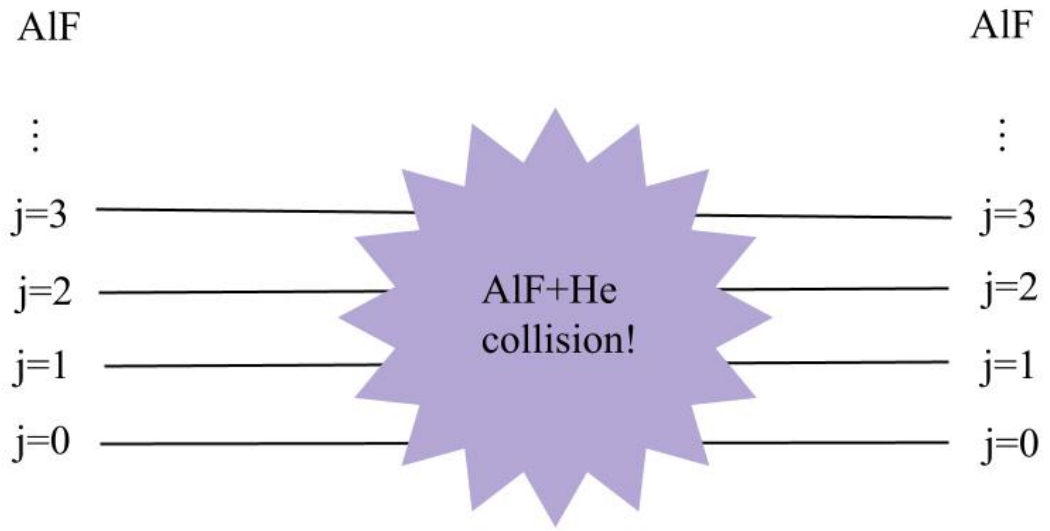

Figure 3.7: In the collision of AlF (rigid rotor) and He, the rotational states of AlF are coupled due to the anisotropic interaction. Both elastic and inelastic collisions are possible.

We use coupled channel approach to calculate the wave function and cross sections. Coupled channel approach is when the radial coordinate, R, is treated by numerical propagation on a grid and using a basis set for the rest of the coordinates [200, 201, 202, 203, 204]. The wave function can be expanded as follows,

$$\psi(R, \beta) = R^{-1} \sum_j \phi_j(\beta)\psi_j(R), \tag{3.94}$$

Here β refers to the rest of the coordinates. The functions $\phi_j(\beta)$ are basis sets for motion in the coordinates β. The function $\psi_j(R)$ are the radial channel functions for each channel j. Such an expansion of the wave function gives us a coupled differential equation for the channel functions.

Coupled equations are propagated using the Manolopoulos diabatic modified logderivative [205] and the Alexander-Manolopoulos Airy propagator [206].

4 AlF

AlF is a closed shell molecule with a $X^1\Sigma^+$singlet ground state and a dissociation energy of about $57000\ \mathrm{cm}^{-1}$. Recent experimental research on AlF reports promising results for ultracold AlF [144]. A spectroscopic characterisation of the $a^3\Pi$ state of aluminium monoflouride molecule was done using a jet-cooled, pulsed molecular beam. AlF is produced from SF_6 gas reacting with aluminium atoms which are ablated from a rotating aluminium rod with a Nd:YAG laser. Due to supersonic expansion of AlF into the gas chamber, the translational temperature is ≈ 3 K and the rotational temperature is ≈ 5 K. An important conclusion is that the transitions from $a^3\Pi, \nu = 0$ state to the $X^1\Sigma^+, \nu = 1$ and $\nu = 2$ state are more than two and five orders of magnitude smaller than to the $\nu = 0$ state. The lifetime of the rotational levels of $a^3\Pi, \nu = 0$ state were also experimentally estimated [161].

In this chapter the ab initio calculations for the ground and excited state of AlF molecule are reported. We also discuss the convergence of interaction energy with basis set cardinal number and with different levels of theory. I also report dipole moment and dipole polarizability of AlF in $X^1\Sigma^+$and $a^3\Pi$ states.

4.1 Methods

4.1.1 *Ab initio* methods

Coupled cluster with single, double excitations and perturbative inclusion of triples is the highest level of theory used to calculate the ground state $\left(X^1\Sigma^+\right)$and excited state $\left(a^3\Pi\right)$ potential energy curves of aluminium monoflouride molecule. We have reported the convergence of interaction energy for increasing basis set cardinal numbers, usage of midbonds, inclusion of core electron correlation. The interaction energy is calculated using the supermolecular method,

$$V_{\text{int}}(r) = E_{AlF}(r) - E_{Al}(r) - E_F(r), \tag{4.1}$$

where E_{AlF} is the energy of the molecule AlF and E_{Al}, E_F are the energies of the aluminium and flourine atoms. The interaction energy depends on only one coordinate which is the bond length, r_{AlF}. The basis set superposition error is countered with the counterpoise correction [174] meaning both the monomer and dimer energy calculations are carried out using the dimer basis set.

An important distinction to note is for AlF, an ionic molecule, it is only reasonable to use a single reference wave function ansatz for a short range of the bond length. As ionic molecules dissociate at large distances, the perturbatively added triple excitation in $\mathrm{CCSD(T)}$ becomes anomalous and CCSD does not correctly describe the multi reference character of the electronic wave function. In our case, $\mathrm{CCSD(T)}$ stopped converging around 8 bohr for a molecule with a bond length of 3.136 bohr.

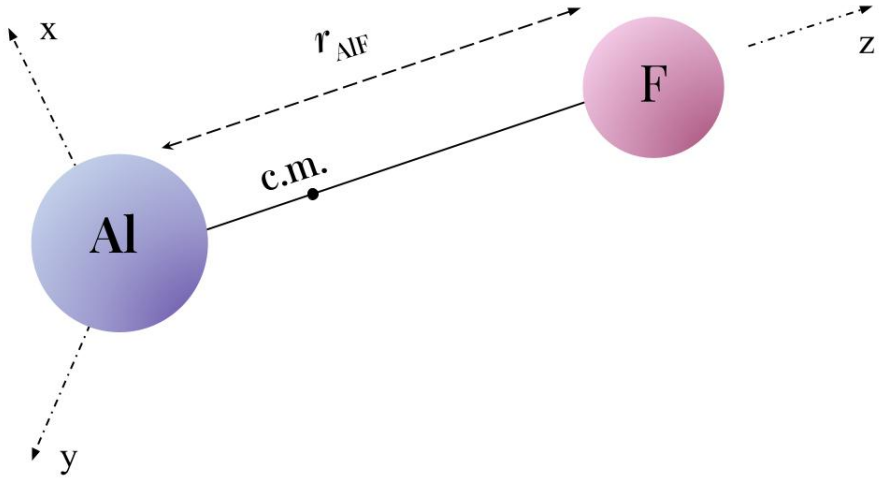

Figure 4.1: AlF molecule. The bond length, r_{AlF} and centre of mass (c.m) are indicated.

The core-electron correlation energy contribution to the interaction energy reported in Fig. 4.4 and Fig. 4.7 is calculated using the following formula,

$$V_{\text{core}} = V_{\text{core-valence}} - V_{\text{valence}} \tag{4.2}$$

where $V_{\text{core-valence}}$ is the interaction energy of AlF molecule calculated when the core excitations are included while V_{valence} is the interaction energy of AlF molecule without including core excitations. The level of theory used is $\mathrm{CCSD(T)}$ /aug-cc-pCVXZ.

4.1.2 Dipole moment and polarizability

Polarizability describs the tendency of the electron cloud of the molecule to get distorted by an external electric field. In the presence of an external electric field, the charge distribution of a particle can be characterised by polarizabilities. The electric multipole moments are used to write the new charge distribution. The dipole moment p, which is the lowest order multipole moment of a neutral particle can be written as

$$p = p_0 + \alpha \cdot \varepsilon + \frac{1}{2}\beta\varepsilon^2 + \ldots, \tag{4.3}$$

where p_0 is the permanent electric dipole moment, α gives the lowest order induced dipole moment of a particle and ε is the electric field. For symmetric species, the permanent electric dipole moment $p_0 = 0$ but in our case, the AlF molecule is a heteronuclear diatomic molecule which has a permanent electric dipole moment. α and β represent polarizability and hyperpolarizability tensors respectively. Finite-field method calculates the energy of the molecule in different external electric fields and the polarizability is extracted using numerical differentiation.

Table 4.1: Convergence of equilibrium parameters of AlF molecule calculated using $\mathrm{CCSD(T)}$.

Basis sets	r_{eq}(bohr)	$D_{eq}\left(\mathrm{cm}^{-1}\right)$	$B_{eq}\left(\mathrm{cm}^{-1}\right)$	$\omega_{eq}\left(\mathrm{cm}^{-1}\right)$
Valence electron correlated				
aug-cc-pVDZ	3.2263	52633.4	0.51874	738.8
aug-cc-pVTZ	3.1772	55016.4	0.53490	771.7
aug-cc-pVQZ	3.1549	56417.1	0.54248	796.8
aug-cc-pV5Z	3.1451	56879.1	0.54589	800.5
aug-cc-pV5Z+MB	3.1446	56922.8	0.54606	800.7
aug-cc-pV5Z+MB+rel	3.1445	56821.8	0.54610	799.4
Core and valence electrons correlated				
aug-cc-pCVDZ	3.2213	52740.1	0.52034	738.1
aug-cc-pCVTZ	3.1557	55428.9	0.54220	781.6
aug-cc-pCVQZ	3.1346	56789.4	0.54955	799.6
aug-cc-pCV5Z	3.1296	57112.7	0.55131	801.9
aug-cc-pCV5Z+MB	3.1289	57162.2	0.55155	803.0
aug-cc-pCV5Z+MB+rel	3.1288	57058.5	0.55157	801.6
Experimental results				
	3.125 [207]	58409 [208]	0.540 [209]	802.26 [210]

4.2 Results

4.2.1 Potential energy curves

Ground state

Table. 4.2.1 reports the equilibrium parameters r_{eq} (equilibrium distance between Al and F), D_{eq} (equilibrium depth), B_{eq} (rotational constant at equilibrium position), ω_{eq} (vibrational constant of the Al-F interaction) for various basis sets, with usage of mid-bonds and relativistic corrections. The deepest well is observed for $\mathrm{CCSD(T)}$ /aug-cc-pCV5Z+midbond for which the equilibrium bond length is 3.128 bohr, the vibrationally averaged bond length we used for AlF ground state is 3.136 bohr. The scalar relativistic corrections are incorporated using DKH Hamiltonian. With both valence and core-valence basis set, the scalar relativistic corrections are not sensitive to the core electron correlation. When we compare the bond lengths for valence and core-valence basis sets, we see a consistent trend where we obtain shorter bond lengths for core-valence basis sets. Core electron correlation reduces the bond length by about $0.67\%, 0.64\%$ and 0.49% for the basis set cardinal numbers, $X = \mathrm{T}, \mathrm{Q}, 5$ respectively.

Fig. 4.2 shows the convergence of $\mathrm{CCSD(T)}$ interaction energies of AlF molecule with increasing basis set cardinal numbers for aug-cc-pVXZ basis set. The addition of midbonds to the basis set lowers the energy negligibly by about $43\ \mathrm{cm}^{-1}$. Even the smallest aug-cc-pVDZ basis set captures about 92% of the total interaction energy. The change in position of the global minima between aug-cc-pV5Z+MB and aug-cc-pVDZ is -0.08 bohr. The use of midbonds only improves the well depth by about $50\ \mathrm{cm}^{-1}$, which is 0.08%.

Fig. 4.3 shows the convergence of the interaction energy with respect to the different levels of

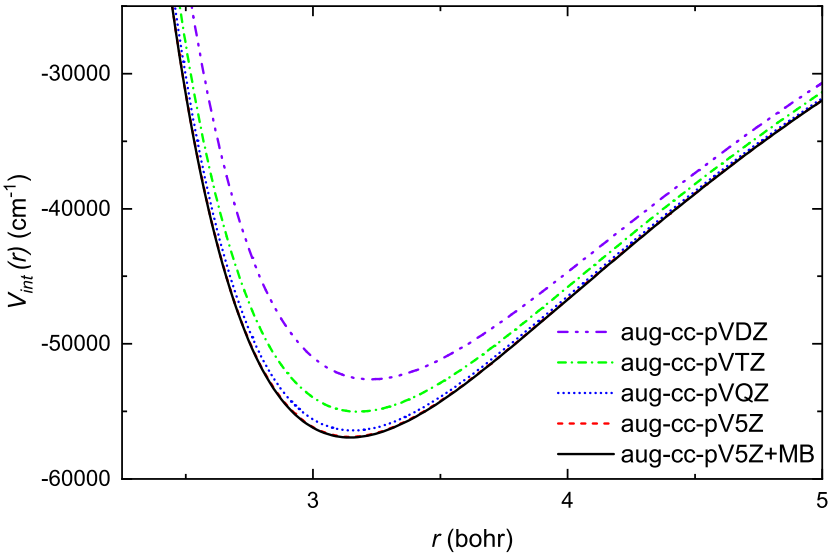

Figure 4.2: Convergence of ground state potential energy of AlF with respect to increasing basis set cardinal number of aug-cc-pVXZ basis set. The level of theory used is CCSD(T). The aug-cc-pV5Z and aug-cc-pV5Z+MB curves overlap in the above plot.

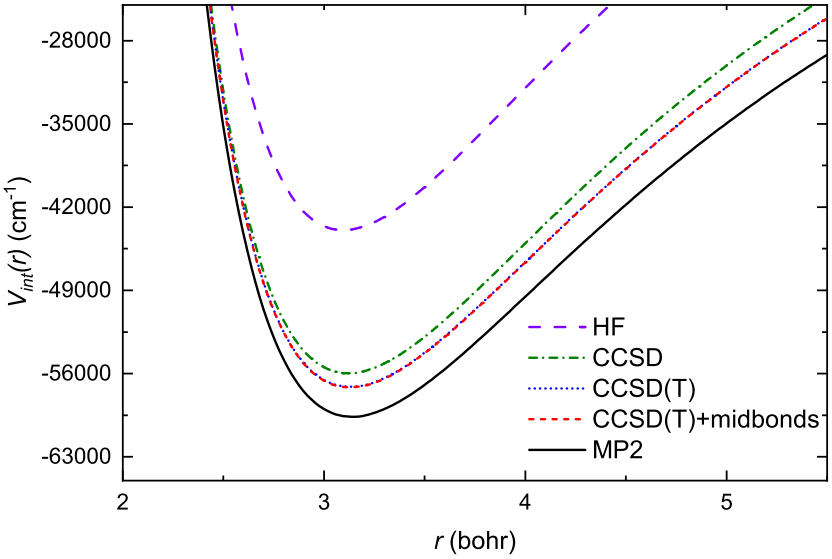

Figure 4.3: The ground state potential energy curves of AlF calculated at different levels of theory. The basis set used is aug-cc-pCV5Z. The curves of CCSD(T) and CCSD(T)+midbonds overlap in the above plot.

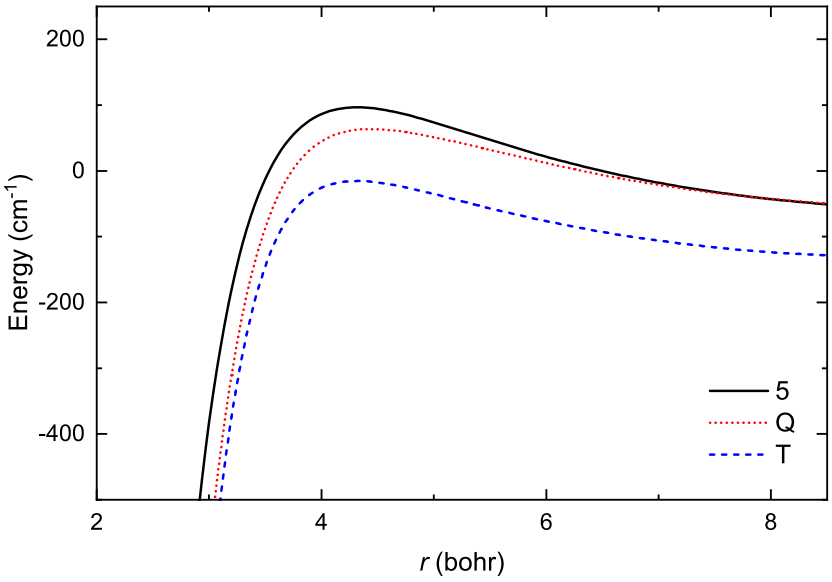

Figure 4.4: The core-electron correlation energy contribution to the ground state interaction energy for core-valence basis set (aug-cc-pCVXZ) for three basis set cardinal numbers. $\mathrm{CCSD(T)}$ method is used.

theory. The Hartree-Fock curve is $43940\ \mathrm{cm}^{-1}$ deep, the correlation energy contribution to the interaction energy is $13196\ \mathrm{cm}^{-1}$. The deepest curve observed is from the MP2 calculation.

There are cases when MP2 method overestimates the interaction energy [211, 212]. Here, the MP2 method has overestimated the interaction energy by about $2500\ \mathrm{cm}^{-1}$ which is 4% of the well depth. The depth of the potential D_e is $57152.2\ \mathrm{cm}^{-1}(\mathrm{CCSD(T)}/$ aug-cc-pCV5Z+MB). The position of global minima remains unchanged in all levels of theory reported in Fig. 4.3

Fig. 4.4 reports the core-electron correlation energy contribution to the interaction energy. For decreasing bond length, the contribution of the core electrons increases. It is lowest around $r =$ 4 bohr and approaches a constant negative value for longer bond lengths which is also indicative of the multireference nature of the electronic wavefunction. The core-valence basis set is bigger than the valence electron basis set which improves the overall description of the wavefunction so the upward shift from the aug-cc-pCVTZ curve cannot be entirely attributed to just increase in correlation energy contribution. As the atoms approach the repulsive wall, the core electrons naturally have bigger contributions which is what we observe. For increasing basis set cardinal number, the accuracy of the interaction energy increase but the core electron contribution as such reduces.

The scalar relativistic effects are added using the DKH protocol. Fig. 4.5 shows the relativistic correction. Curves obtained with valence and core-valence basis set almost overlaps with just a marginal difference at longer bond lengths.

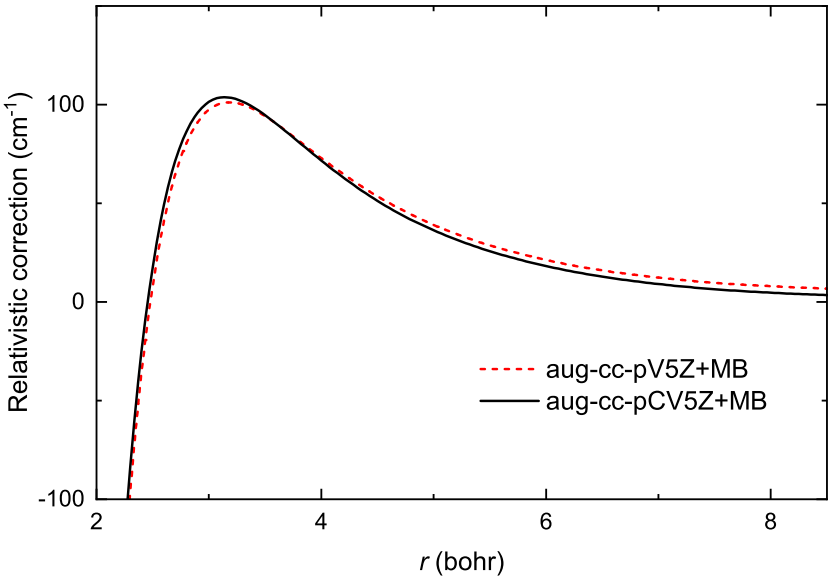

Figure 4.5: Ground state scalar relativistic correction to the interaction energy obtained with the DKH Hamiltonian,

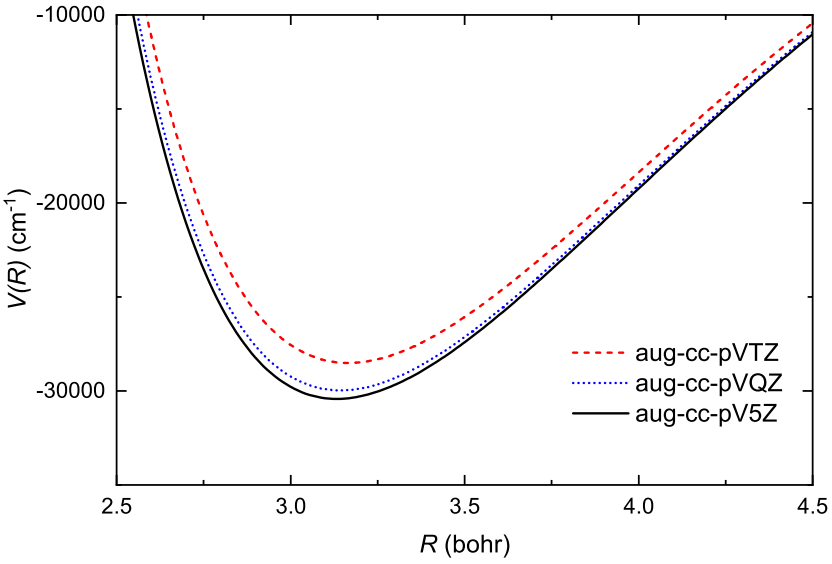

Figure 4.6: Potential energy curve for the $a^3\Pi$ state of AlF for three basis sets obtained with CCSD(T).

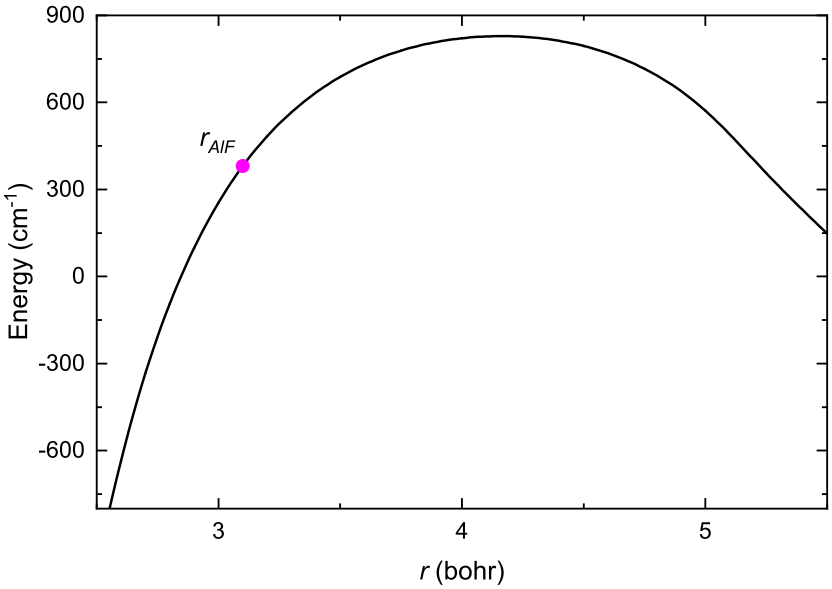

Figure 4.7: The correlation energy contribution to the interaction to the $a^3\Pi$ state interaction energy for the core-valence basis set aug-cc-pCV5Z. $\mathrm{CCSD(T)}$ method is used.

4.3 Excited state

The $a^3\Pi$ excited state potential energy curves for increasing basis set cardinal numbers are reported in Fig. 4.6. The global minima of this interaction lies at $r \approx 3.1$ bohr with a well depth of $30385\ \mathrm{cm}^{-1}$. The position of global minima only marginally decreases for the three basis sets reported in Fig. 4.6. The minima of the excited triplet state $a^3\Pi$ and the ground state is well separated by about $26731\ \mathrm{cm}^{-1}$ from the ground state, the accuracy of this separation is about 2% which was estimated in reference to the experimental observation of the electronic spectrum of aluminium monoflouride, the separation between $X^1\Sigma^+$and $a^3\Pi$ states is reported as $27241\ \mathrm{cm}^{-1}$ [155].

Fig. 4.7 presents the core electron correlation energy contribution to the interaction energy at CCSD(T)/aug-cc-pCV5Z level of theory. One immediate distinction to note is the difference between the Fig. 4.4 and Fig. 4.7. The core electron contribution gets negative only near the repulsive wall at r less than around 2.8 bohr.

4.3.1 Dipole moment and polarizability

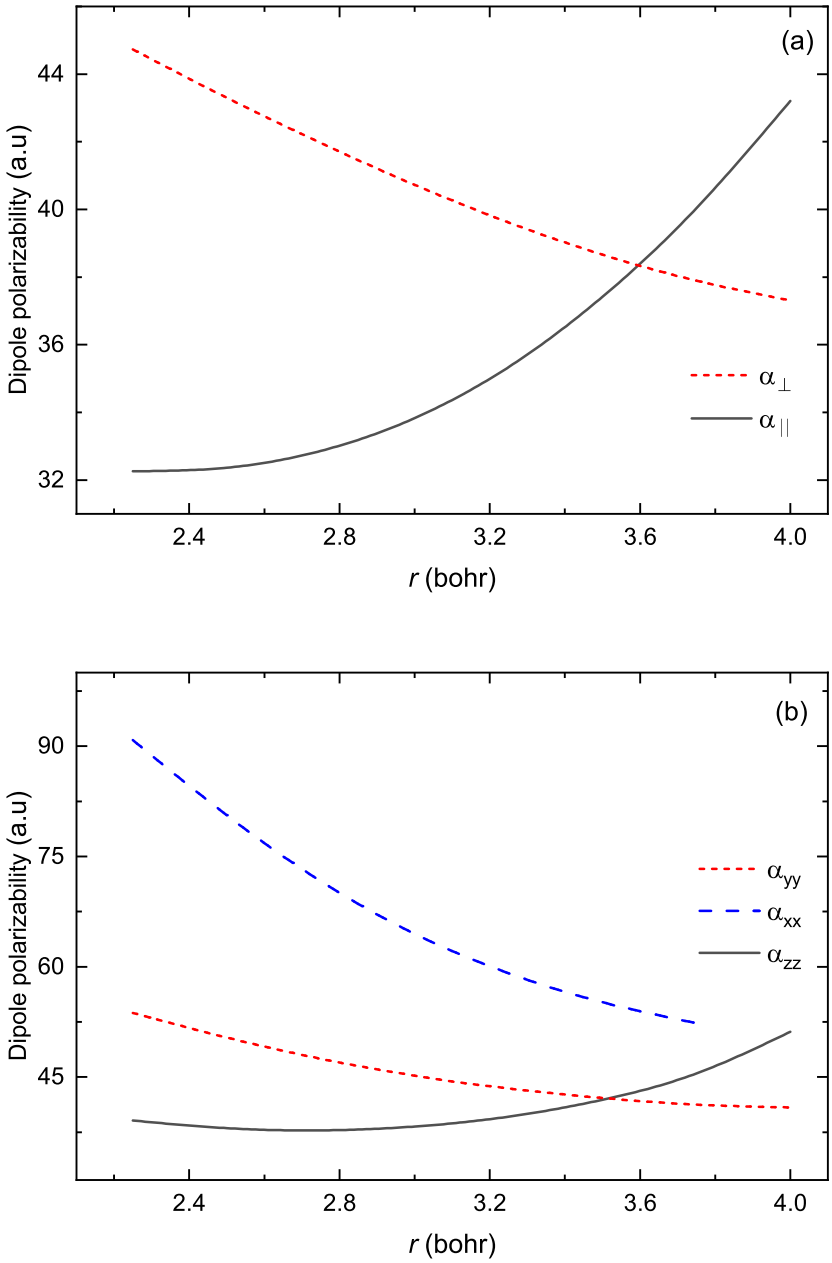

Figure 4.8: The dipole polarizability of the AlF molecule with respect to change in the bond length of AIF. Panel (a) shows results for AIF in ground state $X^1\Sigma^+$and panel (b) for AlF in excited state $a^3\Pi$. The level of theory used is $\mathrm{CCSD(T)}$ /aug-cc-pwCV5Z.

Fig. 4.8 shows the dipole polarizability components of AlF molecule with respect to the bond length. The calculations were carried out using the finite field method. We see that in Fig.

4.8, (a), for the azimuthally symmetric $X^1\Sigma^+$state, we have the parallel and the perpendicular components as the α_{xx} and α_{yy} components are equal.

In Fig. 4.8 (b), all the three polarizability components are completely different. At $r_{AlF} = 3.5$ bohr, there is a crossing between α_{yy} and α_{zz}. The α_{xx} component also seems to cross the lines of the other components at some later point.

Fig. 4.9 presents the dipole moment of the AlF molecule in $X^1\Sigma^+$and $a^3\Pi$ state for varying bond lengths. With increasing bond length, the dipole moment of AlF increases. When the molecule approaches dissociation into neutral atoms, the dipole moment should approach zero but we are unable to observe that here as the bond lengths we reported in Fig. 4.9 stay within the dissociation limit.

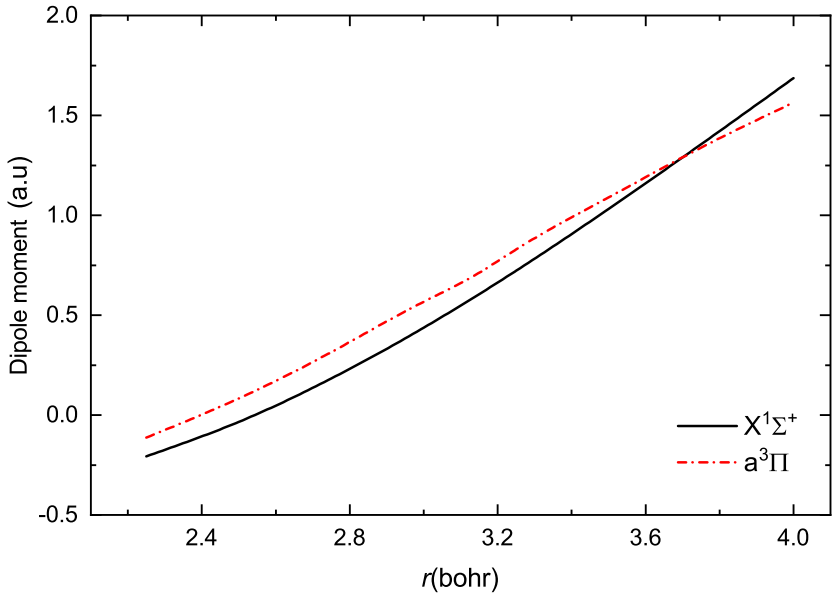

Figure 4.9: The dipole moment of the AIF molecule at different bond lengths for $X^1\Sigma^+$and $a^3\Pi$ states.

Table 4.2: Theoretical and experimental dipole moment values of AlF molecule at r_e. The dipole moment is in Debye. The level of theory used is CCSD(T)/aug-cc-pwCV5Z.

State	Theoretical	Experimental
$X^1\Sigma^+$	1.50 D	1.53 D [207]
$a^3\Pi$	1.45 D	1.78 D [146]

Tab. 4.2 reports the theoretical and experimental dipole moment values at equilibrium bond length. From the numbers, the theoretical dipole moment of the ground state is accurate upto one significant digit while the dipole moment for the excited state is less accurate than that of the ground state.

4.3.2 Conclusion

We have reported the ground and excited state potential energy curves of AlF molecule. The convergence of interaction energy to the basis set cardinal number and for different levels of theory for AlF molecules are further compared to that of AlF-He and AlF-AlF interactions. The dipole moment and dipole polarizability trend with respect to bond length shows how the vibrational motion of the molecule at cold temperatures influence the interaction with static electric fields. Our report on the potential energy of the molecule using different ab initio methods show the convergence trend for a deeply bound molecule as AlF. The depth of the $X^1\Sigma^+$state we report, $57152.2\ \mathrm{cm}^{-1}$, is 2.6% higher than the spectroscopic data of the AlF dissociation energy is $55652.2\ \mathrm{cm}^{-1}$ [145]. The separation between $X^1\Sigma^+$and $a^3\Pi$ states is experimentally reported as $27241\ \mathrm{cm}^{-1}$ [154] while the separation we had calculated, $26731\ \mathrm{cm}^{-1}$, is 2% lower. This shows the accuracy of our ab initio calculations and demonstrates that the theoretical values are both qualitatively and quantitatively reliable.

5 AlF-He

It is important to study the interaction between AlF and He as buffer gas cooling of AlF is a crucial first step for ultracold AlF production. Helium is most commonly used as a buffer gas owing to its i) chemically inert nature, ii) weak interactions with other molecules, iii) appreciable vapour pressure at temperatures above $200\mathrm{mK}$. Many molecules have been successfully buffer gas cooled to temperatures below 10 K [33].

In this chapter, I will discuss the relevant methodology used and the results regarding the interaction between aluminium monofluoride molecule and helium atom. I also discuss the convergence trend of interaction energy with respect to basis set cardinal number and different levels of theory, contribution of core electron correlation and relativistic effects. The computational run time for different basis sets are reported to understand the computational feasibility of ab initio calculations. The final section of this chapter consists of a report and discussion on the scattering between AlF molecule and He. This chapter is based on the published article **??**.

5.1 Methods

5.1.1 Ab initio electronic structure theory

The $X^1\Sigma^+, a^3\Pi, A^1\Pi$ states of AlF upon interaction with He correspond to the following states of the interacting complex $X^1A', a^3A'', b^3A', A^1A', B^1A''$ under the C_s point group (Tab. 5.1.1). The AlF molecule is considered as a rigid rotor with a fixed bond length r_{AlF}. The Jacobi coordinates R and θ are used to describe the orientation of the molecule and the atom. R is the distance between the helium atom and the centre of mass (c.m.) of the molecule; θ is the angle between the molecular axis and vector from c.m. to He ($\theta = 0^\circ$ corresponds to the linear He-AlF and $\theta = 180^\circ$ to the linear AlF-He). The coordinates are presented in Fig. 5.2.1. We used the vibrationally averaged value of bond length r_{AlF} for the corresponding electronic states [213, 214]. The interaction potential, V_{int} depends on both R, θ. We obtain V_{int} by using the

Table 5.1: Correlation between the electronic states of AlF molecule and AlF+He.

AlF	AlF + He
$X^1\Sigma^+$	X^1A'
$a^3\Pi$	b^3A'
	a^3A''
$A^1\Pi$	A^1A'
	B^1A''

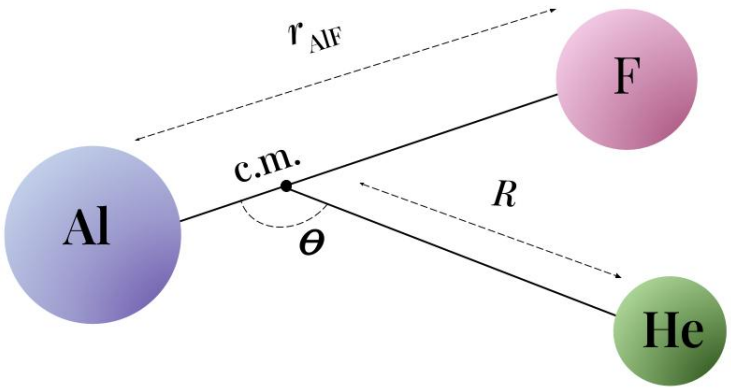

Figure 5.1: Jacobi coordinates for AlF+He system.

supermolecular method,

$$V_{\text{int}}(R,\theta) = E_{\text{AlF+He}}(R,\theta) - E_{\text{AlF}}(R,\theta) - E_{\text{He}}(R,\theta) \tag{5.1}$$

where $E_{\text{AlF+He}}$ is the total energy of the complex, E_{AlF} and E_{He} are the energies of the monomers. The basis set superposition error is corrected using the counterpoise correction [174] where the monomer energies are also calculated in the same basis set as that of the whole complex.

The explicitly correlated coupled cluster method [215] restricted to a single, double, and non-iterative triple excitations (CCSD(T)-F12b) [216], is used to calculate the potential energy surfaces for the states X^1A', a^3A'' and b^3A' of the AlF + He complex.

During $\mathrm{CCSD(T)-F12\,b}$ computations, we use aug-cc-pV6Z [217] as orbital basis set, augcc-pV6Z-RIFIT as density fitting and resolution of the identity basis, and aug-cc-pV5Z-JKFIT as density fitting basis for exchange and Fock operators. We obtained aug-cc-pV5Z-JKFIT by augmenting cc-pV5Z-JKFIT [218]. The cc-pV5Z-JKFIT for He based on the unpublished work [219]. The aug-cc-pV6Z-RIFIT based on unpublised work avaliable in the Basis Set Exchange repository [220, 221, 222].

We improve the description of electronic correlation of X^1A', a^3A'', b^3A' states by including full triple correction:

$$\delta V_{int}^{\text{CCSDT}} = V_{int}^{\text{CCSDT}} - V_{int}^{\text{CCSD(T)}}, \tag{5.2}$$

where V_{int} is the interaction energy calculated using the respective methods (presented as superscript). $V_{\text{int}}^{\text{CCSDT}}$ and $V_{\text{int}}^{\text{CCSD(T)}}$ were obtained with the aug-cc-pVTZ basis set [223, 224, 225] using the MRCC [**kallay**, 226, 227, 228, 229] code.

We describe A^1A' and B^1A'' states of the complex with the internally contracted multiconfiguration reference configuration interaction, MRCI, method with Davidson correction [230, 231, 232] and the aug-cc-[**empty citation**]pV5Z basis set [225, 223, 224]. We obtain appropriate orbitals by multistate MCSCF calculations [233]. The active space is composed of 5 orbitals in the A' symmetry, 1 orbital in A" symmetry, and 8 electrons.

All electronic structure calculations are performed with the Molpro package of ab initio programmes [234, 235].

The potential energy surfaces $V_{\text{int}}(R,\theta)$ are anisotropic and can be expanded in a basis of Legendre polynomials, $P_\lambda(\theta)$, as

$$V_{\text{int}}(R,\theta) = \sum_{\lambda=0}^{\lambda_{\max}} V_\lambda(R) P_\lambda(\cos\theta), \tag{5.3}$$

where $V_\lambda(R)$ are the expansion coefficients dependent on R. Potential energy surfaces $V_{\text{int}}(R,\theta)$ were calculated on a two-dimensional grid of 50 points in R between 5 and 35Bohr and 15 points in angle θ between 0° and 180° chosen to be the roots of the Legendre polynomial of order 15 .

At long range, the atom+molecule potential is dominated by attractive van der Waals interactions of the form $V(R) = -C_6/R^6$. The isotropic C_6 coefficients is sum of dispersion and induction contributions. Dispersion is an intermonomer correlation effect and corresponds to the interaction of fluctuating instantaneous dipole moments. The isotropic dispersion coefficient calculated from the Casimir-Polder formula is [199]

$$C_{6,0}^{\text{dis}} = \frac{3}{\pi}\int_0^\infty \bar{\alpha}^{\text{AlF}}(i\omega)\alpha^{\text{He}}(i\omega)d\omega, \tag{5.4}$$

where $\bar{\alpha}^X$ is the mean dynamic dipole polarizability of X. We calculated $C_{6,0}^{\text{dis}}$ using the coupled cluster polarization propagator method [236, 237, 199, 238, 239] within Molpro [234, 235] and obtained $C_{6,0}^{\text{dis}} = 18.97E_h a_0^6$. The anisotropic $C_{6,2}^{\text{dis}}$ coefficient is associated with the $P_2(\cos\theta)$ term in the Legendre expansion [240] and is given by

$$C_{6,2}^{\text{dis}} = \frac{1}{\pi}\int_0^\infty \Delta\alpha^{\text{AlF}}(i\omega)\alpha^{\text{He}}(i\omega)d\omega, \tag{5.5}$$

where $\Delta\alpha^X$ is the anisotropy of the polarizability of molecule X defined as the difference between parallel and the perpendicular dynamic dipole polarizabilities of X, as follow: $\Delta\alpha^X = \alpha_\parallel^X - \alpha_\perp^X$.$C_{6,2}^{\text{dis}}$ estimated as $-0.13E_h a_0^6$.

The induction effect is due to the polarization of a monomer due to the static field of the other monomer, in this case, AlF. The induction energy is determined by the permanent multipole moments and static polarizabilities of the monomers. The induction contribution to the C_6 coefficient can be written as

$$C_{6,0}^{\text{ind}} = C_{6,2}^{\text{ind}} = \mu_{\text{AlF}}^2 \alpha^{\text{He}}(0), \tag{5.6}$$

where μ_{AlF} is the electric dipole moment of AlF. The static polarizability of $\text{He}, \alpha^{\text{He}}$, was obtained from [241]. The value of C_6^{ind} was found to be $0.48E_h a_0^6$.

For triplet excited states of AIF, we scale the dispersion coefficients C_6^{dis} from the ground state by the ratio of the corresponding static polarizabilities. Refer to Chapter 4 for discussions and results on polarizability of AlF. For the $a^3\Pi$ state, static polarizability was obtained through the finite field method at $\mathrm{CCSD(T)}$ level.

5.1.2 Collision theory

The essence of buffer gas cooling is the thermalisation of AlF molecules by colliding with He atoms. Thus, scattering calculations are necessary to understand the possible outcomes of cooling of AlF by He.

The total Hamiltonian of the atom+rigid-rotor system in the centre-of-mass frame under the Born-Oppenheimer approximation is

$$\hat{H} = -\frac{\hbar^2}{2\mu}\nabla_R^2 + \frac{\hbar^2 \hat{L}^2}{2\mu R^2} + V_{\text{int}}(R,\theta) + B_0 \hat{j}^2 \tag{5.7}$$

The first term is the component of the kinetic energy operator in the scattering coordinate R. The second term is the centrifugal component, where $\hat{L}$ is the rotational angular momentum of He and AlF around each other, with the quantum number L.$V_{\text{int}}(R,\theta)$ is the interaction potential of the colliding systems, as calculated in the previous section, and μ is the collisional reduced mass. The states of the free molecule are eigenfunctions of the rotational Hamiltonian, $\hat{H}_{\text{rot}} = B_0 \hat{j}^2$, with rotational quantum number j and energy $j(j+1)B_0$, where $B_0 = 0.55\ \mathrm{cm}^{-1}$ [242] is the rotational constant of AlF. We neglect the small differences in rotational constant for different electronic states.

The expansion coefficients $V_\lambda(R)$ of the interaction potentials are interpolated and extrapolated using a reciprocal power reproducing kernel Hilbert space method (RP-RKHS) [243]. This produces potentials with asymptotic forms as a sum of terms with different inverse powers depending on the parameters used. Terms with different values of λ in the expansion have different leading terms, and we have chosen parameters in the method to give the correct leading powers up to R^{-10}. For the long-range coefficients calculated in the previous section, we use the method from [244] to fix the extrapolation to these values.

We perform coupled-channel scattering calculations using the MOLSCAT package [200, 245]. The angular component of the wave function is expanded in the total angular momentum basis [246], limited by $j_{\max} = 12$. Coupled equations are propagated using the Manolopoulos diabatic modified log-derivative [205] and the Alexander-Manolopoulos Airy propagator [206]. The solutions are matched to asymptotic boundary conditions. S matrices extracted, and cross sections calculated using usual methods.

Bound states are calculated using the Bound package [245, 247]. This is closely related to MOLSCAT and uses similar coupled-channels methods, but matches to bound-state boundary conditions and solves for eigen energies.

Table 5.2: Equilibrium Jacobi coordinates R_e, θ_e and equilibrium well depths D_e of AlF+He complex in different electronic states. Values for global minima (gm) and local minima (lm) are reported.

state	minima	R_e(bohr)	θ_e (degree)	$D_e\left(\mathrm{cm}^{-1}\right)$	reference
X^1A'	gm	7.71	180	24.9	this work
		7.1	180	22	[144
		7.75	180	24.056	[150]
	lm	10.06	0	-8	this work
b^3A'	gm	7.17	141.4	27.5	this work
	lm	8.68	0	21	this work
	lm	7.59	180	27.2	this work
a^3A''	gm	6.00	85.4	54.1	this work
	lm	7.59	180	27.2	this work
A^1A'	gm	7.62	180	24.0	this work
	lm	9.05	0	22.1	this work
B^1A''	gm	7.62	180	24.0	this work
	lm	9.05	0	22.1	this work

5.2 Results

5.2.1 Potential energy surfaces

The depth of the potential well is in the range between 21 and 28 cm^{-1} except for a^3A'' (Tab. 5.2.1), only slightly deeper than that of a similar $\mathrm{YbF} + \mathrm{He}$ complex (21.88 cm^{-1} [248]) and somewhat on the low end of the scale of the typical interaction strength between He and neutral molecule [249]. The only exception is the lowest triplet state, a^3A'', for which we predict roughly two times deeper interaction potential, close to the high end of the scale of the typical interaction strength between He and neutral molecule [249]. Such a noticeable difference shows that the interaction strength between AlF and He can be controlled by electronic excitation.

Fig. 5.2 shows one-dimensional cross sections through the potential energy surface of the $X^1A', a^3A'', b^3A', A^1A', B^1A''$ states of $\mathrm{AlF} + \mathrm{He}$ in linear and perpendicular configurations. For the ground state of AIF, the linear configuration in which He is near fluorine is twice as deep as for the perpendicular and the other linear configuration. Additionally, the minima for linear $\mathrm{He} + \mathrm{AlF}$ orientation exhibit higher intermonomer separation than AlF+He. The electronic excitation allows helium to come closer to aluminum and reduces the differences in the depths of the well for two linear configurations. Once again, we see that we can control the shape of the potential by changing the electronic state of AlF.

The anisotropic nature of the interaction is also seen on Fig. 5.3 and Fig. 5.4, that show two dimensional contour plots of $V_{\mathrm{int}}(R, \theta)$ for the $X^1A', a^3A'', b^3A', A^1A'$, and B^1A'' states. All surfaces show strong orientation dependence. The global minima for the a^3A'' and b^3A' states are non-linear in contrast to the singlet states, that are linear. At global minima of the X^1A', b^3A', A^1A', and B^1A'' states, the He atom is near the fluorine, which is the electronegative side

of the molecule. A similar situation was reported for $\mathrm{YbF} + \mathrm{He}$ [248].

For the X^1A', b^3A', A^1A', and B^1A'' states, there is a local minimum in the linear configuration where He reaches the molecule from the side of Al. The depth of this minima is approximately $8\ \mathrm{cm}^{-1}, 21\ \mathrm{cm}^{-1}, 22.1\ \mathrm{cm}^{-1}$ and $22.1\ \mathrm{cm}^{-1}$ for X^1A', b^3A', A^1A' and B^1A'' states respectively. Only a^3A'' does not exhibit the minima for that orientation. The local minimum of X^1A' was not reported in the previous studies, [151, 145] because it appears only after including full triple corrections. This minimum is very shallow; the barrier joining global and local minima has energy only a fraction of cm^{-1} higher than local minima. For the a^3A'' and b^3A' states, we see a local minimum with a depth of $27.2\ \mathrm{cm}^{-1}$ in the linear configuration where He reaches the molecule from the side of fluorine, similar to the global minima of the ground states.

The accuracy of our electronic structure calculation may be affected by (a) an incomplete orbital basis set, (b) an inadequate description of the correlation energy, and (c) the neglect of relativistic effects. The correct description of the electron correlation is crucial for $\mathrm{AlF} + \mathrm{He}$, similar to other systems dominated by the van der Wals interaction. The convergence of interaction energy of X^1A' with the quality of the wavefunction is analysed in Fig. 5.5(a). The HartreeFock method, which is a mean-field method, produces a repulsive potential. The second-order perturbation theory, MP2, reproduces about 75% of the correlation energy. The depth of the potential predicted at the CCSD level is $19.4\ \mathrm{cm}^{-1}$. Further perturbative inclusion of triple excitation deepens the potential by $3.7\ \mathrm{cm}^{-1}$ while the full triple correction improves it further by
$0.62\ \mathrm{cm}^{-1}$. The perturbative treatment of the triple excitation is responsible for approximately 85% of the total triple contribution.

When calculating the entire potential energy surface, we neglect the excitations higher than triple in the coupled cluster expansion. We estimated that contribution as a difference between $\mathrm{CCSDT(Q)}$ and CCSDT potential, and it turned out to be relatively small as presented in Fig. 5.6. It altered the interaction energy by $0.5\ \mathrm{cm}^{-1}$ near the classical turning point and steeply decreased with the inter atomic distance to more than ten times lower value $\left(0.045\ \mathrm{cm}^{-1}\right)$ at the global minimum. The reported potential energy surface also neglects the core-electron and core-valence correlation. Including the core-electron and core-valence correlation changes the interaction energy by $0.02\ \mathrm{cm}^{-1}$, as we estimate at the $\mathrm{CCSD(T)}$ level of theory. The system under study is relatively light, so the relativistic effects are relatively small, as we see from the $\mathrm{CCSD(T)}$ /augcc-pV5Z calculations with Douglas-Kroll-Hess Hamiltonian included up to the third order. The correction is in the range of -0.1 to $-0.05\ \mathrm{cm}^{-1}$ (Fig. 5.6) around the global minimum and decreases with increasing distance.

Basis sets with increasing basis set cardinal numbers have been used to study convergence toward the complete basis limit. As shown in Fig. 5.5(b), the depth of the potential increases monotonically as the basis set size increases. The difference in depth of the potentials predicted by $\mathrm{CCSD(T)}$-F12 using aug-cc-pV5Z and aug-cc-pV6Z basis sets is $0.28\ \mathrm{cm}^{-1}$. For sextuple zeta basis sets, the difference between $\mathrm{CCSD(T)}$ and $\mathrm{CCSD(T)}$-F12 is about $0.5\ \mathrm{cm}^{-1}$. The complete basis set limit estimated using $\mathrm{CCSD(T)}$ is deeper by $0.3\ \mathrm{cm}^{-1}$ than the depth of the well estimated by $\mathrm{CCSD(T)}$-F12.

We test the accuracy of rigid rotor approximation by optimizing the structures of AlF and $\mathrm{AlF} + \mathrm{He}$ using $\mathrm{CCSD(T)}$/ aug-cc-pV5Z. The interaction with He decreases the equilibrium bond length of AlF by 0.008 bohr. This small relaxation of the bond length changes the interac-

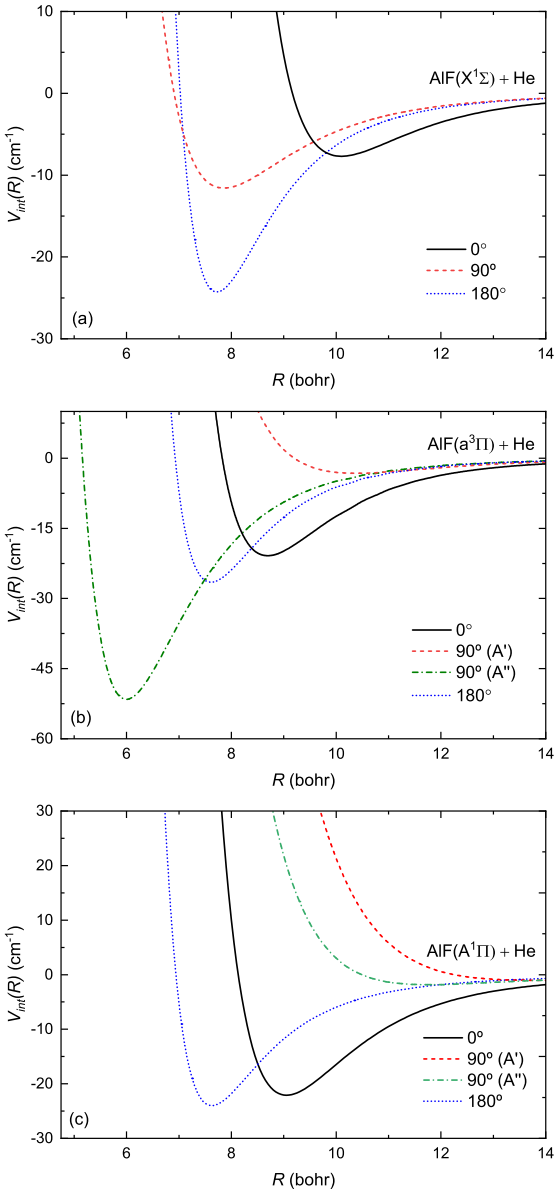

Figure 5.2: one-dimensional cuts through the potential energy surfaces for the states of AlF+He, (a) X^1A', (b) a^3A'' and b^3A', and (c) A^1A' and B^1A'' in linear and perpendicular orientations.

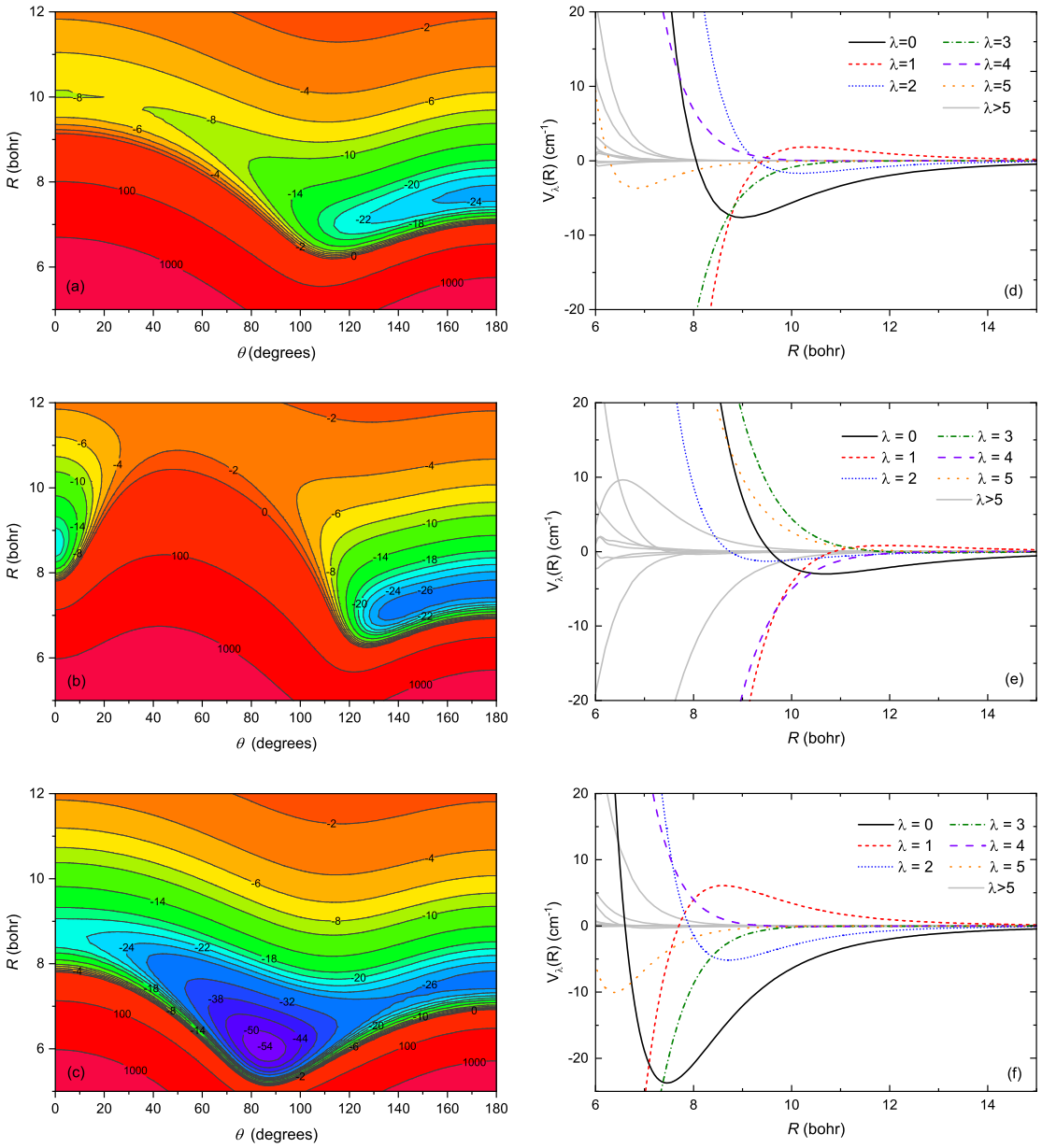

Figure 5.3: The two-dimensional potential energy surfaces for the (a) X^1A', (b) b^3A', (c) a^3A'' states of AlF + He. Panels (d), (e), and (f) show the first 15 Legendre components of the respective potential energy surfaces.

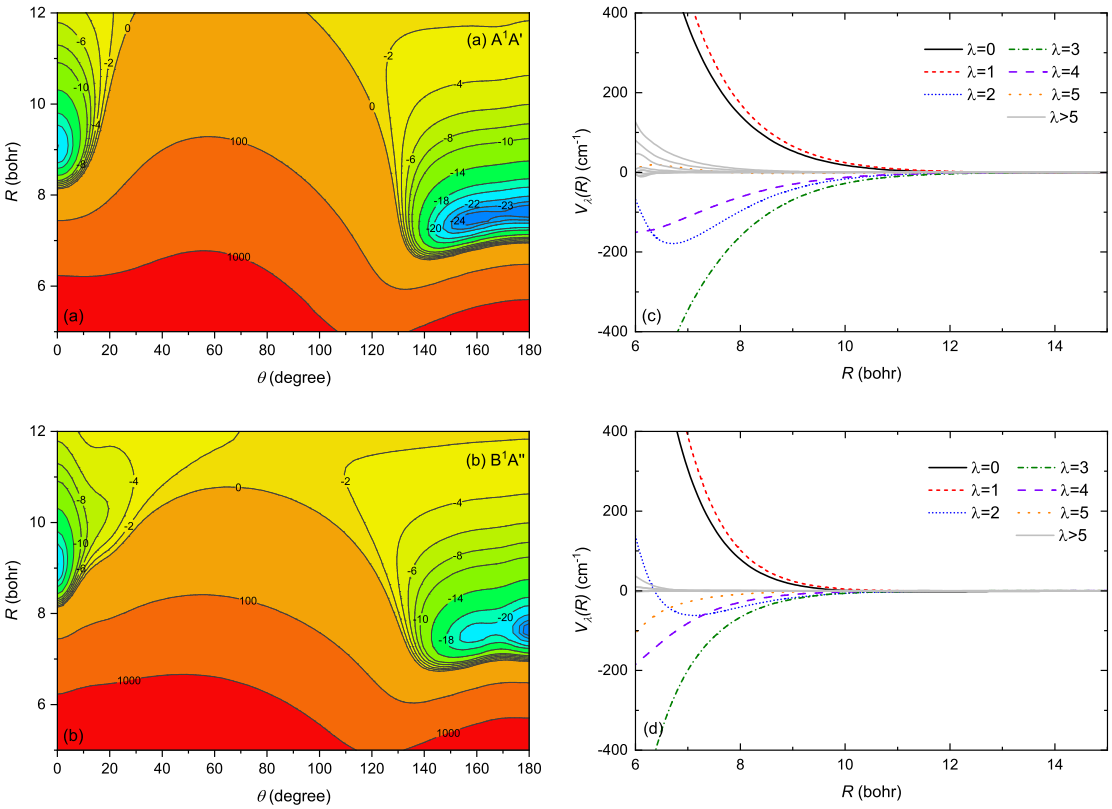

Figure 5.4: The two-dimensional cuts through the potential energy surfaces for the (a) A^1A' and (b) B^1A'' states of the AlF + He complex. Panels (c) and (d) show the first 15 Legendre components of the respective potential energy surfaces.

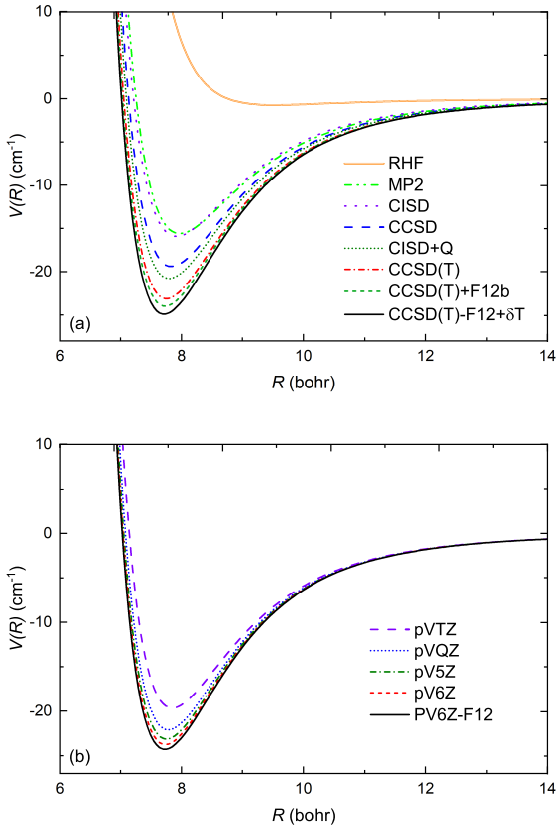

Figure 5.5: The convergence of the interaction energy of the X^1A' state at $\theta = 180°$ (a) for different ab initio methods with the aug-cc-pV5Z basis set and (b) for the aug-ccpVXZ basis set with increasing basis set cardinal number. CCSD(T) method is used.

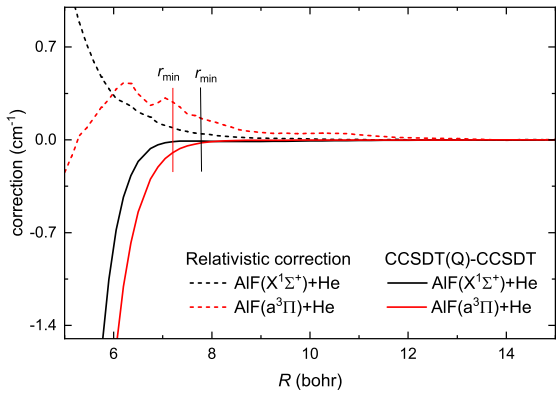

Figure 5.6: The effect of the including iterative quadruple excitation and the relativistic correction (DKH Hamiltonian of order=3) on the AlF+He interaction energy. r_{min} indicates the position of global minima in R coordinate. The red lines are for b^3A' state and the black line is for X^1A' state.

tion energies by a negligible $0.02\ \mathrm{cm}^{-1}$.

The accuracy of our calculations is predominantly limited by the basis set incompleteness in the description of the valence electron correlation. The overall accuracy of our potential at global minimum is $0.3\ \mathrm{cm}^{-1}$, which is 1.3% of the depth of the ground state potential. Our ground state interaction potential exhibits depth similar to that in Ref. [150] but it is deeper by 12% ($2.9\ \mathrm{cm}^{-1}$) than reported in Ref. [145]. This discrepancy isn't surprising, as the calculations reported in Ref. [145] do not reach the complete basis set limit. The older results reported in Ref. [151] use the mid-bounds functions, which improve the convergence of the interaction energy with the basis set size. The basis set incompleteness hampers the accuracy of our potential in b^3A' state by $1\ \mathrm{cm}^{-1}$, which is 3.9% of the depth of the b^3A' potential and 2% of the depth of the a^3A'' potential, the same for the A^1A'' and B^1A' state (MRCI/aug-cc-pV5Z) is $0.4\ \mathrm{cm}^{-1}$ which is 1.6% of the depth of the potential. We expect that the MRCI computations are affected mainly by the lack of higher excitations in the configuration interactions expansion and the size consistency of the method. We do not have any reliable estimation of that contributions. Still, we may expect that it can be even of the order of 20%, similar to the difference between the CCSD and CCSDT interaction energies at the ground state.

The further increase in the size of the basis set will lead to improved accuracy of the predicted potential. However, the increase in the size of the basis set will also lead to a dramatic increase in computational time.

An ab initio report

The average run time for $\mathrm{CCSD(T)}$ calculations with different basis sets and extensions is recorded for X^1A' in Tab. 5.2.1 and for b^3A' in Tab. 5.2.1. The highest difference in run time is seen between valence and core-valence electron correlation which is about 6 times for cardinal number $X = 5$. For other extensions from $\mathrm{CCSD(T)}$ such as including relativistic correction, $\mathrm{CCSD(T)-F12}$ method and use of mid bonds increase the run time at most twice as much as $\mathrm{CCSD(T)}$/ aug-cc-pV5Z.

Table 5.3: The equilibrium position, R_{eq} and the well depth, D_{eq} calculated using CCSD(T) method using different basis sets and augmentations, average run time per point (using MOLPRO). The calculation was performed for X^1A' state.

AlF + He				
Basis sets	R_{eq}	D_{eq}	(run time) C_{2v}	(run time) C_s
aug-cc-pVTZ	7.84121	19.569	0.25 mins	
aug-cc-pVQZ	7.77454	22.004	60.4 s	1.2 mins
aug-cc-pV5Z	7.74391	23.025	6 min	7.10mins
aug-cc-pV5Z+rel	7.74393	23.033	5.3mins	
aug-cc-pV6Z	7.72809	23.656	45 mins	
aug-cc-pV5Z+MB	7.72073	24.208	10.2 mins	13.77 mins
aug-cc-pVQZ+MB	7.72665	24.116	3.2mins	
aug-cc-pV6Z+MB	7.71781	24.262	78 mins	
aug-cc-pV5Z+F12c	7.72312	23.832	13 mins	
aug-cc-pV5Z+F12b	7.72273	23.833	13 mins	
aug-cc-pCV5Z	7.74319	23.033	54 mins	
FAl+He				
aug-cc-pVTZ	10.2567	6.527	13.4 s	
aug-cc-pVQZ	10.1794	7.016	62 s	1.09mins
aug-cc-pV5Z	10.1273	7.376	7.8 mins	7.5 mins
aug-cc-pV5Z+rel	10.1198	7.391	5.9mins	
aug-cc-pV6Z	10.1089	7.576	50 mins	
aug-cc-pV5Z+MB	10.0981	7.706	11mins	14.3mins
aug-cc-pVQZ+MB	10.1064	7.663	2.42 mins	
aug-cc-pV6Z+MB	10.0932	7.750	2.28hrs	
aug-cc-pV5Z+F12c	10.1088	7.542	14.4 mins	
aug-cc-pV5Z+F12b	10.1065	7.552	14.4 mins	
aug-cc-pCV5Z	10.1271	7.375	43 mins	
$\perp$ geometry				
aug-cc-pVTZ	8.0539	9.671		11sec
aug-cc-pVQZ	7.94657	10.583		1 min
aug-cc-pV5Z	7.90203	11.062		13.5 mins
aug-cc-pV5Z+rel	7.89326	11.114		18.6 mins
aug-cc-pV6Z	7.88718	11.359		1.34hrs
aug-cc-pVQZ+MB	7.87029	11.523		3.34mins
aug-cc-pV5Z+MB	7.86394	11.583		35 mins
aug-cc-pV6Z+MB	7.86107	11.626		2.3hrs
aug-cc-pV5Z+F12b	7.87411	11.385		44 mins
aug-cc-pV5Z+F12c	7.87702	11.350		44 mins

Table 5.4: The equilibrium position, R_{eq} and the well depth, D_{eq} calculated using CCSD(T) method using different basis sets and augmentations, average run time per point (using MOLPRO). The calculation was performed for b^3A' state.

b^3A'			
AlF + He			
Basis sets	R_{eq}	D_{eq}	average run time (C_s group)
aug-cc-pVTZ	7.72182	21.795	10 s
aug-cc-pVQZ	7.6655	24.243	1.2 mins
aug-cc-pV5Z	7.6357	25.315	7.6 mins
aug-cc-pV5Z+rel	7.63398	25.347	17 mins
aug-cc-pV6Z	7.6211	25.968	35.5mins
aug-cc-pV5Z+MB	7.6144	26.537	18 mins
aug-cc-pVQZ+MB	7.6192	26.480	2.7 mins
aug-cc-pV6Z+MB	7.6104	26.587	3.2hrs
aug-cc-pV5Z+F12b	7.61577	26.213	14.6 mins
aug-cc-pV5Z+F12a	7.61206	26.336	14.6 mins
FAl + He			
aug-cc-pVTZ	8.8832	16.768	10.5 s
aug-cc-pVQZ	8.7617	18.737	1 min
aug-cc-pV5Z	8.7186	19.921	10 mins
aug-cc-pV5Z+rel	8.70737	20.086	11.6mins
aug-cc-pV6Z	8.6983	20.498	58 mins
aug-cc-pV5Z+MB	8.6923	20.887	22 mins
aug-cc-pVQZ+MB	8.7027	20.675	2.7 mins
aug-cc-pV6Z+MB	8.6888	20.998	2.72hrs
aug-cc-pV5Z+F12b	8.69382	20.697	14 mins
aug-cc-pV5Z+F12a	8.68812	20.831	14 mins
$\perp$ geometry			
aug-cc-pVTZ	10.6693	2.531	28sec
aug-cc-pVQZ	10.5418	2.755	2.6 mins
aug-cc-pV5Z	10.4489	2.953	23 mins
aug-cc-pV6Z	10.3861	3.117	1.4hrs
aug-cc-pVQZ+MB	10.3618	3.266	7.7 mins
aug-cc-pV5Z+MB	10.3496	3.289	45 mins
aug-cc-pV5Z+rel	10.4504	2.949	47 mins
aug-cc-pV5Z+F12a	10.381	3.114	40 mins
aug-cc-pV5Z+F12b	10.3867	3.103	40 mins

Fig. 5.7 presents a plot of average run time against the basis set cardinal number. We can notice that for a lower C_s symmetry, the average computational run time is almost twice as that for the C_{2v} symmetry. The Tab. 5.2.1 reports the equilibrium position, R_{eq} and the well depth, D_{eq} for the three configurations $\theta = 180°, 0°, 90°$. A general observation that can be made

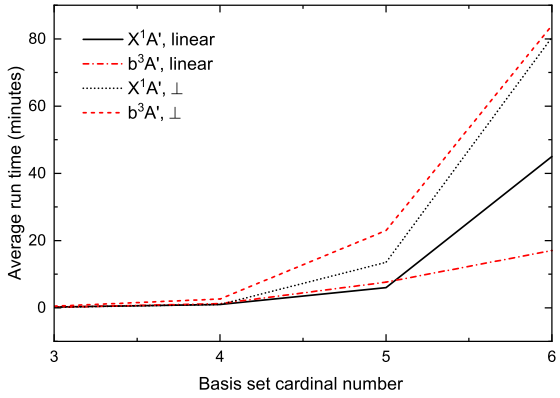

Figure 5.7: The average run time of CCSD(T) calculations plotted against the basis set cardinal number for aug-cc-pVXZ basis. For the linear geometry AlF-He, the symmetry enforced is C_{2v}, for $\perp$ geometry, C_s symmetry is enforced.

is that computational time is longer when the lower C_s symmetry is implemented. For both symmetries the computational time grows rapidly with the basis set cardinal number.

5.2.1 Collision dynamics

When AlF collides with He, there are two possible outcomes: elastic collision, where there is no change in AlF's internal state, and inelastic collision, where there is a change in AlF's rotational state. Elastic collisions determine the translational thermalization of AlF, whereas inelastic collisions determine rotational thermalisation. Fig. 5.8 shows the elastic and inelastic cross sections for the AlF + He collision for the X^1A', a^3A'' and b^3A' states. To better understand these outcomes, we can examine the cross sections of these events.

Let us focus on the temperatures between 100mK to 10 K, which are the most interesting from the buffer-cell cooling perspective. A significant value of elastic cross-section is necessary to provide effective translational thermalisation. In systems where inelastic cross-sections are about one to two orders of magnitude lower than elastic ones [250, 33] both translational and rotational degrees of freedom can be thermalized. The thermally-averaged elastic cross sections for the AlF+He collision (Fig. 5.8 lie in the range between 0.2×10^3 and $2\times10^3 \mathring{A}^2$, regardless of the quantum state of AlF. These calculated values are larger than the $0.1\times10^3 \mathring{A}^2$ experimentally estimated for CaH [30], but comparable to the values calculated for that system [251]. On average, buffer gas cooling can achieve a temperature range of a few hundred mK. For the X^1A' state of AlF + He, the ratio of elastic to inelastic collision is around 7 for $\sigma_{j=1}/\sigma_{j=1\to0}$ at 1 K gradually decreasing to 0.9 at 0.2 K, around 10 for $\sigma_{j=2}/\sigma_{j=2\to0}$ at 1 K increasing to 15 near 0.5 K to 0.9 at 10mK, around 3 for $\sigma_{j=2}/\sigma_{j=2\to1}$ at 1 K to 0.9 at 90mK. With higher elastic collision cross sections, translational thermalisation looks more prospective near 1 K. The trend is similar for other states of the AlF. The values of the ratio of elastic to inelastic collisions at 1 K are reported in Table 5.2.1.

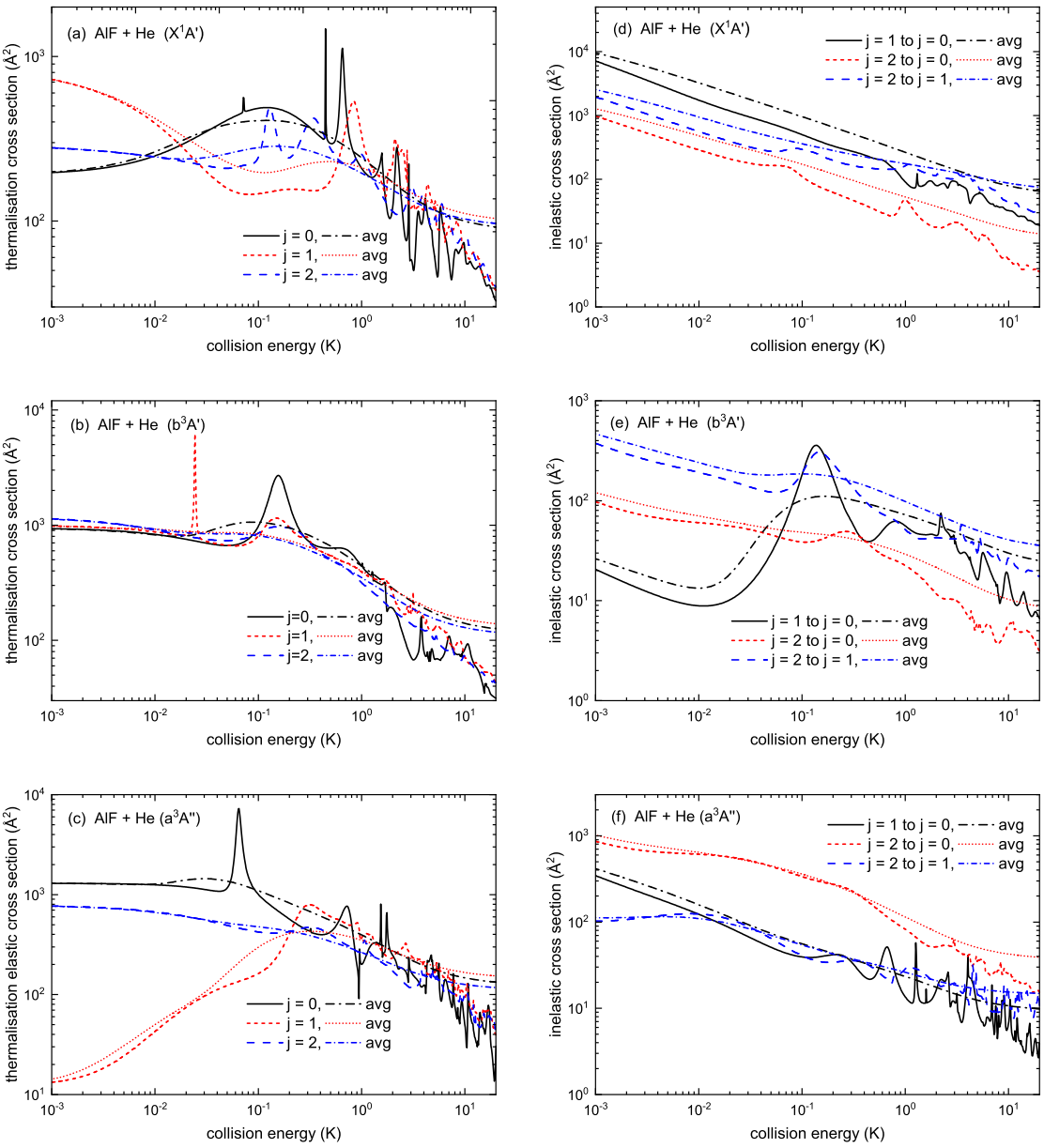

Figure 5.8: Elastic cross section vs collision energy for AlF +He collision complex in the (a) X^1A', (b) b^3A', (c) a^3A'' states. The inelastic cross section for the AlF+He collision are in the (d) X^1A', (e) b^3A', (f) a^3A'' states. The cross sections of the scattering channels for the rotational states $j = 0, 1, 2$ of AlF are shown. The corresponding curves in the same colour are the thermally averaged cross sections.

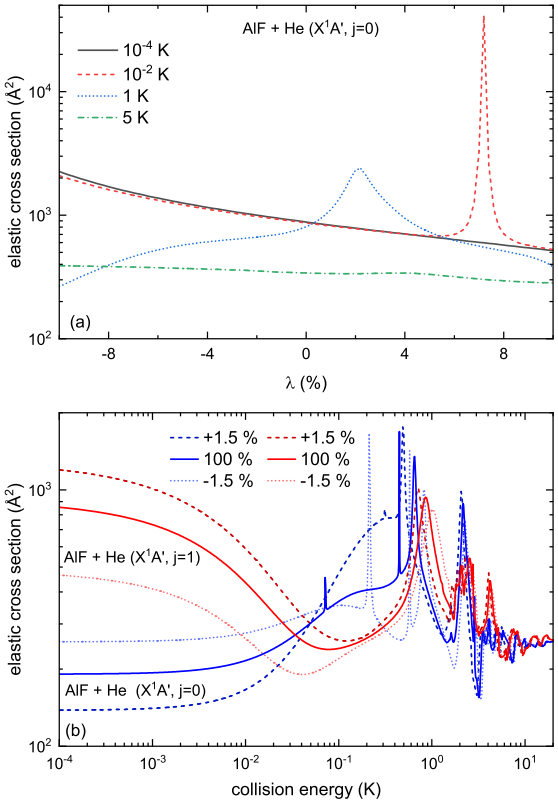

Figure 5.9: (a) The sensitivity of the elastic scattering cross section to the scaling of the potential for the X^1A' state of the $\mathrm{AlF}+\mathrm{He}$ for the collision energies 5 K, 1 K, 0.01 K, 0.0001 K. (b) Elastic scattering cross-sections in function for the potential scaled by $\pm 1.5\%$.

Table 5.5: Ratio of elastic to inelastic collision cross sections at 1 K for the $\mathrm{AlF}+\mathrm{He}$ collisions.

State	$\sigma_{j=1}/\sigma_{j=1\to 0}$	$\sigma_{j=2}/\sigma_{j=2\to 0}$	$\sigma_{j=2}/\sigma_{j=2\to 1}$
X^1A'	7.6	10.8	3.1
a^3A''	18.6	40.3	17.6
b^3A'	36.6	8.9	25.5

Let us focus now on temperatures below $100\mathrm{mK}$, which are difficult to obtain by pure buffer cell cooling; however, we see higher sensitivity of the cross-sections on the rotational state. The elastic cross-sections are relatively constant at these temperatures, as the shape resonances gradually disappear with a decreasing temperature. The inelastic cross section is most significant for the state X^1A', resulting in fast rotational relaxation from $j = 1$ to $j = 0$ of AlF. For the X^1A' state of AlF+He, $\sigma_{j=1\to 0}$ is more than an order of magnitude higher than $\sigma_{j=1}$. This means that the molecules should be cooled into the rotational ground state efficiently. Lower values of inelastic cross-sections for triplet states can be related to lower anisotropy of the potentials, visible as a smaller difference in the shape of the potential energy curves for $\theta = 0°$ and $\theta = 180°$

Table 5.6: Bound states for $X^1\ A'$ state of AlF + He. Energy in cm^{-1}.J is the total angular momentum, p is the parity of the state.

J^p					
0^+	-7.59	-2.44	-0.63		
1^+	-4.77	-0.03			
1^-	-7.22	-4.84	-2.01	-0.81	
2^+	-6.50	-4.13	-1.52	-1.16	-0.43
2^-	-3.96	-1.45			
3^+	-2.75	-0.41			
3^-	-5.43	-3.07	-0.71		
4^+	-4.01	-1.68			
4^-	-1.16				
5^-	-2.27				
6^+	-0.21				

in Fig. 5.8 (b) and (c). Still, the inelastic and elastic cross-sections are usually in comparable range. Panel (c) of Fig. 5.8 shows that for the a^3A'' state, the elastic cross section for $j = 1$ is negligibly low in the low-energy limit; this is due to the scattering length being accidentally close to zero. This will inhibit translational thermalisation in this state, but the inelastic cross section is much larger, so the molecules will rapidly reach a different state where cooling could continue.

The bound states of the AlF+He complex in the X^1A' state are reported in Table 5.6. The lowest bound state supported by this potential is at $-7.59\ cm^{-1}$. There are 26 bound states for the ground state. For the a^3A'' state with a well depth of $54\ cm^{-1}$, there are 124 bound states, which are tabulated in the Appendix A.

We study the sensitivity of our scattering results to interaction energy by scaling potential to ± 10 percent and observe changes in the elastic cross-sections. Fig. 5.9 (a) shows how the cross section varies with a scaling of the potential for four energies. Here, λ scales the potential energy as $V \rightarrow (1 + \lambda) \times V$. We observe a peak in the 1 K line (Fig. 5.9 (a)), which can be attributed to the sensitivity of the shape resonances visible around 1 K in Fig. 5.8 (a). The uncertainty of the potential energy surface is about 2%, so the scattering results are not very far from the truth for all four energies. In Fig. 5.8 (b) we show the shift in elastic cross sections for a $\pm 1.5\%$ scaling for two rotational states of the AlF. For the $j = 0$ rotational state of AlF, the first few shape resonances are more sensitive to the scaling of potential, but their relative sensitivity decreases for higher energies. For the $j = 1$ rotational state of AlF, the curves are shifted while preserving the general shape. The scattering cross sections generally lie in the same range as predicted recently in Ref. [145], with a shift in the position of shape resonances. Although our ab initio calculations are more accurate, the scattering results from Ref. [145] are similar, which suggests that the details of the potential energy surface have a moderate effect on the scattering outcomes for this system.

5.2.2 Conclusion

We have constructed accurate potential energy surfaces using the explicitly correlated coupled-cluster method for the $\mathrm{AlF} + \mathrm{He}$ interaction. We understand that interaction between He and AlF is anisotropic and weak. For all states we have found global and local minimum. For most of the states, the global minima is linear and appear when He approaches F. The only exception from this rule is a^3A'' state, however it exhibit deep local minima for $\mathrm{AlF} + \mathrm{He}$ orientation. $\mathrm{AlF} + \mathrm{He}$ is a relatively light system uninfluenced by relativistic effects. Coupled channel scattering theory was then used to calculate the scattering cross sections of the AlF+He collision outcomes. The uncertainty of the potential energy surface were estimated, and the sensitivity of the scattering results to the scaling of the potential was studied to give us a better idea of the predictability of the results. It helps determine the optimal conditions for buffer gas cooling. The high ratio of elastic to inelastic collisions suggests that buffer gas cooling of AlF molecule can be efficient. We have demonstrated that the shape and depth of the $\mathrm{AlF} + \mathrm{He}$ interaction potential can be controlled by changing the electronic state of AlF.

6 AlF-AlF

Interaction between aluminium flouride molecules determine the efficiency of evaporative cooling. Molecular collisions are an integral part of ultracold studies and it is essential to study them to gain a complete understanding of the ultracold interactions. AlF is a polar molecule with an electric dipole moment of $1.53\mathrm{D}$, hence the nature of interaction is dipolar. The interaction energy between two dipoles with dipole moments along the unit vectors $\vec{e}_1$ and $\vec{e}_2$ is given by the expression,

$$U_{dd}(\vec{r}) = \frac{d^2}{4\pi\epsilon_0}\frac{(\vec{e}_1\cdot\vec{e}_2)\,r^2 - 3\,(\vec{e}_1\cdot\vec{r})\,(\vec{e}_2\cdot\vec{r})}{r^5} \tag{6.1}$$

where d is the permanent electric dipole moment, ϵ_0 is the vacuum permittivity. As the dipoledipole interaction decays as $\sim \frac{1}{r^3}$, it has a long range character compared to the van der Waals type interaction dominated by dispersion $\left(\sim \frac{1}{r^6}\right)$.

For dipoles pointing in the same direction, the interaction becomes

$$U_{dd}(\vec{r}) = \frac{d^2}{4\pi\epsilon_0}\frac{1-3\cos^2\theta}{r^3} \tag{6.2}$$

where θ is the angle between the dipole and the vector joining the particles. Polar molecules like AlF possess permanent electric dipole moment which means in the presence of electric field, they have both highand low-field seeking states. Hence, the interparticle interactions can be controlled and tuned by external fields or by optical traps [252, 107, 253, 254]. Recent progress in experiments with ultracold polar molecules has created more interest in low temperature dipolar interactions [252, 253, 254, 255, 256, 77, 40].

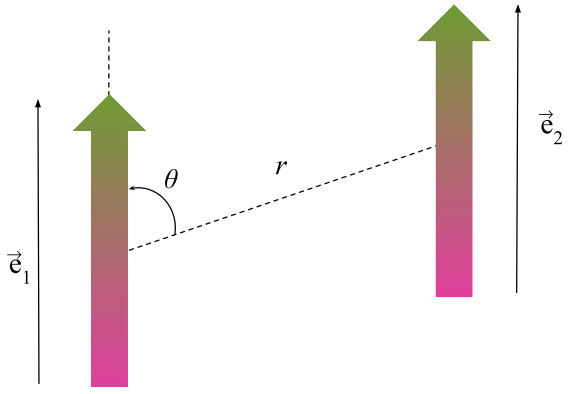

Figure 6.1: Dipolar interaction.

Table 6.1: Jacobi angles for selected spatial configurations of the AlF-AlF system. The definition of angles are on Fig. 6.2.

Name	θ_1	θ_2	Φ
AlF-AlF	0°	180°	0°
AlF-FAl	0°	0°	0°
FAl-AlF	180°	180°	0°
⊥;FAl-AlF	180°	90°	0°
⊥;AlF-AlF	0°	90°	0°
parallel dipoles	90°	90°	0°
antiparallel dipoles	90°	90°	180°

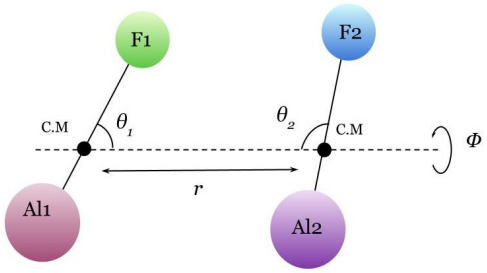

Figure 6.2: The Jacobi coordinates used to describe the AlF-AlF orientation is shown.

In this chapter, we aim to study the interaction between AlF molecules, report an accurate ground state potential energy surface for AlF-AlF interaction and potential energy curves for the excited states of the complex. The aluminium monofluoride molecules are treated as rigid rotors. There are four geometric parameters $(\theta_1, \theta_2, \phi, r)$ to describe the orientation of the two interacting monomers. These parameters are visualized through Fig. 6.2. The seven distinct configurations of the AlF-AlF complex for which the interaction energies were calculated are reported in Tab. 6.

The list of explored electronic states of AlF-AlF complex is presented in Tab. 6.2 along with the corresponding asymptotic monomer states and the level of theory with which the interaction energies have been evaluated. As we encountered convergence issues for the excited states, different levels of theory were used for different states.

6.1 Methods

The interaction potential V_{int} depends on $R, \theta_1, \theta_2, \phi$. Using the supermolecular method,

$$V_{\text{int}}\ (R, \theta_1, \theta_2, \phi) = E_{AlF+AlF}\,(R, \theta_1, \theta_2, \phi) - E_{AlF}\,(R, \theta_1, \theta_2, \phi) - E_{AlF}\,(R, \theta_1, \theta_2, \phi)\,, \tag{6.3}$$

Table 6.2: Ab initio methods used to calculate the interaction energy of the AlF-AlF system in different spin states for planar configurations.

Molecular states	Asymptotic states	Methods
X^1A'	$X^1\Sigma^+ + X^1\Sigma^+$	CCSD(T)
a^3A''	$X^1\Sigma^+ + a^3\Pi$	MRCI
b^3A''	$a^3\Pi + X^1\Sigma^+$	MRCI
c^3A'	$X^1\Sigma^+ + a^3\Pi$	MRCI
d^33'	$a^3\Pi + X^1\Sigma^+$	MRCI
A^1A''	$X^1\Sigma^+ + A^1\Pi$	EOM-CCSD
e^3A''	$a^3\Pi + a^3\Pi$	MRCI
f^3A'	$a^3\Pi + a^3\Pi$	MRCI
B^1A'	$X^1\Sigma^+ + A^1\Pi$	EOM-CCSD
g^3A''	$a^3\Pi + a^3\Pi$	MRCI
C^1A'	$A^1\Pi + X^1\Sigma^+$	EOM-CCSD
D^1A''	$A^1\Pi + X^1\Sigma^+$	EOM-CCSD
E^1A'	$X^1\Sigma^+ + B^1\Sigma^+$	EOM-CCSD
F^1A'	$B^1\Sigma^+ + X^1\Sigma^+$	EOM-CCSD
i^5A''	$a^3\Pi + a^3\Pi$	CCSD(T); MRCI
j^5A'	$a^3\Pi + a^3\Pi$	CCSD(T); MRCI
k^5A'	$a^3\Pi + a^3\Pi$	CCSD(T); MRCI

where $E_{AlF+AlF}$ is the total energy of the complex and E_{AlF} is the energy of the individual monomers.

The CCSD(T)-X2C/aug-cc-pVQZ-X2C and CCSD(T)-X2C/aug-cc-pVTZ-X2C method is used to calculate the ground state potential energy surface of the AlF-AlF interaction. Complete Basis Set (CBS) limit of the interaction energy was then extrapolated using the formula,

$$V(X) = V_{CBS} + a \cdot X^{-3} \tag{6.4}$$

where X is the basis set cardinal number, $V(X)$ is the interaction energy of AlF-AlF.

MRCI method is used to calculate the potential energy curves of a^3A'', b^3A'' and few other excited states. In the C_s symmetry, the active space used for these calculations is composed of four A' orbitals and two A'' orbitals. We used EOM-CCSD method to converge excited singlet states of the AlF-AlF dimer. One of the main challenges in ab initio calculations is to converge to the desired states. In the case of excited states of AlF-AlF dimer, the states a^3A'', c^3A', j^5A' and i^5A'' are the lowest states in the given spin multiplicity and symmetry. But CCSD(T) method, being a single reference method, did not always converge to these states. Our results also demonstrate the various logjams that one encounters during accurate electronic structure calculations.

X^1A' is the ground state of the AlF-AlF complex. We have calculated the potential energy curves for 14 excited states. Tab. 6.2 lists the states that we report on. Alphabetical convention is used to name the states where X denotes the ground state, $A, B, C, \ldots$ denote exited states with the same spin multiplicity as the ground state, $a, b, c, \ldots$ denote excited states with a different

Table 6.3: Unpaired electron distribution between A' and A'' symmetry molecular orbitals.

dimer state	A'		A''	
	monomer 1	monomer 2	monomer 1	monomer 2
c^3A''	1	0	0	1
d^3A'	1	1	0	0
e^3A''	0	1	1	0
f^3A'	0	0	1	1
g^5A''	3	0	0	1
h^5A'	1	1	1	1
i^5A'	2	2	0	0
j^5A''	0	3	1	0

spin multiplicity from that of the ground state. A distinction between B^1A' and C^1A' is the permutation of AlF monomers in each state. A similar case with E^1A' and F^1A' states. For the triplet and quintuplet states for which both the AlF monomers are in $a^3\Pi$ state, the difference in unpaired electron distribution is recorded in Tab. 6.3. The states f^3A' and j^5A'' remain unreported as our MRCI calculations either did not converge well or the converged points were not continuous.

The optimisation of AlF-AlF ground state equilibrium geometry is done using analytic gradient of energy. The level of theory used is CCSD/aug-cc-pVTZ.

6.2 Results

6.2.1 Ground state X^1A'

We have calculated the potential energy surface of AlF-AlF interaction. Within the rigid rotor approximation, we obtain a four dimensional potential energy surface. We used CCSD(T)X2C/aug-cc-pVQZ-X2C, to calculate the ground state interaction energy surface. We calculated the potential energy surface on a grid of about 8700 points in $(\theta_1, \theta_2, \phi, r)$. It is a closed-shell complex with a potential depth of $12903\ \mathrm{cm}^{-1}$. The potential energy surface we calculated gives us a potential depth of only $1846\ \mathrm{cm}^{-1}$ but the CCSD optimization of the dimer led us to a much deeper minima. This shows that the rigid rotor approximation is highly inaccurate and is inadequate for this system. The rigid rotor approximation only led us to a local minima which is much shallower than the global minima of the complex. To compare with similar other complexes, the well depth of $\mathrm{KRb} - \mathrm{KRb}$ interaction is $2888.78\ \mathrm{cm}^{-1}$ [260], of $\mathrm{CaF} - \mathrm{CaF}$ interaction is $8760\ \mathrm{cm}^{-1}$ [261], of $\mathrm{NaK} - \mathrm{NaK}$ interaction is $4534\ \mathrm{cm}^{-1}$ [262]. AlF-AlF complex remains a relatively strongly bound dimer compared to the above complexes.

Fig. 6.3 shows the one-dimensional cuts through the potential energy surface of AlF - AlF $\left(X^1\Sigma^+ - X^1\Sigma^+\right)$interaction. There are seven curves on the plot for seven different orientations. We see that the curve for AlF-dipole orientation is the deepest curve with a well depth of about $916\ \mathrm{cm}^{-1}$ at $R = 7$ bohr. The curves have varying minima located at different R meaning that this interaction is anisotropic. We can note that the potential energy curve for linear AlF-FAl

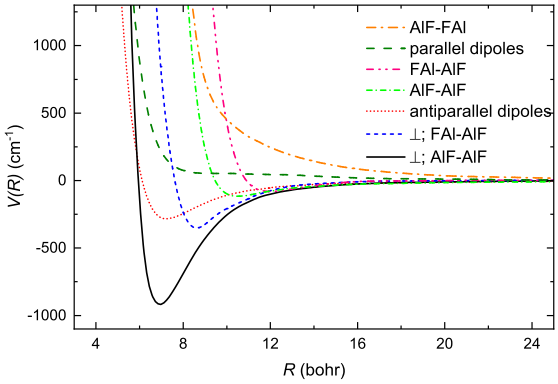

Figure 6.3: The one-dimensional cuts through the $X^1\Sigma^+ + X^1\Sigma^+$ground state potential energy surface of AlF-AlF is presented for seven selected configurations. The level of theory used is $\mathrm{CCSD(T)} - \mathrm{X2C/CBS}$.

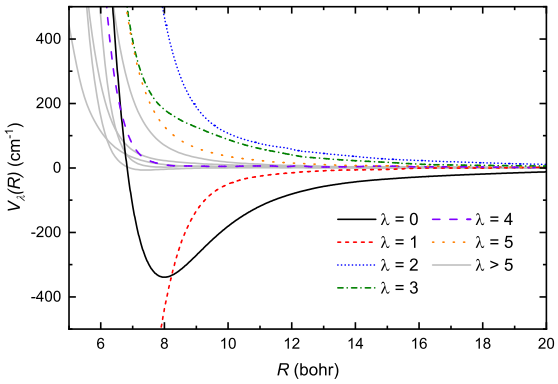

Figure 6.4: The first 11 Legendre components of a two dimensional cut through the potential energy surface is presented. The constant parameters here are $\theta_1 = 60°, \phi = 180°$.

is the most repulsive owing to the dense lone pair of electrons carried by both the fluorine atoms.

The first 11 Legendre components of two dimensional potential energy surface for $\theta_1 = 60°$, $\phi = 180°$ is presented in Fig. 6.4. The Legendre components help us visualise the anisotropy of the interaction. The anisotropic $\lambda = 1, 2, 3, 5$ component seem to dominate the interaction, the isotropic component $\lambda = 0$ also has a significant contribution while the rest of the components are relatively insignificant and also repulsive.

The convergence of the interaction energy for increasing levels of theory is presented in Fig. 6.5 for the linear AlF-AlF configuration using aug-cc-pVQZ basis set. The HF curve is completely repulsive meaning it is a very poor description of this interaction. The deepest curve we see here is the explicitly correlated $\mathrm{CCSD(T)}$-F12 energy which is only $5\ \mathrm{cm}^{-1}$ deeper than $\mathrm{CCSD(T)}$ energy. It is interesting to note that the difference in energy for CCSD and $\mathrm{CCSD(T)}$ is about $36\ \mathrm{cm}^{-1}$ which is 45% of the $\mathrm{CCSD(T)}$ interaction energy. In the case of $\mathrm{AlF} - \mathrm{He}$, this difference is about $3.2\ \mathrm{cm}^{-1}$ (aug-cc-pVQZ) which is 15% of $\mathrm{CCSD(T)}$ energy and for the AlF molecule it is $1164\ \mathrm{cm}^{-1}$ (aug-cc-pVQZ), 2% of the $\mathrm{CCSD(T)}$ interaction en-

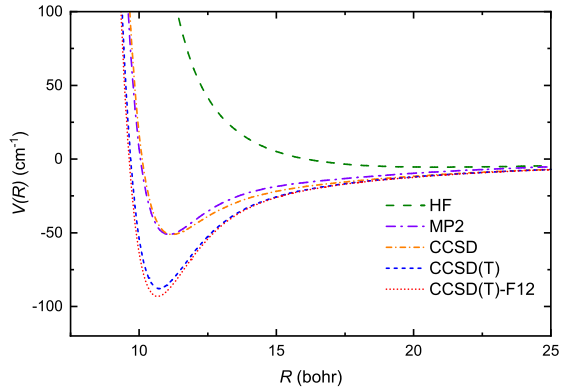

Figure 6.5: The convergence of the interaction energy for different levels of theory for the linear AlF-AlF configuration in X^1A' state. The basis set used is aug-cc-pVQZ.

ergy. The perturbative triples correction contribution is bigger for systems with greater number of electrons.

The basis set convergence of the interaction energy is shown in Fig. 6.6. The deepest curve is for the $\mathrm{CCSD(T)-X2C/CBS}$ curve which is what we implemented to calculate the four dimensional ground state potential energy surface. We should note that $\mathrm{CCSD(T)}$ /aug-cc-pV5Z curve is shallower than $\mathrm{CCSD(T)-F12/}$ aug-cc-pVQZ-F12 curve but the use of the F12 term improves the $\mathrm{CCSD\,(T\ )}$ interaction energy by about $1\ \mathrm{cm}^{-1}$ (aug-cc-pVQZ-F12) and $2\ \mathrm{cm}^{-1}$ (aug-cc-pV5ZF12). We conclude that the complete basis set limit of non-relativistic $\mathrm{CCSD(T)}$ interaction energy is about 96.06 cm^{-1}. The relativistic $\mathrm{CCSD(T)-X2C}$ calculation exhibits convergence with basis set cardinal number, similar to the non-relativistic calculation. The difference between $\mathrm{CCSD(T)-\ X2C/}$ aug-cc-pCVQZ-X2C and $\mathrm{CCSD(T)-X2C/CBS}$ is about $6\ \mathrm{cm}^{-1}$ (the difference between $\mathrm{CCSD(T)}$-F12/aug-cc-pV5Z-F12 and $\mathrm{CCSD(T)}$ /aug-cc-pVQZ is about $5\ \mathrm{cm}^{-1}$), which is about half of the $11.8\ \mathrm{cm}^{-1}$ scalar relativistic correction. We estimate the complete basis set limit of relativistic $\mathrm{CCSD(T)}$-X2C interaction energy as -113.76 cm^{-1}.

I have generated four two-dimensional cuts through the X^1A' state potential energy surface of AlF-AlF dimer. The two dimensional curve gives us an idea of the nature of interaction with respect to specific parameters. Despite the local minima that we see in Fig. **??**, the only minima that this dimer has is the global minima at $R = 4.5\mathrm{bohr}, \theta_1 = 71^\circ, \theta_2 = 60^\circ, \phi_1 = 180^\circ$ which is seen in Fig. 6.10 with a well depth of $1846\ \mathrm{cm}^{-1}$. The other local minima only appear in the two dimensional cuts where two other parameters are frozen. No local minima were obtained in CCSD optimization, the dimer always ends up in the global minima configuration.

Fig. 6.7 shows the two-dimensional cuts through the ground state potential energy in which we can see that the interaction is highly anisotropic to change in θ_2. The change in configuration of the $\mathrm{AlF-AlF}$ complex with θ_2 is visually represented inside the plot. Despite aluminium being a bigger atom than flourine, the configuration at $\theta_2 = 180^\circ$ is more attractive than at $\theta_2 = 0^\circ$. At any given point in R, the $\theta_2 = 71^\circ$ configuration has the lowest energy. An interesting feature about the AlF-AlF interaction is that there is only one minima in the whole interaction landscape. Our optimisation of AlF-AlF dimer always led to the same global minima

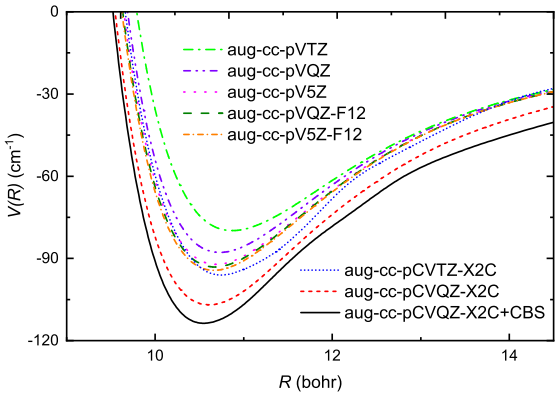

Figure 6.6: The convergence of the interaction energy for increasing basis set cardinal number for the linear AlF-AlF configuration in the X^1A' state. The level of theories used are $\mathrm{CCSD(T)}, \mathrm{CCSD(T)-F12}, \mathrm{CCSD(T)-X2C}$.

we see in Fig. 6.7 no matter what the starting configuration is. Global minima is also seated well inside a repulsive wall, accessible only for a short range of the Jacobi distance.

Fig. 6.8 shows the two dimensional cuts through the ground state potential energy surface for change in the azimuthal angle ϕ for $\theta_1 = 90°, \theta_2 = 90°$. The depth is $300\ \mathrm{cm}^{-1}$ and the minima lies at a skewed geometry with $\phi = 120°$. Change in azimuthal angle seems to influence a change in energy of at most $300\ \mathrm{cm}^{-1}$.

Fig. 6.9 represents the two dimensional cuts through the ground state potential energy surface for $R = 12.2$ bohr, $\phi = 0.1$ where θ_1 and θ_2 are varied. We can observe that the plot is symmetric around the line $\theta_1 = \theta_2$. There is a local minima at $\theta_1 = 120°, \theta_2 = 0°$ at $130\ \mathrm{cm}^{-1}$. It is interesting to see the change in interaction energy as the dimer configuration changes.

Fig. 6.10 shows the two dimensional cuts through the ground state potential energy surface when an AlF molecule is rotated around another molecule ($\phi = 0°$). Owing to the symmetry of the system, Fig 6.10 is representative of a complete rotation of an AlF molecule around another molecule. So it is enough to present only angles from $0°$ to $90°$. The linear configuration at $(0°, 180°)$ seems to be highly repulsive.

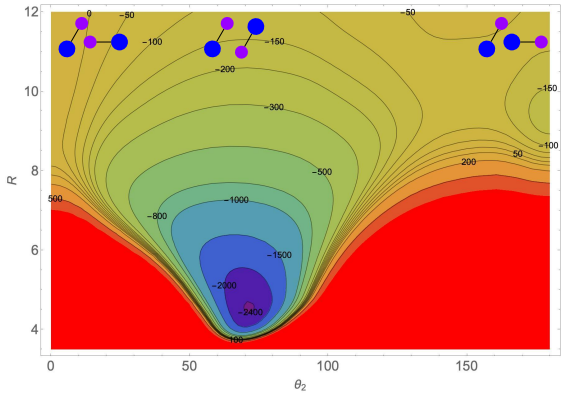

Figure 6.7: The two dimensional cuts through the $X^1\Sigma^+ + X^1\Sigma^+$ground state potential energy surface of AlF-AlF with respect to R and θ_2 for $\theta_1 = 60°, \phi = 180°$. The level of theory used is $\mathrm{CCSD(T)-X2C/CBS}$.

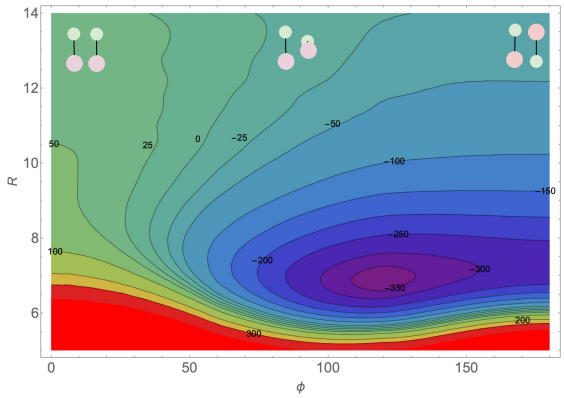

Figure 6.8: The two dimensional cuts through the $X^1\Sigma^+ + X^1\Sigma^+$ground state potential energy surface of AlF-AlF with respect to R and ϕ for $\theta_1 = 90°, \theta_2 = 90°$. The level of theory used is $\mathrm{CCSD(T)-X2C/CBS}$.

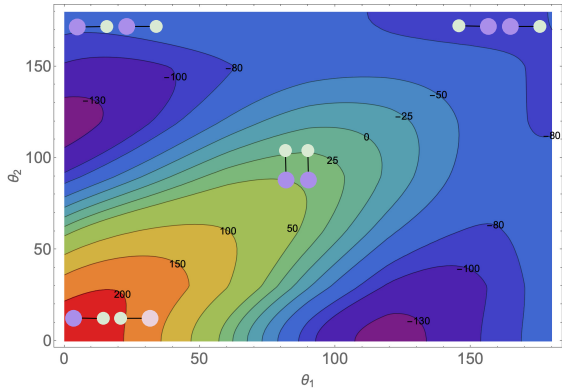

Figure 6.9: The two dimensional cuts through the $X^1\Sigma^+ + X^1\Sigma^+$ground state potential energy surface of AlF-AlF with respect to θ_1 and θ_2 for $R = 12.2\text{bohr}, \phi = 0°$. The level of theory used is CCSD(T)-X2C/CBS.

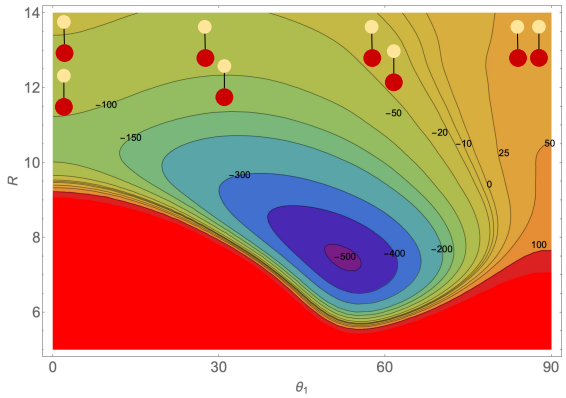

Figure 6.10: The two dimensional cuts through the $X^1\Sigma^+ + X^1\Sigma^+$ground state potential energy surface of AlF-AlF with respect to R and θ_1 for $\theta_2 = 180° - \theta_1, \phi = 0°$. The level of theory used is $\text{CCSD(T)} - \text{X2C}/\text{CBS}$.

6.2.2 Optimization

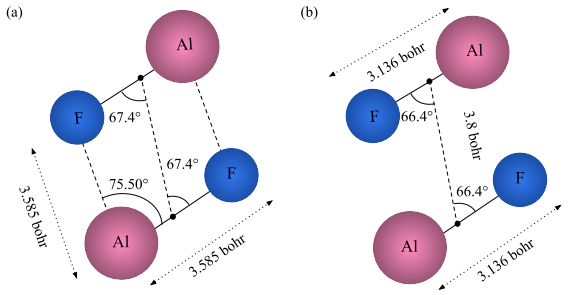

Figure 6.11: (a) The optimized geometry of the AlF-AlF dimer without rigid rotor approximation. (b) The global minima AlF-AlF configuration within rigid rotor approximation.

An optimization of the AlF-AlF dimer geometry was done using CCSD method. The global minimum geometry was found to be a rhombus as seen in Fig. 6.11 (a). The depth of the well D_e for the global minimum is $11546\ \mathrm{cm}^{-1}$ (CCSD/aug-cc-pVTZ). The lowest vibrational frequency is in A'' symmetry at $143.3\ \mathrm{cm}^{-1}$ and the second lowest vibrational frequency is in A' symmetry at $251.9\ \mathrm{cm}^{-1}$. The $\mathrm{CCSD(T)-X2C/}$ aug-cc-pCVQZ-X2C single point calculation at the global minimum geometry gives a well depth of $12900\ \mathrm{cm}^{-1}$. Fig. 6.11 (b) shows the global minima configuration within the rigid rotor approximation with a well depth of about $2400\ \mathrm{cm}^{-1}$.

Fig. 6.12 shows the one-dimensional interaction energy curve against the coordinate R. It probes the interaction through the global minima geometry but within the rigid rotor approximation. Complete parametric optimization of the dimer results in a much deeper potential of $12900\ \mathrm{cm}^{-1}$. This shows us that rigid rotor approximation does not accurately describe this interaction at short range.

6.2.3 Potential energy curves for excited states

The one-dimensional potential energy curves for different spin and electronic states of AlF-AlF dimer has been presented in this Section. The common observation is that the first triplet excited states with $X^1\Sigma^+ + a^3\Pi$ asymptotes, c^3A' and d^3A', are well separated from the higher excited states.

For the linear configuration AlF-AlF in Fig. 6.14 , the ground state has a shallow potential well of about $87\ \mathrm{cm}^{-1}$ with the position of minima at $R = 10$ bohr. The ground state well depth of FAl-AlF linear configuration in Fig. 6.18 is $74\ \mathrm{cm}^{-1}$ deep with the position of minima at 12 bohr. The ground state of AlF-FAl linear configuration presented in Fig. 6.16 has no attractive well owing to the interaction between two electron dense flourine molecules. Similarly, the AlF-AlF parallel configuration seen in Fig. 6.17 also has a completely repulsive potential energy curve for the ground state. The deepest potential well is observed for $\perp$; AlF-AlF configuration which is about $500\ \mathrm{cm}^{-1}$ at 7.4 bohr as seen in Fig. 6.15 while the position of minima lies at the shortest intermonomer separation for the AlF-AlF antiparallel configuration at 6.8 bohr with

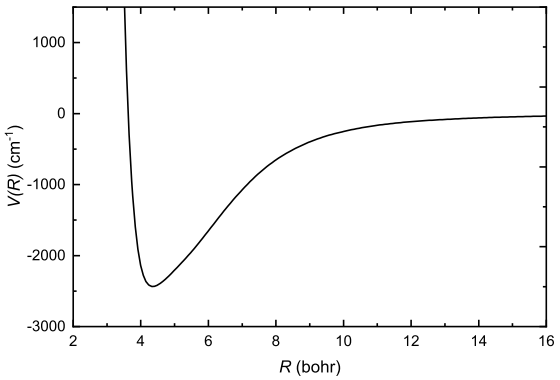

Figure 6.12: One-dimensional cut through the ground state potential energy surface. The respective orientation of monomers is characterised by the following angles: $\theta_1 = 67.43°$, $\theta_2 = 67.43°, \phi = 180°$.

a depth of about $393\,\mathrm{cm}^{-1}$ seen in Fig. 6.13. The ground state potential energy curve are in agreement with the more accurate computation described in previous section.

The four excited triplet states of AlF-AlF with $X^1\Sigma^+ + a^3\Pi$ asymptotes are a^3A'', b^3A'', c^3A' and d^3A'. The position of the minima of the b^3A'' state is at the shortest intermonomer separation for the antiparallel configuration at 4.5 bohr with a depth of $1757\,\mathrm{cm}^{-1}$ Fig. 6.13 and the same for the c^3A' state is at 4 bohr with a depth of about $5200\,\mathrm{cm}^{-1}$ Fig. 6.13. For the antiparallel configuration, the a^3A'' and d^3A' states seem repulsive. In the linear AlF-FAl configuration seen in Fig. 6.16, the states a^3A'', b^3A'' and c^3A', d^3A' are repulsive and overlap each other. The repulsive behaviour of these states and the complete overlap of states with same asymptotes repeats for higher excited states too. For the linear FAl-AlF configuration, we observe a crossing between the ground state and c^3A' state at 7.5 bohr and more importantly, a crossing between the a^3A'' and e^3A'' state at 8 bohr. In the linear FAl-AlF configuration in Fig. 6.18, the depth of the b^3A'' and c^3A' states are about $9800\,\mathrm{cm}^{-1}$ and $9400\,\mathrm{cm}^{-1}$ at $7.6\mathrm{bohr}$, respectively. To compare with the AlF-AlF configuration (Fig. 6.14, which has b^3A'' and c^3A' depths as $280\,\mathrm{cm}^{-1}$ and $954\,\mathrm{cm}^{-1}$ respectively, the b^3A'' and c^3A' states are much deeper for the linear FAl-AlF configuration. For the parallel configuration seen in Fig. 6.17, the depth of b^3A'' is about $6500\,\mathrm{cm}^{-1}$ at 5 bohr while the depth of c^3A' is about $8000\,\mathrm{cm}^{-1}$ at $5.25\mathrm{bohr}$. a^3A' and d^3A' states are repulsive. For the parallel configuration, the minima of the states A^1A'' and b^3A'' are separated by $6335\,\mathrm{cm}^{-1}$. For the FAl-AlF perpendicular configuration in Fig. 6.19, the repulsive wall of X^1A' state crosses both the c^3A' and the d^3A' states at around 6 bohr and it crosses B^1A' state at 5.8 bohr. In the AlF-AlF perpendicular configuration in Fig 6.15, the a^3A'' has the deepest well of about $23100\,\mathrm{cm}^{-1}$. Comparing the two perpendicular configurations (Fig. 6.15 and Fig. 6.19), a very important distinction to note is that AlF-AlF perpendicular configuration shows no crossing between X^1A' and the higher states which is not the case with FAl-AlF perpendicular configuration. A general observation is that more the number of fluorine atoms present at the interaction site, more repulsive the interaction.

The four excited singlet states of AlF-AlF with $X^1\Sigma^+ + A^1\Pi$ asymptotes are A^1A'', B^1A', C^1A', D^1A''. For the AlF-AlF linear configuration, the well depth of B^1A' and C^1A' states

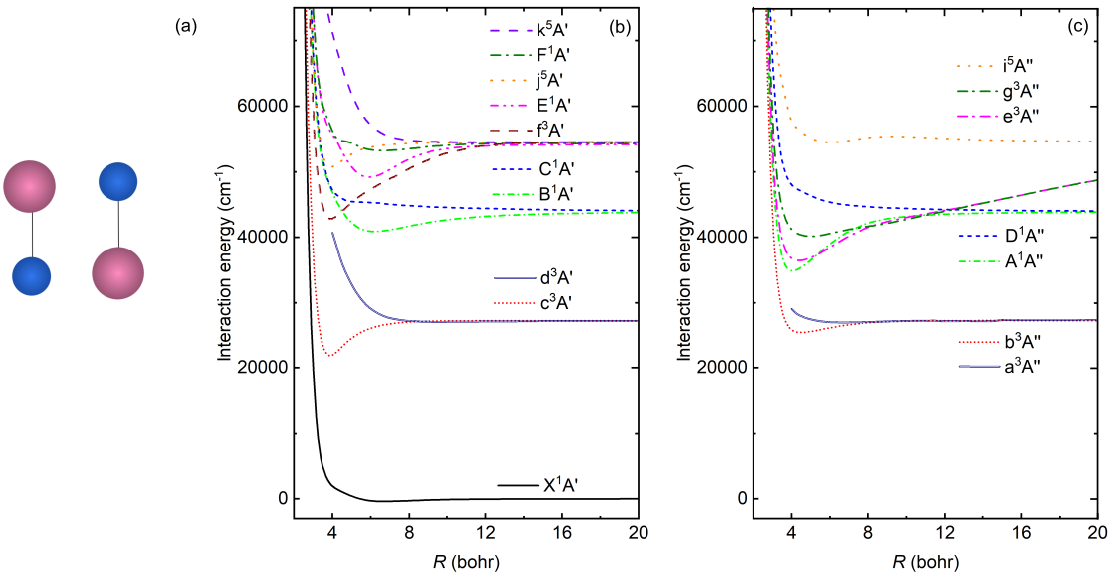

Figure 6.13: The one-dimensional potential energy curves for different spin states of AlF-AlF system for the anti parallel configuration (a) is presented. The potential energy curve for A' and A'' states are presented in panel (b) and panel (c) respectively.

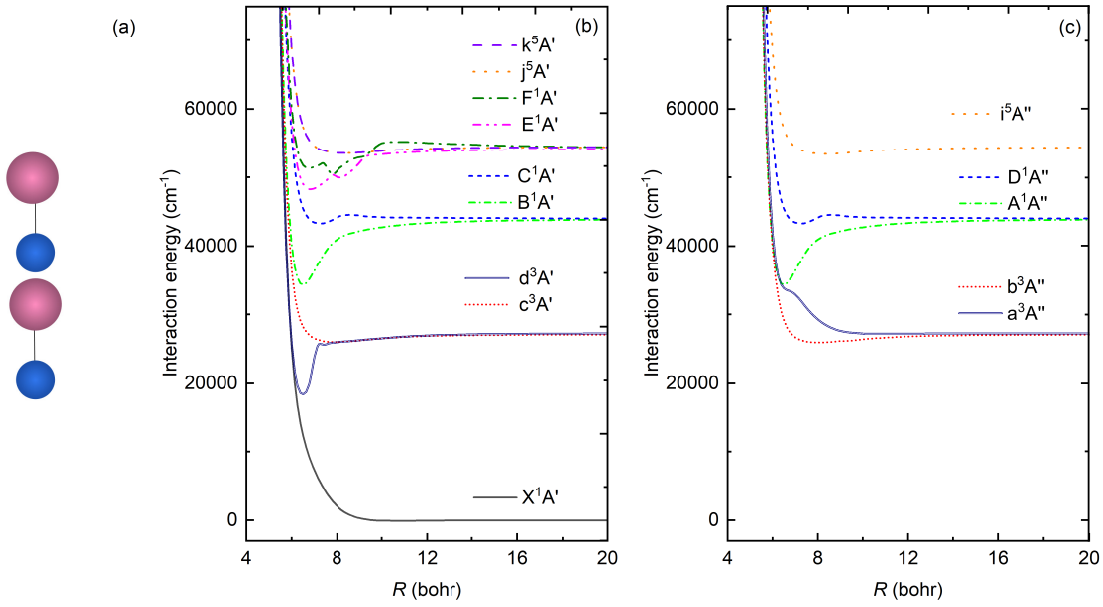

Figure 6.14: The one-dimensional potential energy curves for different spin states of AlF-AlF system for the linear AlF-AlF configuration (a) is presented. The potential energy curve for A' and A'' states are presented in panel (b) and panel (c) respectively.

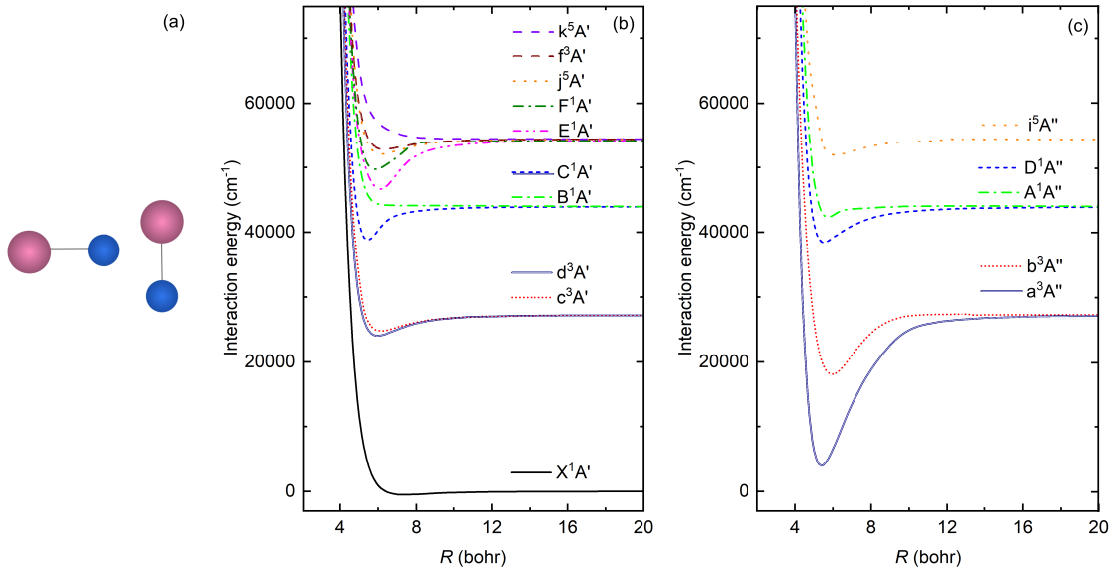

Figure 6.15: The one-dimensional potential energy curves for different spin states of AlF-AlF system for the perpendicular configuration (a) is presented. The potential energy curve for A' and A'' states are presented in panel (b) and panel (c) respectively.

seem to be well separated by about $8980\ \mathrm{cm}^{-1}$. The states C^1A' and B^1A' do not cross any of the higher excited states. The D^1A'' state is repulsive with no attractive potential well. For the AlF-AlF perpendicular configuration, the states C^1A' and B^1A' do not cross any of the higher excited states. It is interesting to note that only for AlF-AlF perpendicular configuration, the state C^1A' is deeper than B^1A' and D^1A'' is deeper than A^1A''. Due to the lower symmetry of the non-linear configuration, the states with the same asymptotes do not overlap each other. In contrast, for AlF-AlF linear configuration Fig. 6.14, the curves in panel (c) and (b) with the same asymptotes look identical.

For the AlF-FAl linear configuration, the C^1A', B^1A' states and the D^1A'', A^1A'' states almost overlap each other with a difference of about $600\ \mathrm{cm}^{-1}$ visible in Fig. 6.16. The Π symmetry of the monomer in $A^1\Pi$ state becomes irrelevent due to the reduced symmetry of the configuration as both the π molecular orbitals are perpendicular to the molecular axis. The difference in energy between C^1A' and B^1A' states is the highest for the FAl-AlF perpendicular configuration. The B^1A' state has the monomer 1 in $A^1\Pi$ state with the π molecular orbitals parallel to monomer 2 . While in C^1A' state, the monomer 2 is in $A^1\Pi$ state with the π molecular orbitals near the aluminium of monomer 1 , creating more repulsion. The well depth of $15000\ \mathrm{cm}^{-1}$ for A^1A' state is deepest for the FAl-AlF perpendicular configuration. In the Fig. 6.18, the separation of the potential well is highest between the D^1A'' and A^1A'' states by $21144\ \mathrm{cm}^{-1}$.

The higher excited singlet states F^1A' and E^1A' have the asymptotes $X^1\Sigma^+ + B^1\Sigma^+$and they both have Σ symmetry. A crossing between F^1A' and E^1A' states is observed for the AlF-AlF and the FAl-AlF linear configurations as can be observed in Fig. 6.14 and Fig. 6.18 respectively. For the AlF-FAl linear configuration, the F^1A' and E^1A' states completely overlap each other

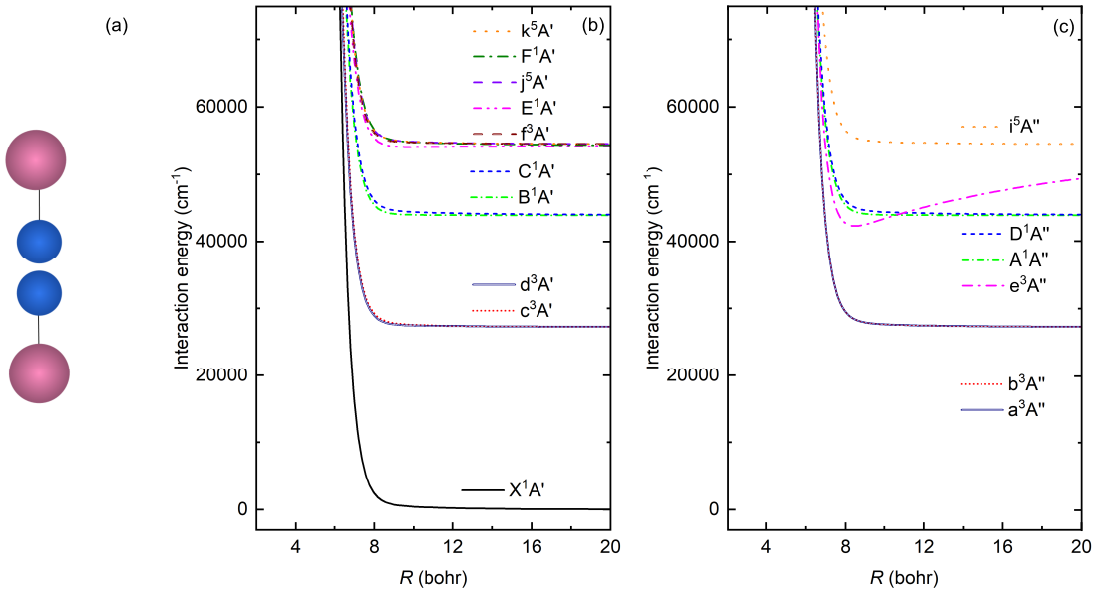

Figure 6.16: The one-dimensional potential energy curves for different spin states of AlF-AlF system for the linear AlF-FAl configuration (a) is presented. The potential energy curve for A' and A'' states are presented in panel (b) and panel (c) respectively.

seen in Fig. 6.16. The E^1A' state is deepest for the FAl-AlF linear configuration with a well depth of about 19800 cm^{-1}. The F^1A' and E^1A' minima are the most separated for the parallel configuration as seen in Fig. 6.17.

The high-spin states i^5A'', j^5A', k^5A' have the asymptotes $a^3\Pi + a^3\Pi$. For the AlF-AlF linear configuration in Fig. 6.14, the j^5A' and k^5A' states overlap each other completely. The π molecular orbitals are perpendicular to the molecular axis hence the electronic occupation in j^5A' and k^5A' states remain equivalent in a linear configuration. i^5A' state seems to have an avoided crossing from a higher state at 6 bohr. The i^5A'' state seems to be well separated from the other states for all the selected configurations except for the FAl-AlF linear configuration, there is a crossing between i^5A'' and D^1A'' states at about 7.5 bohr. An observation about the k^5A'' state is that this state remains consistently repulsive for all the configurations except for the AlF-AlF linear configuration where there is a shallow potential well about 1000 cm^{-1} deep seen in Fig. 6.14. All the curves in Fig. 6.15 have an attractive potential well except the k^5A' state.

The second set of excited triplet states are e^3A'', f^3A', g^3A'' with the same asymptotes $a^3\Pi + a^3\Pi$. For the antiparallel configuration seen in Fig. 6.13, the g^3A'' and e^3A'' states remain attractive over a long range but the f^3A' state has the same asymptotes but remains attractive only for a short range of inter monomer separation. We see a difference in curves between g^3A'' and e^3A'' states only in the short range, after 12 bohr they overlap each other.

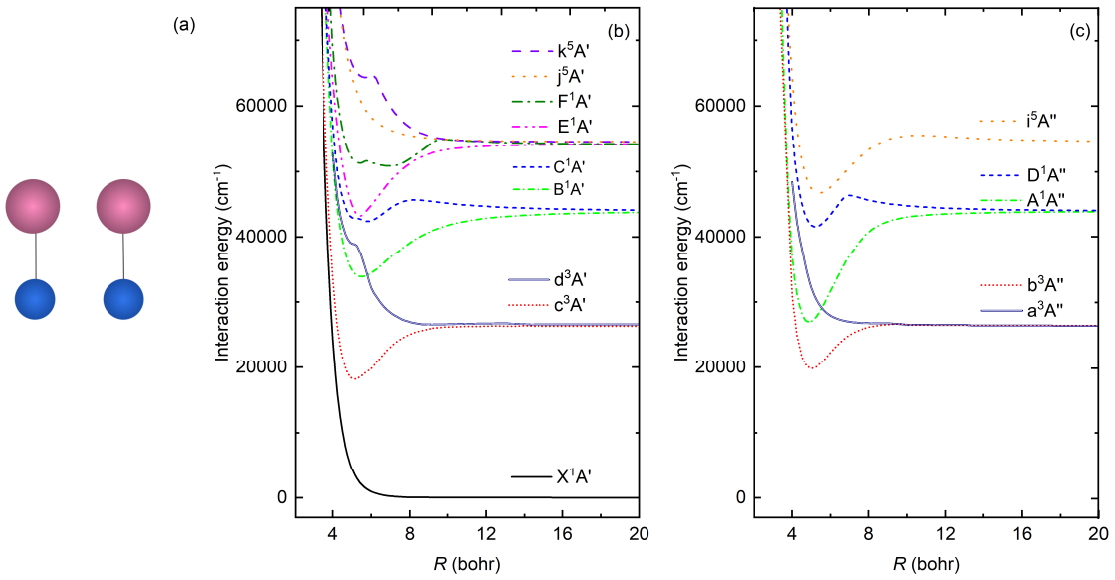

Figure 6.17: The one-dimensional potential energy curves for different spin states of AlF-AlF system for the parallel configuration (a) is presented. The potential energy curve for A' and A'' states are presented in panel (b) and panel (c) respectively.

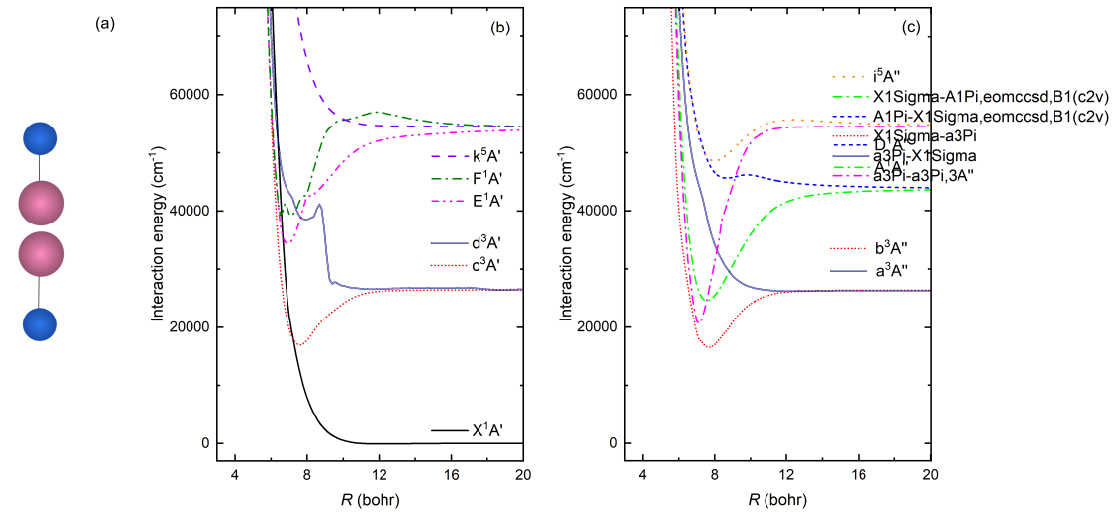

Figure 6.18: The one-dimensional potential energy curves for different spin states of AlF-AlF system for the linear FAl-AlF configuration (a) is presented. The potential energy curve for A' and A'' states are presented in panel (b) and panel (c) respectively.

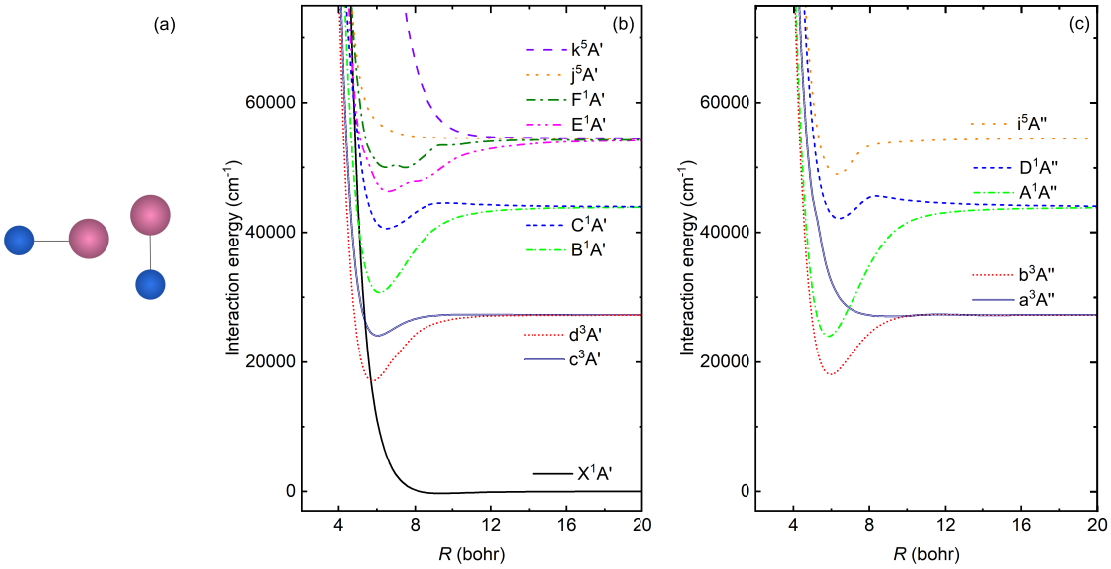

Figure 6.19: The one-dimensional potential energy curves for different spin states of AlF-AlF system for the perpendicular configuration (a) is presented. The potential energy curve for A' and A'' states are presented in panel (b) and panel (c) respectively.

6.3 Conclusion

We have calculated an accurate potential energy surface of the X^1A' state of AlF-AlF interaction. The interaction is highly anisotropic but attractive. The potential energy surface has only one minima (global minima). It is surprising that there is no local minima for the AlF-AlF interaction. The global minima configuration is a rhombus structure with a depth of $12900\ \mathrm{cm}^{-1}$. The difference in the AlF-AlF ground state well depth with rigid rotor approximation and complete optimization is $10500\ \mathrm{cm}^{-1}$ which is huge. We conclude that rigid rotor approximation poorly describes the AlF-AlF interaction in the short range. We explored the excited potential energy surface for seven selected configurations. It is important to note that the first excited state a^3A' is separated from the ground state and the higher excited states for all the selected configurations of the AlF-AlF complex.

7 AlF-Rb

The first realisation of Bose-Einstein condensate was in a dilute gas of rubidium-87 atoms at 170 nanokelvein [6]. Since then the rubidium has become one of the most researched atom in ultracold physics. Ultracold rubidium atoms have been successfully used to sympathetically cool atoms like ytterbium [257], lithium [258], rubidium-85 [259] and molecules like OH^- [260]. In this chapter, we report the potential energy surfaces for the interaction between aluminium monoflouride molecule and rubidium atom to study the possibility of sympathetic cooling of AlF molecules and observing magnetic Feshbach resonances in this system.

The ground state of rubidium atom is a doublet $^2S_{1/2}$ and that of aluminium monoflouride molecule is $X^1\Sigma^+$. The ground state of AlF-Rb dimer is X^2A'. The electronic structure calculation of AlF-Rb interaction energy will help us model sympathetic cooling of AlF molecules in by rubidium.

Table. 7.1 lists the AlF-Rb states I study in his chapter. The potential energy surfaces for the ground state, first two excited doublet states and two high-spin quartet states are reported. In this chapter, we discuss the relevant methods used and report the potential energy surfaces of the AlF-Rb interaction in ground and few excited states. These calculations are a starting point to understand the nature of AlF-Rb interaction which is essential for sympathetic cooling of AlF molecule using cold Rb atoms.

7.0.1 Methods

I used the exact two-component coupled cluster single double and perturbative triples method with relativistic basis set (CCSD(T)-X2C/aug-cc-pwCVQZ-X2C) [261, 262, 263] to calculate the potential energy surfaces for the AlF- Rb interaction in its ground state X^2A' and in the high-spin states $^4A'$ and $^4A''$. A weighted core-valence basis set is used to improve the description of core-valence electron correlation. For the excited states B^2A' and A^2A'', MRCI/aug-cc-

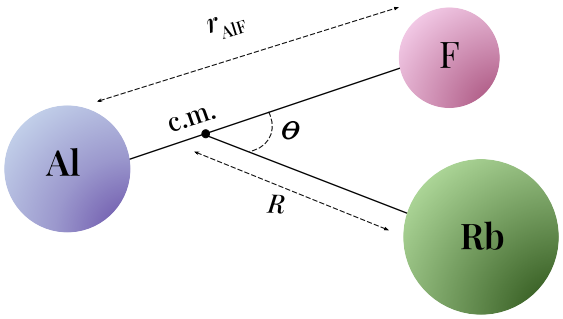

Figure 7.1: The Jacobi coordinates for the AlF+Rb systems.

Table 7.1: AlF-Rb states we report on.

Molecular states	Asymptotic states	Methods
X^2A'	$X^1\Sigma^+ + {}^2S$	CCSD(T)-X2C
B^2A'	$X^1\Sigma^+ + {}^2P$	MRCI
A^2A''	$X^1\Sigma^+ + {}^2P$	MRCI
${}^4A'$	$a^3\Pi + {}^2S$	CCSD(T)-X2C
${}^4A''$	$a^3\Pi + {}^2S$	CCSD(T)-X2C

pwCVQZ-PP method is used. Pseudopotentials are used to prevent the explicit treatment of core electrons and for AlF-Rb due to large number of electrons. Pseudopotentials reduces the size of basis sets and number of explicitly treated electrons while also including the relativistic effects in turn reducing the computational effort [264].

The interaction energy, $V_{\text{int}}\,(R,\theta)$, is calculated using the supermolecular method as follows.

$$V_{int}(R,\theta) = E_{AlF+Rb}(R,\theta) - E_{AlF}(R,\theta) - E_{Rb}(R,\theta) \tag{7.1}$$

where E_{AlF+Rb} is the total energy of the complex, E_{AlF} and E_{Rb} are the energy of the monomers in the dimer basis set to account for basis set superposition error.

Analytic gradient of energy is used to optimise the AlF-Rb geometry. The optimisation of AlF-Rb coordinates was done using CCSD method with aug-cc-pVTZ basis set for aluminium and fluorine and the pseudopotential basis set ECP28MDF basis set for Rubidium.

7.0.2 Results

Fig. 7.2 (a) reports the potential energy surface of the ground state, X^2A'. The global minima of the ground state X^2A' lies at $R = 6$ bohr, $\theta = 58°$. The configuration is non-linear with rubidium near flourine. The depth of the potential is $1600\ \mathrm{cm}^{-1}$. The interaction appears to be anisotropic with a high repulsive wall near aluminium. Fig. 7.2 (b), shows the Legendre component of the potential energy surface. We see that the deepest component is the second Legendre component ($\lambda = 1$), followed by the fourth component. The zeroth component which is the isotropic part dominates the interaction in long range. We observe that the interaction is anisotropic in short range and remains isotropic in the long range. CCSD optimization of the AlF-Rb complex arrived at a minima where $R = 6.2\mathrm{bohr}, \theta = 60.3°, r_{AlF} = 3.32$ bohr. The complete optimization of the AlF-Rb complex still gives a global minima very close to the one obtained within the rigid-rotor approximation, confirming its validity.

The B^2A' state potential energy surface can be seen in Fig. 7.3 (a). The global minima of the interaction lies at $R = 7.74$ bohr, $\theta = 180°$ with a well depth of around $8800\ \mathrm{cm}^{-1}$. The global minima configuration is linear with rubidium near aluminium while a local minima of about $7500\ \mathrm{cm}^{-1}$ depth exists at a non-linear configuration with rubidium near flourine at $r = 6.2\mathrm{bohr}$, $\theta = 32°$. The potential energy surface seems to be highly anisotropic at short range but as we see in Fig. 7.3 (b), the isotropic Legendre component ($\lambda = 0$) seems to contribute significantly in long range. The interaction is dominated in the short range by the second Legendre component which is linear in $\cos\theta$. We can also note that in the short range up until

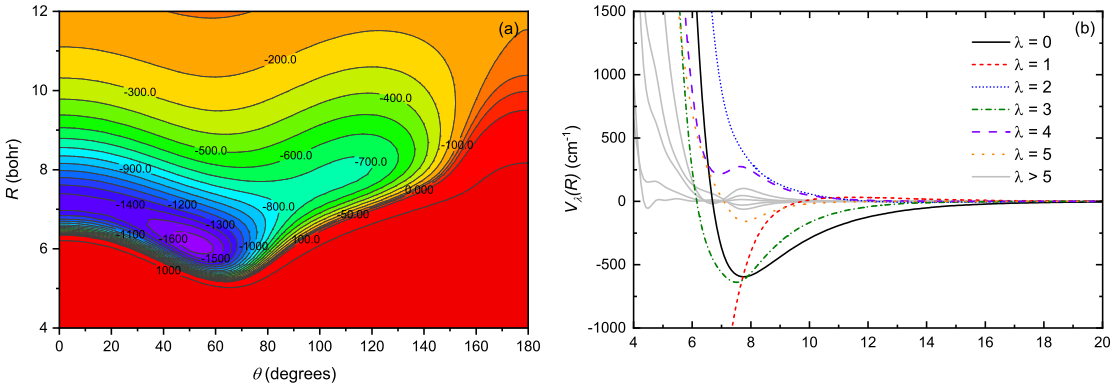

Figure 7.2: Panel (a) shows the two-dimensional cuts through the ground state potential energy surface of AlF-Rb interaction. Panel (b) shows the first 11 Legendre components of the potential energy surface. The level of theory used is $\mathrm{CCSD(T)} - \mathrm{X2C}/$ aug-ccpwCVQZ-X2C.

$R = 10\mathrm{bohr}$, the third and the fourth component ($\lambda = 2$ and $\lambda = 3$) also contribute significantly indicating the highly anisotropic nature of the interaction in short range.

Fig. 7.4 presents the potential energy surface of the A^2A'' state. The global minima is about $10300\ \mathrm{cm}^{-1}$ deep at $R = 7.5$ bohr, $\theta = 180°$ while there is a local minima at $R = 5.5$ bohr, $\theta = 61°$ of $9900\ \mathrm{cm}^{-1}$ depth. The global minima configuration is linear with rubidium near aluminium and the local minima configuration in non linear with rubidium near fluorine. Despite the differences in the depth, we can note the similarities between B^2A' and A^2A'' potential energy surfaces, they both have almost the same global minima configuration and also a local minima near fluorine. From the Legendre decomposition of A^2A'' we can observe that in long distance the isotropic $\lambda = 0$ component dominates the interaction and contributes significantly even in short range. At short range, the first Legendre component which is anisotropic contributes most to the interaction.

The quartet $^4A'$ state potential energy surface of AlF-Rb interaction is presented in Fig. 7.5. The global minimum lies at $R = 7$ bohr, $\theta = 0°$ which is a linear configuration with ruidium near fluorine. The depth of the potential well is about $1370\ \mathrm{cm}^{-1}$. Compared to the five states we report for AlF- Rb, it is interesting to note that there is a linear global minima configuration with rubidium near fluorine only for the $^4A'$ state. Unlike the other potentials, $^4A'$ potential has a high repulsive wall when rubidium approaches aluminium. This wall separates the global minima from a shallow local minima near the linear configuration at $R = 11\mathrm{bohr}, \theta = 180°$ with a depth of $150\ \mathrm{cm}^{-1}$. Another interesting thing to note is that the interaction landscape of AlF molecule ($a^3\Pi$) with rubidium atom is very similar in pattern to the interaction of AlF with He molecule b^3A'. The global minima of both the interactions lie near the linear configuration where the atom approaches the AlF molecule from the side of aluminium. Both the surfaces have a local minima near flourine which is separated by a huge repulsive region. So, in both cases, the most attractive part of the potential lies near the linear configurations.

Fig. 7.6 shows the potential energy surface for the $^4A''$ state. The global minima of the interaction lies near the perpendicular geometry at $R = 5.5$ bohr, $\theta = 62°$ with a well depth of about

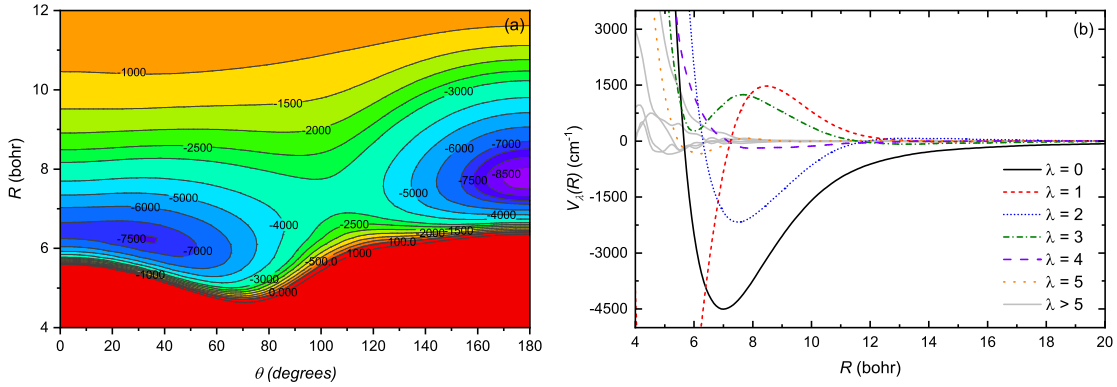

Figure 7.3: Panel (a) shows the two-dimensional cuts through the B^2A' state potential energy surface of AlF-Rb interaction. Panel (b) shows the first 11 Legendre components of the potential energy surface. The level of theory used is MRCI/aug-cc-pwCVQZPP.

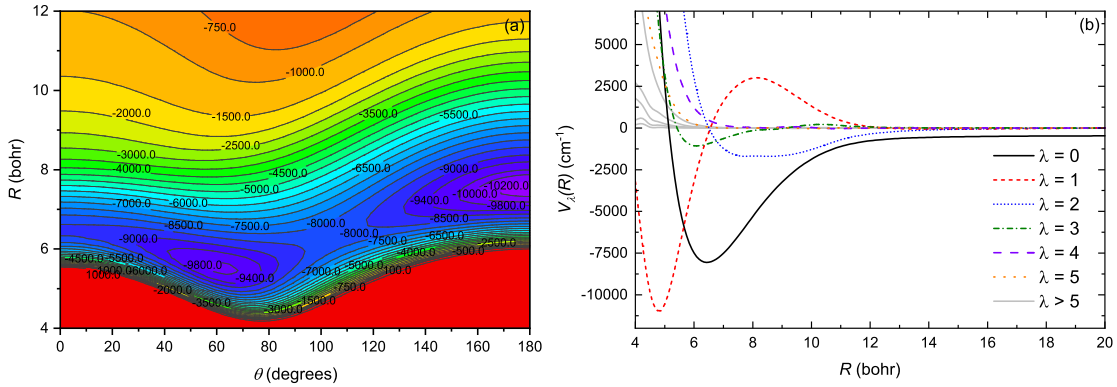

Figure 7.4: Panel (a) shows the two-dimensional cuts through the A^2A'' state potential energy surface of AlF-Rb interaction. Panel (b) shows the first 11 Legendre components of the potential energy surface. The level of theory used is MRCI/aug-cc-pwCVQZPP.

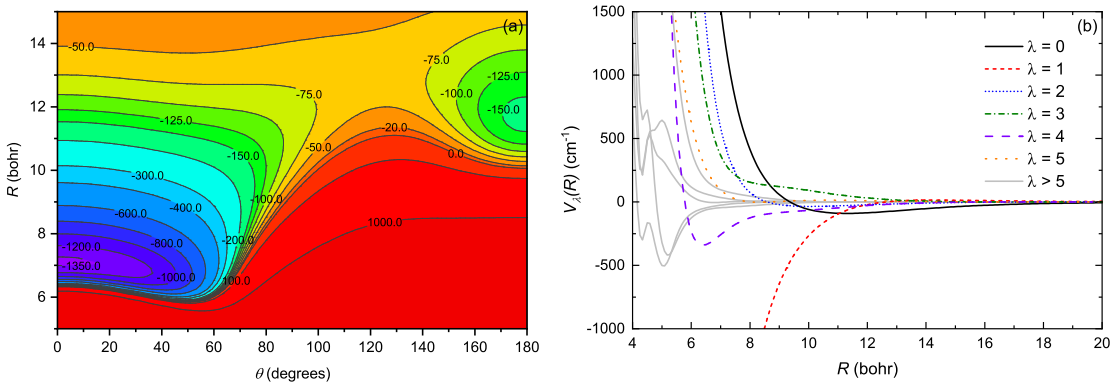

Figure 7.5: Panel (a) shows the two-dimensional cuts through the $^4A'$ state potential energy surface of AlF-Rb interaction. Panel (b) shows the first 11 Legendre components of the potential energy surface. The level of theory used is CCSD(T)-X2C/aug-ccpwCVQZ-X2C.

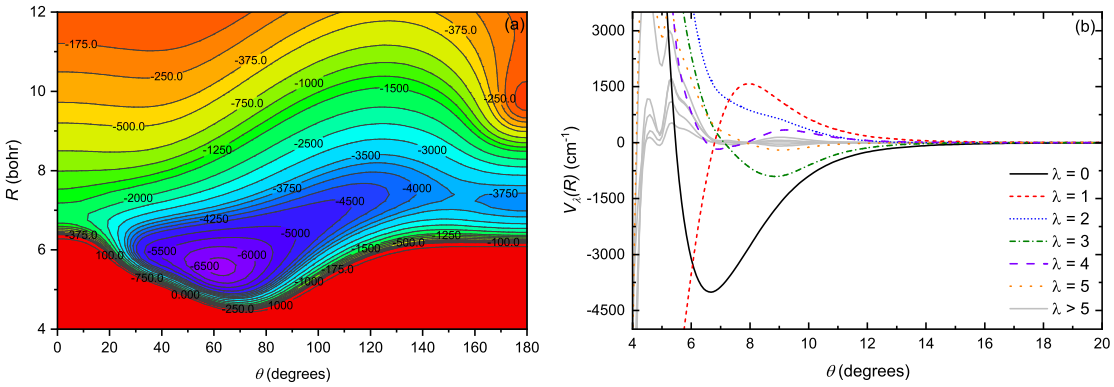

Figure 7.6: Panel (a) shows the two dimensional cuts through the $^4A''$ state potential energy surface of AlF-Rb interaction. Panel (b) shows the first 11 Legendre components of the potential energy surface. The level of theory used is CCSD(T) − X2C/ aug-ccpwCVQZ-X2C.

$6600\ \mathrm{cm}^{-1}$. There is a local minima at $R = 7.2\mathrm{bohr}, \theta = 180^{\circ}$ with a well depth of $3880\ \mathrm{cm}^{-1}$ which is separated from the global minima by a repulsive barrier of about $200\ \mathrm{cm}^{-1}$. The surface looks fairly isotropic indicated by the dominant isotropic $\lambda = 0$ Legendre component. But at short range, $\lambda = 1, 2, 3$ contribute significantly to the interaction. We should note that when AlF molecule is in the $a^3\Pi$ state, the resultant AlF-Rb states of different symmetries, $^4A'$ and $^4A''$, have completely different potential energy surfaces with a linear and near perpendicular non linear global minima configuration, respectively. As in the case of the $^4A'$ state, the $^4A''$ potential energy surface is also similar in shape to that of a^3A'' state of the AlF-He dimer. Both the potential energy surfaces have the global minima near the perpendicular geometry and at long inter monomer separation, the isotropic Legendre component $\lambda = 0$ dominate both the interactions.

7.0.3 Conclusion

We have reported the potential energy surfaces of AlF-Rb interaction for the states X^2A', B^2A', A^2A'', $^4A'$ and $^4A''$. The excited states of the AlF-Rb interaction are much deeper than the ground state X^2A' which is $1600\ \mathrm{cm}^{-1}$ deep. There are similarities between the potential energy surfaces of AlF-Rb and AlF-He interactions. The potential energy surfaces we report serve as an important starting point to understand the nature of this interaction and can be used further in scattering calculations. As atoms are easier to cool down than molecules due to their simple electronic structure, sympathetic cooling of molecules using ultracold atoms seems to be a viable option.

8 Summary and Outlook

The main results of this thesis is the detailed ab initio study of aluminium monoflouride molecule and its interaction with helium atom, with another AlF molecule and rubidium molecule. We were also able to observe the i) convergence of various ab initio methods to basis set cardinal number, , ii) significance of including core electron correlation, iii) significance of the relativistic correction and iv) the accuracy of rigid rotor approximation. As we are restricted to use finite basis sets, it is important to study the basis set cardinal number convergence to understand the accuracy that is achievable with a certain method. The interesting aspect is that these trends vary for the systems we studied. It is an important example to demonstrate how to perform an efficient ab initio electronic structure calculation for a particular system.

Buffer gas cooling is a broad cooling technique which can be used on any species and is a convenient and robust first step in the cooling technique. The ab initio study of AlF-He interaction and scattering shows great prospects for buffer gas cooling of AlF molecule. The AlF-He interaction is weak, anisotropic and uninfluenced by relativistic effects. We constructed highly accurate potential energy surfaces using the explicitly correlated coupled cluster method for the AlF-He interaction. Coupled channel scattering theory was then used to calculate the scattering cross sections of the AlF-He collision outcomes. The uncertainty of the potential energy surface were estimated, and the sensitivity of the scattering results to the scaling of the potential was studied to give us a better idea of the predictability of the results. The ratio of elastic to inelastic collisions provides information on how the outcomes change with temperature. This helps us to determine the optimal temperature for buffer gas cooling, ensuring that we select the most favourable conditions for subsequent processes.

State of the art potential energy surfaces for the AlF-AlF interaction in its ground state is reported. The four-dimensional potential energy surface can be used in collision calculation to predict the outcome of evaporative cooling. Unlike the other interactions we have studies, AlF is a polar molecule with a dipole moment of $1.53\mathrm{D}$, hence AlF-AlF is special because of the dipolar interaction which are long range and anisotropic. The long distance behaviour of the interaction will be of the form $\frac{1}{r^3}$, where r is the intermonomer separation. The AlF-AlF is an interesting complex which has a global minima deep seated inside a highly repulsive wall within rigid-rotor approximation. It is important to note the complex, when allowed to relax, arrives exactly at one minima which is about $13 \cdot 10^3\ \mathrm{cm}^{-1}$ deep. The excited state potential energy curves we have reported for the seven selected configurations show the crossings and separation between the low lying and excited states.

The potential energy surface for 5 states of AlF-Rb dimer is reported. The ground state of the interaction is around $1600\ \mathrm{cm}^{-1}$ which is deeper compared to other complexes such as $\mathrm{NH}-\mathrm{Rb}$ ($630\ \mathrm{cm}^{-1}$) [268] and $\mathrm{OH}^- - \mathrm{Rb}\left(405\ \mathrm{cm}^{-1}\right)$ [265]. The excited doublet state of the AlF-Rb complex are much deeper and less anisotropic than the ground state. It is interesting to see that AlF molecule in $a^3\Pi$ state has a similar shape of interaction energy surface with helium and

rubidium but with different energy scales. The potential energy surfaces we report give us an insight into the interaction between rubidium and metal halides which are great candidates for ultracold studies. This result can be used for collision calculations to predict the outcome of sympathetic cooling and magnetic Feshbach resonances.

On the whole we present a comprehensive ab initio study of aluminium monoflouride and the underlying mechanisms for cooling AIF. Apart from providing a theoretical benchmark for experimental studies, this a great case study for effectively using ab initio methods.

A. Appendix A

A.1. The bound states for b^3A' and a^3A'' state of $\mathrm{AlF} + \mathrm{He}^\star$

Table A.1.: Bound states for b^3A' state of $\mathrm{AlF} + \mathrm{He}$. Energy in cm^{-1}. J is the total angular momentum, p is the parity of the state.

J^p			
0^+	-8.33	0.36	
1^-	-4.02		
1^+	-7.97	-4.05	-0.17
2^-	-3.27		
2^+	-7.26	-3.35	
3^-	-2.14		
3^+	-6.20	2.32	
4^-	-0.66		
4^+	-4.79	-0.96	
5^+	-3.05		
6^+	-0.98		

A. Appendix A

Table A.2.: Bound states for a^3A'' state of $\mathrm{AlF} + \mathrm{He}$. Energy in cm^{-1}.J is the total angular momentum, p is the parity of the state.

J^p												
0^+	-22.15	-11.98	-8.88	-5.29	-1.83	-0.19						
1^-	-21.15	-10.29	-5.77	-0.35								
1^+	-21.57	-21.30	-11.40	-10.70	-7.82	-6.76	-3.88	-2.29	-0.53			
2^-	-19.86	-19.08	-9.02	-7.70	-4.16	-2.47						
2^+	-20.48	-20.31	-19.04	-10.35	-9.91	-8.08	-6.36	-5.88	-3.41	-1.94	-1.15	
3^-	-17.98	-17.41	-15.73	-7.22	-6.34	-3.99	-2.02	-0.68				
3^+	-18.94	-18.86	-17.22	-15.74	-9.09	-8.36	-7.33	-4.51	-4.22	-4.03	-2.39	-2.45
4^-	-15.59	-15.20	-13.47	-11.29	-5.08	-4.17	-2.73					
4^+	-17.00	-16.96	-14.75	-13.52	-11.29	-7.44	-6.63	-5.58	-3.88	-1.77	-1.58	-0.58
5^-	-12.76	-12.50	-10.59	-8.65	-5.72	-2.68	-1.29	-0.80				
5^+	-14.66	-14.65	-11.71	-10.76	-8.66	-5.73	-5.43	-4.71	-2.95	-2.71		
6^-	-9.55	-9.37	-7.10	-5.48	-2.80							
6^+	-11.93	-11.92	-8.24	-7.46	-5.48	-3.18	-2.81	-2.15	-1.12			
7^-	-5.98	-5.84	-3.16	-1.74								
7^+	-8.82	-8.79	-4.48	-3.75	-1.77	-0.53						
8^-	-2.07	-1.93										
8^+	-5.32	-5.29	-0.58									
9^+	-1.46	-1.42										

Bibliography

[1] John Weiner et al. “Experiments and theory in cold and ultracold collisions”. In: *Rev. Mod. Phys.* 71 (1 Jan. 1999), pp. 1–85.

[2] Eugene P Wigner. “On the behavior of cross sections near thresholds”. In: *Phys. Rev.* 73.9 (1948), p. 1002.

[3] Albert Einstein. “Sitzber, Kgl preuss”. In: *Akand. Wiss* 261 (1924).

[4] A Einstein. *Quantum Theory of a Monoatomic Ideal Gas A translation of Quantentheorie des einatomigen idealen Gases (Einstein, 1924)*. Vol. 1. 1. Sber. Preuss. Akad. Wiss, 1925.

[5] Bose. “Plancks gesetz und lichtquantenhypothese”. In: *Z. Phys.* 26.1 (1924), pp. 178–181.

[6] M. H. Anderson et al. “Observation of Bose-Einstein Condensation in a Dilute Atomic Vapor”. In: *Science* 269.5221 (1995), pp. 198–201.

[7] Kendall B Davis et al. “Bose-Einstein condensation in a gas of sodium atoms”. In: *PRL* 75.22 (1995), p. 3969.

[8] H. Kamerlingh Onnes. “Further experiments with liquid helium. C. On the change of electric resistance of pure metals at very low temperatures etc. IV. The resistance of pure mercury at helium temperatures”. In: *Proc. K. Ned. Akad. Wet., Ser. B* 13 (Jan. 1910), pp. 1274–1276.

[9] S Ospelkaus et al. “Quantum-state controlled chemical reactions of ultracold potassium-rubidium molecules”. In: *Science* 327.5967 (2010), pp. 853–857.

[10] FH Mies, Eite Tiesinga, and Paul S Julienne. “Manipulation of Feshbach resonances in ultracold atomic collisions using time-dependent magnetic fields”. In: *PRA* 61.2 (2000), p. 022721.

[11] Christian Gross and Immanuel Bloch. “Quantum simulations with ultracold atoms in optical lattices”. In: *Science* 357.6355 (2017), pp. 995–1001.

[12] Martin T Bell and Timothy P. Softley. “Ultracold molecules and ultracold chemistry”. In: *Mol. Phys.* 107.2 (2009), pp. 99–132.

[13] Jeremy M Hutson. “Ultracold chemistry”. In: *Science* 327.5967 (2010), pp. 788–789.

[14] Goulven Quéméner and John L Bohn. “Strong dependence of ultracold chemical rates on electric dipole moments”. In: *PRA* 81.2 (2010), p. 022702.

[15] Yu Liu et al. “Precision test of statistical dynamics with state-to-state ultracold chemistry”. In: *Nature* 593.7859 (2021), pp. 379–384.

[16] MJ Mark et al. “Precision measurements on a tunable Mott insulator of ultracold atoms”. In: *PRL* 107.17 (2011), p. 175301.

[17] Philip D Gregory et al. “Molecule–molecule and atom–molecule collisions with ultracold RbCs molecules”. In: *New J. Phys.* 23.12 (2021), p. 125004.

[18] Matthew A Nichols et al. “Detection of long-lived complexes in ultracold atom-molecule collisions”. In: *Phys. Rev. X.* 12.1 (2022), p. 011049.

[19] Lincoln D Carr et al. “Cold and ultracold molecules: science, technology and applications”. In: *New J. Phys.* 11.5 (2009), p. 055049.

[20] Nicolaas Bloembergen. “Nonlinear optics and spectroscopy”. In: *RMP* 54.3 (1982), p. 685.

[21] Arthur L Schawlow. “Spectroscopy in a new light”. In: *RMP* 54.3 (1982), p. 697.

[22] Harold J Metcalf and Peter Van der Straten. *Laser cooling and trapping*. Springer Science & Business Media, 1999.

[23] Vladilen Letokhov. *Laser control of atoms and molecules*. OUP Oxford, 2007.

[24] K Dieckmann et al. “Two-dimensional magneto-optical trap as a source of slow atoms”. In: *Phys. Rev. A* 58.5 (1998), p. 3891.

[25] Immanuel Bloch. “Quantum coherence and entanglement with ultracold atoms in optical lattices”. In: *Nature* 453.7198 (2008), pp. 1016–1022.

[26] Florian Schäfer et al. “Tools for quantum simulation with ultracold atoms in optical lattices”. In: *Nat. Rev. Phys.* 2.8 (2020), pp. 411–425.

[27] Juris Ulmanis et al. “Ultracold Molecules Formed by Photoassociation: Heteronuclear Dimers, Inelastic Collisions, and Interactions with Ultrashort Laser Pulses”. In: *Chem. Rev.* 112 (2012), p. 4890.

[28] Thorsten Köhler, Krzysztof Góral, and Paul S. Julienne. “Production of cold molecules via magnetically tunable Feshbach resonances”. In: *Rev. Mod. Phys.* 78 (4 Dec. 2006), pp. 1311–1361.

[29] Taylor N Lewis et al. “Optimizing pulsed-laser ablation production of AlCl molecules for laser cooling”. In: *PCCP* 23.39 (2021), pp. 22785–22793.

[30] Jonathan D Weinstein et al. “Spectroscopy of buffer-gas cooled vanadium monoxide in a magnetic trapping field”. In: *J. Chem. Phys.* 109.7 (1998), pp. 2656–2661.

[31] Dima Egorov et al. “Buffer-gas cooling of atomic and molecular beams”. In: *PRA* 66.4 (2002), p. 043401.

[32] JC Pearson et al. “Pressure broadening of gas phase molecular ions at very low temperature”. In: *PRL* 75.16 (1995), p. 2940.

[33] C. Campbell Wesley and M. Doyle John. *Cold molecules: theory, experiment, applications, Chapter-13*. CRC Press, 2009.

[34] Wesley C Campbell and John M Doyle. “Cooling, trap loading, and beam production using a cryogenic helium buffer gas”. In: *Cold Molecules* (2009), pp. 505–540.

[35] Hyungmok Son et al. “Collisional cooling of ultracold molecules”. In: *Nature* 580.7802 (2020), pp. 197–200.

[36] Juliana J Park et al. “Magnetic trapping of ultracold molecules at high density”. In: *Nat. Phys.* (2023), pp. 1–6.

[37] Harald F Hess. “Evaporative cooling of magnetically trapped and compressed spin-polarized hydrogen”. In: *Phys. Rev. B Condens.* 34.5 (1986), p. 3476.

[38] Benjamin K Stuhl et al. “Evaporative cooling of the dipolar hydroxyl radical”. In: *Nature* 492.7429 (2012), pp. 396–400.

[39] Reginaldo de Jesus Napolitano, Sérgio Carlos Zilio, and Vanderlei Salvador Bagnato. “Adiabatic following conditions for the deceleration of atoms with the Zeeman tuning technique”. In: *Opt. Commun.* 80.2 (1990), pp. 110–114.

[40] Hendrick L Bethlem, Giel Berden, and Gerard Meijer. “Decelerating neutral dipolar molecules”. In: *PRL* 83.8 (1999), p. 1558.

[41] Hendrick L Bethlem and Gerard Meijer. “Production and application of translationally cold molecules”. In: *Int. Rev. Phys. Chem.* 22.1 (2003), pp. 73–128.

[42] Jason R Bochinski et al. “Phase space manipulation of cold free radical OH molecules”. In: *PRL* 91.24 (2003), p. 243001.

[43] Michael R Tarbutt et al. “Slowing heavy, ground-state molecules using an alternating gradient decelerator”. In: *PRL* 92.17 (2004), p. 173002.

[44] Sebastiaan YT van de Meerakker et al. “Production and deceleration of a pulsed beam of metastable NH (a1Δ) radicals”. In: *J. Phys. B: At. Mol. Opt. Phys.* 39.19 (2006), S1077.

[45] Eric R Hudson et al. “Production of cold formaldehyde molecules for study and control of chemical reaction dynamics with hydroxyl radicals”. In: *PRA* 73.6 (2006), p. 063404.

[46] Sebastian Jung, Eberhard Tiemann, and Christian Lisdat. “Cold atoms and molecules from fragmentation of decelerated SO_2”. In: *PRA* 74.4 (2006), p. 040701.

[47] Yabing Ji et al. “Ring-shaped traveling wave Zeeman decelerator for both light and heavy molecules”. In: (2023).

[48] Parul Aggarwal et al. “Deceleration and trapping of SrF molecules”. In: *PRL* 127.17 (2021), p. 173201.

[49] Pierre Meystre and Stig Stenholm. “Introdution to feature on the mechanical effects of light”. In: *JOSA B* 2.11 (1985), pp. 1706–1706.

[50] Steven Chu and Carl Wieman. “Laser cooling and trapping of atoms: Introduction”. In: *JOSA B* 6.11 (1989), pp. 2020–2022.

[51] William D Phillips. “Nobel Lecture: Laser cooling and trapping of neutral atoms”. In: *RMP* 70.3 (1998), p. 721.

[52] Claude N Cohen-Tannoudji. “Nobel Lecture: Manipulating atoms with photons”. In: *RMP* 70.3 (1998), p. 707.

[53] E S Shuman, J F Barry, and D DeMille. “Laser cooling of a diatomic molecule.” In: *Nature* 467 (2010), pp. 820–3.

[54] Sebastiaan YT van de Meerakker et al. “Accumulating NH radicals in a magnetic trap”. In: *PRA* 64.4 (2001), p. 041401.

[55] MD Di Rosa. “Laser-cooling molecules: Concept, candidates, and supporting hyperfine-resolved measurements of rotational lines in the AX (0, 0) band of CaH”. In: *EPJD* 31 (2004), pp. 395–402.

[56] DavidáJ Tannor et al. “Laser cooling of internal degrees of freedom of molecules by dynamically trapped states”. In: *Faraday Discuss.* 113 (1999), pp. 365–383.

[57] Matthew T Hummon et al. “2D magneto-optical trapping of diatomic molecules”. In: *PRL* 110.14 (2013), p. 143001.

[58] J Lim et al. “Laser cooled YbF molecules for measuring the electron’s electric dipole moment”. In: *PRL* 120.12 (2018), p. 123201.

[59] MD Di Rosa. “Laser-cooling molecules: Concept, candidates, and supporting hyperfine-resolved measurements of rotational lines in the AX (0, 0) band of CaH”. In: *EPJD* 31 (2004), pp. 395–402.

[60] Timur Anrievich Isaev. “Direct laser cooling of molecules”. In: *Phys. -Uspekhi.* 63.3 (2020), p. 289.

[61] M. R. Tarbutt. “Laser cooling of molecules”. In: *Contemp. Phys.* 59.4 (2018), pp. 356–376.

[62] Daniel Comparat. “Molecular cooling via Sisyphus processes”. In: *PRA* 89.4 (2014), p. 043410.

[63] Jean Dalibard and Claude Cohen-Tannoudji. “Laser cooling below the Doppler limit by polarization gradients: simple theoretical models”. In: *JOSA B* 6.11 (1989), pp. 2023–2045.

[64] Martin Zeppenfeld et al. “Sisyphus cooling of electrically trapped polyatomic molecules”. In: *Nature* 491.7425 (2012), pp. 570–573.

[65] Hiromitsu Sawaoka et al. “Zeeman-Sisyphus deceleration for heavy molecules with perturbed excited-state structure”. In: *Phys. Rev. A* 107.2 (2023), p. 022810.

[66] William C Stwalley. “Stability of spin-aligned hydrogen at low temperatures and high magnetic fields: New field-dependent scattering resonances and predissociations”. In: *PRL* 37.24 (1976), p. 1628.

[67] Yea-Hwang Uang, Robert F Ferrante, and William C Stwalley. “Model calculations of magnetic-field-induced perturbations and predissociations in 6Li7Li near dissociation”. In: *J. Chem. Phys.* 74.11 (1981), pp. 6267–6270.

[68] D Comparat et al. “Formation of cold Cs ground state molecules through photoassociation in the pure long-range state”. In: *EPJD* 11.1 (2000), pp. 59–71.

[69] Kevin M Jones et al. “Ultracold photoassociation spectroscopy: Long-range molecules and atomic scattering”. In: *RMP* 78.2 (2006), p. 483.

[70] Paul D Lett, PS Julienne, and WD Phillips. "Photoassociative spectroscopy of laser-cooled atoms". In: *Annu. Rev. Phys. Chem.* 46.1 (1995), pp. 423–452.

[71] DJ Heinzen. "Collisions of ultracold atoms in optical fields". In: *AIP Conference Proceedings*. Vol. 323. 1. American Institute of Physics. 1994, pp. 369–388.

[72] William C Stwalley and He Wang. "Photoassociation of ultracold atoms: a new spectroscopic technique". In: *J. Mol. Spectrosc.* 195.2 (1999), pp. 194–228.

[73] Françoise Masnou-Seeuws and Pierre Pillet. "Formation of ultracold molecules (T 200 μK) via photoassociation in a gas of laser-cooled atoms". In: *Advances In Atomic, Molecular, and Optical Physics*. Vol. 47. 2001, pp. 53–127.

[74] He Wang and William C Stwalley. "Ultracold photoassociative spectroscopy of heteronuclear alkali-metal diatomic molecules". In: *J. Chem. Phys.* 108.14 (1998), pp. 5767–5771.

[75] Andrew J Kerman et al. "Production of Ultracold, Polar R b C s* Molecules via Photoassociation". In: *PRL* 92.3 (2004), p. 033004.

[76] T Bergeman et al. "Prospects for production of ultracold RbCs molecules". In: *EPJD* 31.2 (2004), pp. 179–188.

[77] D Wang et al. "Photoassociative production and trapping of ultracold KRb molecules". In: *PRL* 93.24 (2004), p. 243005.

[78] D Wang et al. "The photoassociative spectroscopy, photoassociative molecule formation, and trapping of ultracold". In: *EPJD* 31.2 (2004), pp. 165–177.

[79] C Haimberger et al. "Processes in the formation of ultracold NaCs". In: *J. Phys. B: At. Mol. Opt. Phys.* 39.19 (2006), S957.

[80] J Deiglmayr et al. "Formation of ultracold polar molecules in the rovibrational ground state". In: *PRL* 101.13 (2008), p. 133004.

[81] Cheng Chin et al. "Feshbach resonances in ultracold gases". In: *RMP* 82.2 (2010), p. 1225.

[82] Ugo Fano. "Effects of configuration interaction on intensities and phase shifts". In: *Phys. Rev.* 124.6 (1961), p. 1866.

[83] Ugo Fano et al. "On the absorption spectrum of noble gases at the arc spectrum limit". In: *J. Res. Natl. Inst. Stand. Technol.* 110.6 (2005), p. 583.

[84] Herman Feshbach. "Unified theory of nuclear reactions". In: *Ann. Phys.* 5.4 (1958), pp. 357–390.

[85] E Tiesinga, BJ Verhaar, and HTC Stoof. "Threshold and resonance phenomena in ultracold ground-state collisions". In: *PRA* 47.5 (1993), p. 4114.

[86] S Inouye et al. "Observation of Feshbach resonances in a Bose–Einstein condensate". In: *Nature* 392.6672 (1998), pp. 151–154.

[87] Ph Courteille et al. "Observation of a Feshbach resonance in cold atom scattering". In: *PRL* 81.1 (1998), p. 69.

[88] CA Stan et al. “Observation of Feshbach resonances between two different atomic species”. In: *PRL* 93.14 (2004), p. 143001.

[89] M Theis et al. “Tuning the scattering length with an optically induced Feshbach resonance”. In: *PRL* 93.12 (2004), p. 123001.

[90] A Marte et al. “Feshbach resonances in rubidium 87: Precision measurement and analysis”. In: *PRL* 89.28 (2002), p. 283202.

[91] Johann G Danzl et al. “Quantum gas of deeply bound ground state molecules”. In: *Science* 321.5892 (2008), pp. 1062–1066.

[92] J Cubizolles et al. “Production of Long-Lived Ultracold L i 2 Molecules from a Fermi Gas”. In: *PRL* 91.24 (2003), p. 240401.

[93] K-K Ni et al. “A high phase-space-density gas of polar molecules”. In: *Science* 322.5899 (2008), pp. 231–235.

[94] Mingyang Guo et al. “Creation of an ultracold gas of ground-state dipolar na 23 rb 87 molecules”. In: *PRL* 116.20 (2016), p. 205303.

[95] Sebastian A Will et al. “Coherent microwave control of ultracold Na 23 K 40 molecules”. In: *PRL* 116.22 (2016), p. 225306.

[96] Philippe F Weck and N Balakrishnan. “Importance of long-range interactions in chemical reactions at cold and ultracold temperatures”. In: *Int. Rev. Phys. Chem.* 25.3 (2006), pp. 283–311.

[97] N Balakrishnan. “Perspective: Ultracold molecules and the dawn of cold controlled chemistry”. In: *J. Chem. Phys.* 145.15 (2016).

[98] Goulven Quéméner and John L Bohn. “Ultracold molecular collisions in combined electric and magnetic fields”. In: *PRA* 88.1 (2013), p. 012706.

[99] Moritz Kirste et al. “Quantum-state resolved bimolecular collisions of velocity-controlled OH with NO radicals”. In: *Science* 338.6110 (2012), pp. 1060–1063.

[100] T Zelevinsky, S Kotochigova, and Jun Ye. “Precision test of mass-ratio variations with lattice-confined ultracold molecules”. In: *PRL* 100.4 (2008), p. 043201.

[101] JCJ Koelemeij et al. “Vibrational spectroscopy of HD+ with 2-ppb accuracy”. In: *PRL* 98.17 (2007), p. 173002.

[102] Dhiren M Kara et al. “Measurement of the electron’s electric dipole moment using YbF molecules: methods and data analysis”. In: *New J. Phys.* 14.10 (2012), p. 103051.

[103] David Kawall et al. “Precision zeeman-stark spectroscopy of the metastable a (1)[σ+ 3] state of pbo”. In: *PRL* 92.13 (2004), p. 133007.

[104] Mikhail G Kozlov and Leonti N Labzowsky. “Parity violation effects in diatomics”. In: *J. Phys. B: At. Mol. Opt. Phys.* 28.10 (1995), p. 1933.

[105] David DeMille et al. “Using molecules to measure nuclear spin-dependent parity violation”. In: *PRL* 100.2 (2008), p. 023003.

[106] Mikhail A Baranov. "Theoretical progress in many-body physics with ultracold dipolar gases". In: *Phys. Rep.* 464.3 (2008), pp. 71–111.

[107] ML Wall, Erman Bekaroglu, and Lincoln D Carr. "Molecular Hubbard Hamiltonian: Field regimes and molecular species". In: *PRA* 88.2 (2013), p. 023605.

[108] Michael L Wall and Michael L Wall. *Hyperfine molecular hubbard hamiltonian*. 2015, pp. 93–119.

[109] Bo Yan et al. "Observation of dipolar spin-exchange interactions with lattice-confined polar molecules". In: *Nature* 501.7468 (2013), pp. 521–525.

[110] Alexey V Gorshkov et al. "Tunable superfluidity and quantum magnetism with ultracold polar molecules". In: *PRL* 107.11 (2011), p. 115301.

[111] Kaden RA Hazzard et al. "Far-from-equilibrium quantum magnetism with ultracold polar molecules". In: *PRL* 110.7 (2013), p. 075301.

[112] AK Fedorov et al. "Novel p-wave superfluids of fermionic polar molecules". In: *Sci. Rep.* 6.1 (2016), p. 27448.

[113] Niccolò Bigagli et al. "Observation of Bose–Einstein condensation of dipolar molecules". In: *Nature* 631 (2024).

[114] Matthias Schmidt et al. "Self-bound dipolar droplets and supersolids in molecular Bose-Einstein condensates". In: *Phys. Rev. Res.* 4.1 (2022), p. 013235.

[115] Weijun Yuan et al. "Extreme Loss Suppression and Wide Tunability of Dipolar Interactions in an Ultracold Molecular Gas". In: *arXiv:2505.08773v1* (2025).

[116] Henry F Schaefer III. *Quantum chemistry: the development of ab initio methods in molecular electronic structure theory*. Courier Corporation, 2012.

[117] Janet E Del Bene, Willis B Person, and Krystyna Szczepaniak. "Properties of Hydrogen-Bonded Complexes Obtained from the B3LYP Functional with 6-31G (d, p) and 6-31+ G (d, p) Basis Sets: Comparison with MP2/6-31+ G (d, p) Results and Experimental Data". In: *J. Phys. Chem.* 99.27 (1995), pp. 10705–10707.

[118] Janet E Del Bene and Meredith JT Jordan. "Vibrational spectroscopy of the hydrogen bond: an ab initio quantum-chemical perspective". In: *Int. Rev. Phys. Chem.* 18.1 (1999), pp. 119–162.

[119] Janet E Del Bene et al. "Resolving discrepancies between theory and experiment: IR spectrum of the proton-shared HBr: pyridine complex". In: *J. Phys. Chem. A* 101.25 (1997), pp. 4481–4483.

[120] Janet E Del Bene and Meredith JT Jordan. "What a difference a decade makes: progress in ab initio studies of the hydrogen bond". In: *J. Mol. Struct. THEOCHEM.* 573.1-3 (2001), pp. 11–23.

[121] Steve Scheiner. "The CH··· O hydrogen bond: a historical account". In: *Theory and Applications of Computational Chemistry*. 2005, pp. 831–857.

[122] Masaaki Baba et al. "Geometrical structure of benzene and naphthalene: Ultrahigh-resolution laser spectroscopy and ab initio calculation". In: *J. Chem. Phys.* 135.5 (2011).

[123] Masaaki Baba et al. “Structure and excited-state dynamics of anthracene: Ultrahigh-resolution spectroscopy and theoretical calculation”. In: *J. Chem. Phys.* 130.13 (2009).

[124] J Russell Thomas et al. “The balance between theoretical method and basis set quality: A systematic study of equilibrium geometries, dipole moments, harmonic vibrational frequencies, and infrared intensities”. In: *J. Chem. Phys.* 99.1 (1993), pp. 403–416.

[125] PC Redfern et al. “Computational studies of catechol and water interactions with titanium oxide nanoparticles”. In: *J. Phys. Chem. B* 107.41 (2003), pp. 11419–11427.

[126] Benjamin F Gherman et al. “Dioxygen activation in methane monooxygenase: a theoretical study”. In: *JACS* 126.9 (2004), pp. 2978–2990.

[127] Per EM Siegbahn. “OO bond cleavage and alkane hydroxylation in methane monooxygenase”. In: *J. Biol. Inorg. Chem.* 6 (2001), pp. 27–45.

[128] Victor Guallar et al. “Dynamics of alkane hydroxylation at the non-heme diiron center in methane monooxygenase”. In: *JACS* 124.13 (2002), pp. 3377–3384.

[129] Oleg L Polyansky et al. “Water on the sun: line assignments based on variational calculations”. In: *Science* 277.5324 (1997), pp. 346–348.

[130] Oleg L Polyansky et al. “High-accuracy ab initio rotation-vibration transitions for water”. In: *Science* 299.5606 (2003), pp. 539–542.

[131] Yu Liu and Kang-Kuen Ni. “Bimolecular chemistry in the ultracold regime”. In: *Annu. Rev. Phys. Chem.* 73 (2022), pp. 73–96.

[132] PMA Mestrom et al. “Scattering hypervolume for ultracold bosons from weak to strong interactions”. In: *PRA* 100.5 (2019), p. 050702.

[133] D Caruso et al. “Quenching of internal rotations versus collisional cooling at ultralow energies for weakly interacting partners: Cs 2 (3 Σ u+) with He 3, 4”. In: *PRA* 81.4 (2010), p. 042710.

[134] Michał Tomza et al. “Interatomic potentials, electric properties and spectroscopy of the ground and excited states of the Rb2 molecule: ab initio calculations and effect of a non-resonant field”. In: *Mol. Phys.* 111.12-13 (2013), pp. 1781–1797.

[135] Wensha Xia, Haitao Ma, and Wensheng Bian. “Production of ultracold CaCCH and SrCCH molecules by direct laser cooling: A theoretical study based on accurate ab initio calculations”. In: *J. Chem. Phys.* 155.20 (2021).

[136] Debarati Bhattacharya et al. “Polyatomic ab initio complex potential energy surfaces: Illustration of ultracold collisions”. In: *J. Chem. Theory Comput.* 13.4 (2017), pp. 1682–1690.

[137] Ayelet Klein et al. “Directly probing anisotropy in atom–molecule collisions through quantum scattering resonances”. In: *Nat. Phys.* 13.1 (2017), pp. 35–38.

[138] Piotr S Żuchowski and Jeremy M Hutson. “Reactions of ultracold alkali-metal dimers”. In: *PRA* 81.6 (2010), p. 060703.

[139] José Marıa Lucas et al. “Experimental cross-sections energy dependence and an ab initio electronic structure survey of the ground singlet potential surface for reactive Li++ n-C 3 H 7 Cl collisions at low energies”. In: *Phys. Chem. Chem. Phys.* 12.41 (2010), pp. 13646–13656.

[140] Hela Ladjimi et al. “Ab-initio study of the ground and low-lying excited states including the spin-orbit effect of RbBa molecule and laser cooling feasibility”. In: *J. Quant. Spectrosc. Radiat. Transf.* 252 (2020), p. 107069.

[141] Svetlana Kotochigova et al. “Ab initio properties of Li-group-II molecules for ultracold matter studies”. In: *J. Chem. Phys.* 135.16 (2011).

[142] Amal Moussa, Nayla El-Kork, and Mahmoud Korek. “Laser cooling and electronic structure studies of CaK and its ions CaK±”. In: *New J. Phys.* 23.1 (2021), p. 013017.

[143] Lushuai Cao et al. “A unified ab initio approach to the correlated quantum dynamics of ultracold fermionic and bosonic mixtures”. In: *J. Chem. Phys.* 147.4 (2017).

[144] S Hofsäss et al. “Optical cycling of AlF molecules”. In: *New J. Phys.* 23 (2021), p. 075001.

[145] M. Karra et al. “Dynamics of translational and rotational thermalization of AlF molecules via collisions with cryogenic helium”. In: *Phys. Rev. A* 105 (2022), p. 022808.

[146] S. Truppe et al. “Spectroscopic characterization of aluminum monofluoride with relevance to laser cooling and trapping”. In: *Phys. Rev. A* 100 (2019), p. 052513.

[147] Lane IC. Wells N. “Electronic states and spin-forbidden cooling transitions of AlH and AlF.” In: *Phys. Chem. Chem. Phys.* 13 (2011), p. 19018.

[148] X. Liu et al. “The chemistry of AlF and CaF production in buffer gas sources”. In: *J. Chem. Phys.* 157.7 (2022), p. 074305.

[149] Sidney C. Wright et al. “Cryogenic buffer gas beams of AlF, CaF, MgF, YbF, Al, Ca, Yb and NO – a comparison”. In: *Mol. Phys.* (2022), e2146541.

[150] J. L. Highberger et al. “Heavy-Metal Chemistry in Proto–Planetary Nebulae: Detection of MgNC, NaCN, and AlF toward CRL 2688”. In: *ApJ* 562 (2001), p. 790.

[151] Nadjinangar Gotoum et al. “Rotational excitation of aluminium monofluoride (AlF) by He atom at low temperature”. In: *Astrophys* 332 (2011), p. 209.

[152] P Gross et al. “On some equilibria involving aluminium monohalides”. In: *Disc. Faraday Soc.* 4 (1948), pp. 206–215.

[153] RB Ferguson. “Observations on some aluminium fluoride minerals”. In: *Am. Miner. or Am. Min.* 34.5-6 (1949), pp. 383–397.

[154] P Gross, C Hayman, and DL Levi. “The heats of formation of metal halides. Aluminium fluoride”. In: *Trans. Faraday Soc.* 50 (1954), pp. 477–480.

[155] RF Barrow, I Kopp, and C Malmberg. “The electronic spectrum of gaseous AIF”. In: *Phys. Scr.* 10.1-2 (1974), p. 86.

[156] SP So and WG Richards. “A theoretical study of the excited electronic states of AlF”. In: *J. Phys. B: At. Mol. Opt. Phys.* 7.14 (1974), p. 1973.

[157] John M Dyke et al. “A study of aluminium monofluoride and aluminium trifluoride by high-temperature photoelectron spectroscopy”. In: *Chem. Phys.* 88.2 (1984), pp. 289–298.

[158] Robert Klein and Pavel Rosmus. “Ab initio calculations of infrared transition probabilities in the electronic ground states of AlF and AlF+”. In: *Theor. Chim. Acta.* 66 (1984), pp. 21–29.

[159] David M Hirst. “Ab initio potential energy curves for excited states of AIF”. In: *J. Mol. Spectrosc.* 121.1 (1987), pp. 189–198.

[160] Hartmut G Hedderich and Peter F Bernath. “The infrared emission spectrum of gaseous AIF”. In: *J. Mol. Spectrosc.* 153.1-2 (1992), pp. 73–80.

[161] Nicole Walter et al. “Spectroscopic characterization of the a3Π state of aluminum monofluoride”. In: *J. Chem. Phys.* 156.12 (2022).

[162] John A Pople. “Nobel lecture: Quantum chemical models”. In: *RMP* 71.5 (1999), p. 1267.

[163] Robert J Harrison and Ron Shepard. “Ab initio molecular electronic structure on parallel computers”. In: *Annu. Rev. Phys. Chem.* 45.1 (1994), pp. 623–658.

[164] Tomoya Ono and Kikuji Hirose. “Timesaving double-grid method for real-space electronic-structure calculations”. In: *PRL* 82.25 (1999), p. 5016.

[165] He Li et al. “Deep-learning density functional theory Hamiltonian for efficient ab initio electronic-structure calculation”. In: *Nat. Comput. Sci.* 2.6 (2022), pp. 367–377.

[166] Zifeng Wang et al. “Machine learning method for tight-binding Hamiltonian parameterization from ab-initio band structure”. In: *Npj Comput. Mater.* 7.1 (2021), p. 11.

[167] Arvi Rauk. *Orbital interaction theory of organic chemistry*. John Wiley & Sons, 2004.

[168] Carlos A Jiménez-Hoyos, Thomas M Henderson, and Gustavo E Scuseria. “Generalized Hartree–Fock description of molecular dissociation”. In: *J. Chem. Theory Comput.* 7.9 (2011), pp. 2667–2674.

[169] Christopher R Myers et al. “Fock’s expansion, Kato’s cusp conditions, and the exponential ansatz”. In: *PRA* 44.9 (1991), p. 5537.

[170] Frank Jensen. “Polarization consistent basis sets: Principles”. In: *J. Chem. Phys.* 115.20 (2001), pp. 9113–9125.

[171] Wim Klopper and Werner Kutzelnigg. “Gaussian basis sets and the nuclear cusp problem”. In: *J. Mol. Struct. THEOCHEM.* 135 (1986), pp. 339–356.

[172] Frank Jensen. “Estimating the Hartree—Fock limit from finite basis set calculations”. In: *Theor. Chem. Acc.* 113 (2005), pp. 267–273.

[173] Béla Paizs et al. “Intermolecular bond lengths: extrapolation to the basis set limit on uncorrected and BSSE-corrected potential energy hypersurfaces”. In: *J. Comput. Chem.* 22.2 (2001), pp. 196–207.

[174] Samuel F Boys and FJMP Bernardi. “The calculation of small molecular interactions by the differences of separate total energies. Some procedures with reduced errors”. In: *Mol. Phys.* 19.4 (1970), pp. 553–566.

[175] İskender Öksüz and Oktay Sinanoğlu. "Theory of Atomic Structure Including Electron Correlation. II. All-External Pair Correlations in the Various States and Ions of B, C, N, O, F, Ne, and Na, and Prediction of Electron Affinities and Atomic Excitation Energies". In: *Phys. Rev.* 181.1 (1969), p. 54.

[176] K Jankowski and M Polasik. "An approximate method for the evaluation of electron correlation effects on atomic energy differences". In: *J. Phys. B: At. Mol. Opt. Phys.* 17.12 (1984), p. 2393.

[177] Paul Westhaus and Oktay Sinanoğlu. "Theory of Atomic Structure Including Electron Correlation. III. Calculations of Multiplet Oscillator Strengths and Comparisons with Experiments for CII, NI, NII, NIII, OII, OIII, OIV, FII, NeII, and NaIII". In: *Phys. Rev.* 183.1 (1969), p. 56.

[178] Andrzej J Sadlej. "Perturbation theory of the electron correlation effects for atomic and molecular properties". In: *J. Chem. Phys.* 75.1 (1981), pp. 320–331.

[179] Jeffrey C Grossman, Lubos Mitas, and Krishnan Raghavachari. "Structure and stability of molecular carbon: importance of electron correlation". In: *PRL* 75.21 (1995), p. 3870.

[180] Weston Thatcher Borden and Ernest R Davidson. "The importance of including dynamic electron correlation in ab initio calculations". In: *Acc. Chem. Res.* 29.2 (1996), pp. 67–75.

[181] Hans-Joachim Werner and Wilfried Meyer. "PNO-CI and PNO-CEPA studies of electron correlation effects: V. Static dipole polarizabilities of small molecules". In: *Mol. Phys.* 31.3 (1976), pp. 855–872.

[182] Leland C Allen, Enrico Clementi, and HM Gladney. "Pair correlation energies". In: *RMP* 35.3 (1963), p. 465.

[183] Björn O Roos. "The complete active space SCF method in a fock-matrix-based super-CI formulation". In: *Int. J. Quantum Chem.* 18.S14 (1980), pp. 175–189.

[184] Daniel Süß, Stefan E Huber, and Andreas Mauracher. "On the impact of multi-reference character of small transition metal compounds on their bond dissociation energies". In: *J. Chem. Phys.* 152.11 (2020).

[185] J Cizek and J Paldus. "Coupled cluster approach". In: *Phys. Scr.* 21.3-4 (1980), p. 251.

[186] Jiřı Čızek. "On the correlation problem in atomic and molecular systems. Calculation of wavefunction components in Ursell-type expansion using quantum-field theoretical methods". In: *J. Chem. Phys.* 45.11 (1966), pp. 4256–4266.

[187] Krishnan Raghavachari et al. "A fifth-order perturbation comparison of electron correlation theories". In: *Chem. Phys. Lett.* 157.6 (1989), pp. 479–483.

[188] John F Stanton. "Why CCSD (T) works: a different perspective". In: *Chem. Phys. Lett.* 281.1-3 (1997), pp. 130–134.

[189] László Gyevi-Nagy, Mihály Kállay, and Péter R Nagy. "Accurate reduced-cost CCSD (T) energies: parallel implementation, benchmarks, and large-scale applications". In: *J. Chem. Theory Comput.* 17.2 (2021), pp. 860–878.

[190] David Feller, Kirk A Peterson, and J Grant Hill. “On the effectiveness of CCSD (T) complete basis set extrapolations for atomization energies”. In: *J. Chem. Phys.* 135.4 (2011).

[191] Werner Kutzelnigg. “r 12-Dependent terms in the wave function as closed sums of partial wave amplitudes for large l”. In: *Theor. Chim. Acta.* 68 (1985), pp. 445–469.

[192] Pekka Pyykko. “The physics behind chemistry and the periodic table”. In: *Chem. Rev.* 112.1 (2012), pp. 371–384.

[193] Markus Reiher. “Douglas–Kroll–Hess Theory: a relativistic electrons-only theory for chemistry”. In: *Theor. Chem. Acc.* 116.1 (2006), pp. 241–252.

[194] Takahito Nakajima and Kimihiko Hirao. “The Douglas–Kroll–Hess Approach”. In: *Chem. Rev.* 112.1 (2012), pp. 385–402.

[195] Avijit Shee. “Relativistic coupled cluster theory-in molecular properties and in electronic structure”. PhD thesis. Université Paul Sabatier-Toulouse III, 2016.

[196] Lucjan Piela. *Ideas of quantum chemistry*. Elsevier, 2006.

[197] Valerio Magnasco, Camilla Costa, and Giuseppe Figari. “Long-range coefficients for molecular interactions. II”. In: *J. MOL. STRUC-THEOCHEM* 206.3-4 (1990), pp. 235–252.

[198] Valerio Magnasco, Giuseppe Figari, and Camilla Costa. “Long-range coefficients for molecular interactions”. In: *J. MOL. STRUC-THEOCHEM* 164.1-2 (1988), pp. 49–66.

[199] Tatiana Korona, Michał Przybytek, and Bogumil Jeziorski. “Time-independent coupled cluster theory of the polarization propagator. Implementation and application of the singles and doubles model to dynamic polarizabilities and van der Waals constants”. In: *Mol. Phys.* 104 (2006), p. 2303.

[200] Jeremy M. Hutson and C. Ruth Le Sueur. “molscat: A program for non-reactive quantum scattering calculations on atomic and molecular collisions”. In: *Comput. Phys. Commun.* 241 (2019), pp. 9–18.

[201] Roy G Gordon. “New method for constructing wavefunctions for bound states and scattering”. In: *J. Chem. Phys.* 51.1 (1969), pp. 14–25.

[202] Bernard R Johnson. “The renormalized Numerov method applied to calculating bound states of the coupled-channel Schroedinger equation”. In: *J. Chem. Phys.* 69.10 (1978), pp. 4678–4688.

[203] Bernard R Johnson. “New numerical methods applied to solving the one-dimensional eigenvalue problem”. In: *J. Chem. Phys.* 67.9 (1977), pp. 4086–4093.

[204] Jeremy M Hutson. “Coupled channel methods for solving the bound-state Schrödinger equation”. In: *Comput. Phys. Commun.* 84.1-3 (1994), pp. 1–18.

[205] D. E. Manolopoulos. “An improved log derivative method for inelastic scattering”. In: *J. Chem. Phys* 85 (1986), pp. 6425–6429.

[206] Millard H. Alexander and David E. Manolopoulos. “A stable linear reference potential algorithm for solution of the quantum close-coupled equations in molecular scattering theory”. In: *J. Chem. Phys* 86 (1987), pp. 2044–2050.

[207] FJ Lovas et al. “Diatomic spectral database (version 2.1)”. In: *NIST* (2005).

[208] WP Witt and RF Barrow. “The heat of sublimation of aluminium trifluoride and the heat of formation of aluminium monofluoride”. In: *Trans. Faraday Soc.* 55 (1959), pp. 730–735.

[209] HC Rowlinson and RF Barrow. “The band-spectrum of aluminium monofluoride”. In: *Proc. Nat. Acad. Sci. India Sect. A* 66.5 (1953), p. 437.

[210] FC Wyse, Walter Gordy, and Edwin F Pearson. “Millimeter and Submillimeter Wave Spectrum and Molecular Constants of Aluminum Monofluoride”. In: *J. Chem. Phys.* 52.8 (1970), pp. 3887–3889.

[211] Slawomir M Cybulski and Marion L Lytle. “The origin of deficiency of the supermolecule second-order Møller-Plesset approach for evaluating interaction energies”. In: *J. Chem. Phys.* 127.14 (2007).

[212] Reinhold F Fink. “Why does MP2 work?” In: *J. Chem. Phys.* 145.18 (2016).

[213] Malgorzata Jeziorska et al. “On the optimal choice of monomer geometry in calculations of intermolecular interaction energies: Rovibrational spectrum of Ar–HF from two- and three-dimensional potentials”. In: *J. Chem. Phys* 113.8 (2000), pp. 2957–2968.

[214] Alexandre Faure et al. “On the importance of full-dimensionality in low-energy molecular scattering calculations”. In: *Sci. Rep.* 6 (2016).

[215] Thomas B. Adler, Gerald Knizia, and Hans-Joachim Werner. “A simple and efficient CCSD(T)-F12 approximation”. In: *J. Chem. Phys* 127 (2007), p. 221106.

[216] Denis Bokhan, Seiichiro Ten-no, and Jozef Noga. “Implementation of the CCSD(T)-F12 method using cusp conditions”. In: *Phys. Chem. Chem. Phys.* 10 (2008), p. 3320.

[217] Tanja Van Mourik and Thom H. Dunning Jr. “Gaussian basis sets for use in correlated molecular calculations. VIII. Standard and augmented sextuple zeta correlation consistent basis sets for aluminum through argon”. In: *Int. J. Quantum Chem.* 76 (2000), pp. 205–221.

[218] Florian Weigend. “A fully direct RI-HF algorithm: Implementation, optimised auxiliary basis sets, demonstration of accuracy and efficiency”. In: *Phys. Chem. Chem. Phys.* 4 (18 2002), pp. 4285–4291.

[219] *cc*R*epo, A correlation consistent basis sets repository*.

[220] Benjamin P. Pritchard et al. “New Basis Set Exchange: An Open, Up-to-Date Resource for the Molecular Sciences Community”. In: *J. Am. Chem. Soc.* 59 (2019), pp. 4814–4820.

[221] David Feller. “The role of databases in support of computational chemistry calculations”. In: *J. Comput. Chem.* 17 (1996), pp. 1571–1586.

[222] Karen L. Schuchardt et al. “Basis Set Exchange: A Community Database for Computational Sciences”. In: *J. Am. Chem. Soc.* 47 (2007), pp. 1045–1052.

[223] David E. Woon and Thom H. Dunning. “Gaussian basis sets for use in correlated molecular calculations. III. The atoms aluminum through argon”. In: *J. Chem. Phys* 98.2 (1993), pp. 1358–1371.

[224] David E. Woon and Thom H. Dunning. “Gaussian basis sets for use in correlated molecular calculations. IV. Calculation of static electrical response properties”. In: *J. Chem. Phys* 100.4 (1994), pp. 2975–2988.

[225] Rick A. Kendall, Thom H. Dunning, and Robert J. Harrison. “Electron affinities of the first-row atoms revisited. Systematic basis sets and wave functions”. In: *J. Chem. Phys* 96.9 (1992), pp. 6796–6806.

[226] Mihály Kállay et al. “The MRCC program system: Accurate quantum chemistry from water to proteins”. In: *Chem. Phys.* 152 (2020), p. 074107.

[227] Claudia Hampel, Kirk A. Peterson, and Hans-Joachim Werner. “A comparison of the efficiency and accuracy of the quadratic configuration interaction (QCISD), coupled cluster (CCSD), and Brueckner coupled cluster (BCCD) methods”. In: *Chem. Phys. Lett.* 190 (1992), pp. 1–12.

[228] Mihály Kállay and Jürgen Gauss. “Approximate treatment of higher excitations in coupled-cluster theory”. In: *Chem. Phys.* 123 (2005), p. 214105.

[229] Mihály Kállay and Jürgen Gauss. “Approximate treatment of higher excitations in coupled-cluster theory. II. Extension to general single-determinant reference functions and improved approaches for the canonical Hartree–Fock case”. In: *Chem. Phys.* 129 (2008), p. 144101.

[230] Hans-Joachim Werner and Ernst-Albrecht Reinsch. “The self-consistent electron pairs method for multiconfiguration reference state functions”. In: *J. Chem. Phys* 76 (1982), pp. 3144–3156.

[231] Hans-Joachim Werner and Peter J. Knowles. “An efficient internally contracted multiconfiguration–reference configuration interaction method”. In: *J. Chem. Phys* 89 (1988), pp. 5803–5814.

[232] Peter J. Knowles and Hans-Joachim Werner. “An efficient method for the evaluation of coupling coefficients in configuration interaction calculations”. In: *Chem. Phys. Lett.* 145 (1988), pp. 514–522.

[233] Hans-Joachim Werner and Ernst-Albrecht Reinsch. “The self-consistent electron pairs method for multiconfiguration reference state functions”. In: *J. Chem. Phys* 76 (1982), pp. 3144–3156.

[234] Hans-Joachim Werner et al. “The Molpro quantum chemistry package”. In: *J. Chem. Phys* 152 (2020), p. 144107.

[235] Hans-Joachim Werner et al. “Molpro: a general-purpose quantum chemistry program package”. In: *Wiley Interdiscip. Rev. Comput. Mol. Sci.* 2 (2012), pp. 242–253.

[236] Bogumił Jeziorski and Robert Moszynski. "Explicitly connected expansion for the average value of an observable in the coupled-cluster theory". In: *Int. J. Quantum Chem.* 48 (1993), pp. 161–183.

[237] Tatiana Korona. "The effect of local approximations on first-order properties from expectation-value coupled cluster theory." In: *Theor. Chem. Acc.* 129 (2011).

[238] Tatiana Korona and Bogumil Jeziorski. "One-electron properties and electrostatic interaction energies from the expectation value expression and wave function of singles and doubles coupled cluster theory". In: *J. Chem. Phys.* 125.18 (2006), p. 184109.

[239] M Modrzejewski, AM Tucholska, and R Moszynski. "Transition properties from the Hermitian formulation of the coupled cluster polarization propagator." In: *J. Chem. Phys.* 141 (2014).

[240] C. Zhu, A. Dalgarno, and A. Derevianko. "van der Waals interactions between molecular hydrogen and alkali-metal atoms". In: *Phys. Rev. A* 65 (3 2002), p. 034708.

[241] Mauro Masili and Anthony F. Starace. "Static and dynamic dipole polarizability of the helium atom using wave functions involving logarithmic terms". In: *Phys. Rev. A* 68 (2003), p. 012508.

[242] R F Barrow, I Kopp, and C Malmberg. "The Electronic Spectrum of Gaseous AlF". In: *Phys. Scr.* 10 (1974), p. 86.

[243] Tak-San Ho and Herschel Rabitz. "A general method for constructing multidimensional molecular potential energy surfaces from ab initio calculations". In: *J. Chem. Phys.* 104 (1996), pp. 2584–2597.

[244] Tak-San Ho and Herschel Rabitz. "Proper construction of ab initio global potential surfaces with accurate long-range interactions". In: *J. Chem. Phys* 113 (2000), pp. 3960–3968.

[245] Jeremy M. Hutson and C. Ruth Le Sueur. "bound and field: Programs for calculating bound states of interacting pairs of atoms and molecules". In: *Comput. Phys. Commun.* 241 (Aug. 2019), pp. 1–8.

[246] A. M. Arthurs, Alexander Dalgarno, and David Robert Bates. "The theory of scattering by a rigid rotator". In: *Proc. Math. Phys. Eng. Sci.* 256 (1960), pp. 540–551.

[247] J. M. Hutson and C. R. Le Sueur. MOLSCAT, BOUND *and* FIELD *version 2020.0*. `https://github.com/molscat/molscat`. 2020.

[248] T. V. Tscherbul et al. "Fine and hyperfine interactions in cold YbF-He collisions in electromagnetic fields". In: *Phys. Rev. A* 75 (Mar. 2007), p. 033416.

[249] Stefano Borocci et al. "Complexes of helium with neutral molecules: Progress toward a quantitative scale of bonding character". In: *J. Comput. Chem.* 41.10 (2020), pp. 1000–1011.

[250] Nicholas R Hutzler, Hsin-I Lu, and John M Doyle. "The buffer gas beam: An intense, cold, and slow source for atoms and molecules". In: *Chem. Rev.* 112.9 (2012), pp. 4803–4827.

[251] N. Balakrishnan et al. “The He–CaH(2+) interaction. II. Collisions at cold and ultracold temperatures”. In: *J. Chem. Phys.* 118.16 (2003), pp. 7386–7393.

[252] Zi-Liang Li et al. “Efficient production of ultracold polar molecules 23Na40K in their absolute ground state via intermediate state of the coupled complex B 1Π— ν= 4¿ c 3Σ+— ν= 25¿”. In: *Sci. China- Phys. Mech. Astron.* 66.9 (2023), p. 293011.

[253] Charbel Karam et al. “Two-photon optical shielding of collisions between ultracold polar molecules”. In: *Phys. rev. res.* 5.3 (2023), p. 033074.

[254] John M Doyle and Bretislav Friedrich. “Molecules are cool”. In: *Nature* 401.6755 (1999), pp. 749–751.

[255] Hendrick L Bethlem et al. “Electrostatic trapping of ammonia molecules”. In: *Nature* 406.6795 (2000), pp. 491–494.

[256] Jeremy M Sage et al. “Optical production of ultracold polar molecules”. In: *PRL* 94.20 (2005), p. 203001.

[257] S Tassy et al. “Sympathetic cooling in a mixture of diamagnetic and paramagnetic atoms”. In: *J. Phys. B: At. Mol. Opt. Phys.* 43.20 (2010), p. 205309.

[258] C Silber et al. “Quantum-degenerate mixture of fermionic lithium and bosonic rubidium gases”. In: *PRL* 95.17 (2005), p. 170408.

[259] Immanuel Bloch et al. “Sympathetic cooling of 85 Rb and 87 Rb”. In: *Phys. Rev. A* 64.2 (2001), p. 021402.

[260] H López et al. “Sympathetic cooling of OH- ions using ultracold Rb atoms in a dark SPOT”. In: *Ion Traps for Tomorrow’s Applications*. IOS Press, 2015, pp. 279–287.

[261] Daoling Peng and Markus Reiher. “Exact decoupling of the relativistic Fock operator”. In: *Theor. Chem. Acc.* 131 (2012), pp. 1–20.

[262] Markus Reiher and Alexander Wolf. “Exact decoupling of the Dirac Hamiltonian. I. General theory”. In: *J. Chem. Phys.* 121.5 (2004), pp. 2037–2047.

[263] Markus Reiher and Alexander Wolf. “Exact decoupling of the Dirac Hamiltonian. II. The generalized Douglas–Kroll–Hess transformation up to arbitrary order”. In: *J. Chem. Phys.* 121.22 (2004), pp. 10945–10956.

[264] Peter Schwerdtfeger. “The pseudopotential approximation in electronic structure theory”. In: *ChemPhysChem* 12.17 (2011), pp. 3143–3155.

[265] Manuel Lara et al. “Ultracold Rb-OH collisions and prospects for sympathetic cooling”. In: *PRL* 97.18 (2006), p. 183201.